nature portfolio

Peer Review File

Combination of PARP and KRASG12D Inhibitors Enhances Therapeutic Efficacy by Exploiting Vulnerabilities in PDAC

Corresponding Author: Professor Min Deng

This file contains all reviewer reports in order by version, followed by all author rebuttals in order by version.

Version 0:

Reviewer comments:

Reviewer #1

(Remarks to the Author)
In this well written manuscript, the authors first tested the role of KRAS G12D inhibition on the DNA repair pathway in KRAS mutated cells (via RAD51 foci clearance rate after ionizing radiation) after which they treated immunocompromised and immunocompetent mice with vehicle, olaparib, KRAS G12D inhibition or combination therapy. In both models, interestingly, the combination treatment resulted in a prolonged OS of the animals without overt signs of untenable toxicity in the animals.

Comments:
(1) Do the authors have a hypothesis as to why the change in HR pathways was only observed in KRAS G12d mutated cell lines, while HR pathways of lines with KRAS G12V or KRAS G12C were unaffected by the pan-RAS inhibitor?
(2) For the sake of completeness, the authors might consider treating the KRAS G12D cell lines with olaparib alone to ensure that the PARPi alone would not (albeit unexpectedly) result in decreased cell viability.
(3) ALthough the results are interesting preliminarily, it would behoove the authors to provide substantially more mechanistic insights into the combination of KRAS and PARPi therapy. For example, showing CD8 and CC3 increase with the combination of drugs does not in any way prove that there is T-cell mediated killing. Without additional mechanism insights, I do not think that this paper has sufficient interest for Nature Comm readership.

Reviewer #2

(Remarks to the Author)
The authors of this manuscript reported a new therapeutic strategy by combining PARPis and KRASG12D inhibitors to target pancreatic ductal adenocarcinoma (PDAC). Mechanistically, KRASG12D inhibitor reduces HR repair protein expression including BRCA1, RAD51 and RPA32 and thus impairs HR repair capacity, sensitizing to PARPi treatment in multiple in vitro and in vivo PDAC models including CDX, PDX and syngeneic mouse models. Overall, The strength of this manuscript is providing a therapeutic strategy by combining PARPis and KRASG12D inhibitors, which can be readily translated into clinical testing. Results from mouse models clearly demonstrated efficacy of this combination strategy. There are several concerns regarding the mechanistic understanding of the combination treatment and also the clinical applications.
1. RAS/Raf/MEK/ERK and PI3K/ATKT/mTOR pathways are downstream of KRAS activation. The therapeutic efficacy of combining inhibitors of these two pathways (RAS/Raf/MEK/ERK and PI3K/ATKT/mTOR) have been studied and demonstrated in multiple cancer types such as ERK inhibitors, PI3K inhibitors and mTOR inhibitors. As KRASG12D inhibitors only target a specific KRAS activation mutation in a small subset of patients. What is the advantage of using KRASG12D inhibitors in combination with PARPis compared to these existing strategies targeting downstream signaling of KRAS activation regardless of specific mutation sites. Perhaps, this specific inhibitor targeting KRASG12D in combination of PARPis may reduce potential toxicity of combining inhibitors targeting RAS/Raf/MEK/ERK and PI3K/ATKT/mTOR in normal cells.
2. Inhibition of RAS/Raf/MEK/ERK or PI3K/ATKT/mTOR pathway has been shown to regulate key DNA repair proteins and DNA damage response signaling molecules in previous studies. It is not surprising to observe that KRASG12D inhibitors can also reduce multiple HR-related proteins. The mechanistic findings of KRASG12D inhibitors in HR regulation is logically expected due to these existing data, which diminish the novelty of this report.

3. The mechanism underlying KRASG12D inhibitor-induced HR repair gene suppression is not clear. First, it remains unknown whether the reduction in HR gene expression induced by KRASG12D inhibitor is at protein level or at transcriptional level. Second, KRASG12D inhibitor can ablate its downstream signaling ERK1/2 and AKT, which direct regulate cell proliferation. HR repair capacity, the transcriptional expression of BRCA1, RAD51 are known associated with s phase cells. In Fig. 2SE, the authors tested the cell cycle distribution by PI staining and concluded that the reduction of HR and HR repair proteins is not resulted from cell cycle arrest. This experiment was conducted at one time point at 24 hrs. Multiple time points might provide a better assessment of the impact of KRASG12D inhibitor on cell cycle. BrdU labeling assay for S phase evaluation is more accurate than PI staining. Testing the effect of KRASG12D inhibitor in synchronized cells on HR repair protein expression could be more convincing to exclude the indirect contribution from cell cycle arrest. Thirdly, the pan-KRAS inhibitor BI-2865 did not induce HR deficiency in KRAS G12V or KRAS G12C cells (Fig. S2). Does this pan RAS BI-2865 inhibit RAS downstream signaling ERK1/2 and AKT in these cells? Is inhibition of RAS downstream signaling required or sufficient for the reduction of HR repair expression by KRASG12D inhibitor?
4. As the authors discussed that the resistance to KRASG12D inhibitor is a clinical chanllenge, does KRASG12D inhibitor suppress HR repair capacity and HR repair protein expression in KRASG12D inhibitor-resistant cells? Does this combination regimen work for KRASG12D inhibitor-resistant tumors? The models used in the current study are KRASG12D inhibitor-naïve models.

Reviewer #3

(Remarks to the Author)
Reviewer Understanding and General Comments
In this manuscript, Xu and colleagues investigate the specific effect of KRAS G12D inhibition with MRTX1133 to induce homologous repair (HR) deficiency in pancreatic cancer cells, which could be exploited therapeutically by combining KRAS inhibition with PARP inhibitors. The authors used both human and mouse pancreatic cancer cell lines harboring the KRAS G12D mutation to show that effective inhibition of the MAPK pathway induces downregulation of HR genes, including RAD51, and impairs the cellular response to double-strand breaks induced through irradiation. Notably, inhibition of the pathway per se does not increase DNA damage but rather reduces the efficiency of repairing induced damage.
The specificity of this induced phenotype is addressed by showing that the downregulation of HR genes does not occur in KRAS wild-type cells (e.g., BXPC-3) treated with MRTX1133 nor in pancreatic cancer cells harboring other KRAS mutations (e.g., G12V) treated with a pan-Ras inhibitor. Importantly, the treatment-induced phenotype is not solely attributable to a reduced cell proliferation index. The authors further demonstrate synergistic effects between MRTX1133 and the PARP inhibitor Olaparib in both in vitro and in vivo settings.
This is a timely and interesting manuscript given the interest around KRAS inhibition in pancreatic cancer. Previous studies have shown that KRAS inhibitors, including MRTX1133, often have transient efficacy with resistance mechanisms—both genetic and non-genetic—emerging rapidly. Additionally, rapid pathway rewiring following treatment necessitates close monitoring of pathway dynamics to interpret findings robustly. I think the last two aspects are a bit overlooked in this manuscript.
While the findings in this manuscript are potentially impactful, the study lacks rigor in conducting and reporting experiments, with significant gaps in statistical analysis and experimental controls.

One important point that needs clarification is the specificity of HR deficiency induction. The question here is whether the treatment of G12D cells with pan-Ras inhibitors would result in the same phenotype, i.e. HR deficiency. In my opinion, the following experiments should be conducted: (i) Evaluate the effect of pan-RAS inhibitors on KRAS G12D-driven cancer cells, as the authors have access to this drug; (ii) test another MAPK pathway inhibitor (trametinib) in KRAS G12D-mutant and non-G12D-mutant tumor cells; (iii) Perform genetic perturbation (e.g., KRAS G12D knockdown/knockout) to determine if the HR-deficient phenotype is allele-specific or drug-specific. Furthermore, I think that the HRD phenotype needs a more rigorous validation by, among other things, use a validated HRD score to quantitatively assess homologous repair deficiency across cell lines. The authors might consider using the COMET assays to measure DSB formation accurately and correlate results with HR efficiency and test synthetic lethality by targeting RAD51 or BRCA1/2 genetically in combination with KRAS inhibition.
As I already said above, the emergence of resistance is overlooked in this work. The authors should conduct long-term studies to investigate resistance mechanisms to KRAS inhibitors and/or the combination with the respect to the HR-deficient phenotype. Moreover, I think it is very important for the authors to evaluate pathway dynamics (e.g., pERK levels) over time to understand the kinetics of pathway rewiring after KRAS inhibition. To the clinical relevance of the work, I think that it would be very important to investigate potential synergism with cis-platinum and exclude activity from other chemotherapy agents commonly used in pancreatic cancer. Finally, if the activation of the immune system is responsible for the in vivo efficacy of the drug, this should be investigated deeply. For example, performing experiments with mouse pancreatic cancer cells in immunodeficient and immunocompetent settings. Alternatively, the authors might consider the specific depletion of CD8+ T cells to further distinguish immune-related effects from direct tumor effects. Moreover, the authors should assess the effect of treatment on the composition and activation status of tumor microenvironment cells, potentially using single-cell sequencing or cytometric analysis.

Finally, I found quite difficult to follow the manuscript when it comes to treatment timepoints. The (in vivo) treatment seems to last from 10 to 14 days. Then, the tumor burden is assessed at 7 days in the immunodeficient setting and at 7 and 14 days in the immunocompetent setting (using KPC derived cell lines). This is also in contrast with the timeline of the survival experiments. It is very confusing. The authors should be more clear in outlining the timeline of the experiments, which again is quite important considering the dynamics of pathway rewiring.

Specific Comments
Figures and Analysis
•Figure 1A: Clearly indicate how many cases are included in the analysis and justify the use of non-KRAS G12D as a control. Would non-G12D KRAS alleles be more appropriate?
•Figure 1B: The GSEA analysis is not convincing. Adjust for false discovery rate (FDR) and use appropriately sized gene sets. Sparse or small gene sets reduce the validity of the results.
•Figure 1C: Revise the legend. MRTX1133 does not induce DNA damage; rather, it alters the DNA damage response.
•Figure 1E-G: Why reporting surviving fraction and not number or size of colonies; very different concepts/parameters.
•Figure 2A-D: Explicitly indicate the timing of analyses.
•Figure 2E-H: Address why foci reduction is seen for BRCA1, RPA32, and RAD51 but not for MDC1, FK2, or 53BP1.
•Figure 2I: Correct the DR-GFP reporter system label; it is not an in vivo system.
•Figure 3C: Clarify the vehicle used. Address the significant differences in results between human and mouse cells. Is the results consistent across different mouse cell lines?
•Figure 4A: The experimental schematic does not align with the legend.
•Figure 4H-I and Figure 5H-I: Provide higher-resolution images with appropriate magnification and IHC quantification details (i.e., number of mice per group, number of fields per mouse etc)
•Figure 6A-C: Resolve the timeline discrepancy and provide details of the survival experiment, including the rationale for stopping at day 30 and drug preparation methods.
•Figures S2E and S4A: Statistical analyses are missing, and the results do not match corresponding main figures.
•Figure S5G: Address the lack of formal statistical analysis in the GSEA. Clearly demonstrate downregulation of HR genes after KRAS inhibition.

•Line 117 (Fig S2A): Explain why HR gene downregulation is inconsistent across cell lines (e.g., SW1990 vs. AsPC-1 and PANC-1).
•Line 124 (Fig 2E-H): Elucidate why some HR-related markers (e.g., MDC1) are unaffected.
•Line 127-129 (Fig 2): Clarify whether pan-KRAS inhibition induces HR deficiency in KRAS G12D cells.
•Line 154-156 (Fig 3): Correct inconsistencies in figure references and legends.
•Line 187 (Fig 6C): Explain discrepancies in mouse group sizes and provide details of in vivo drug preparation.

Reviewer #4

(Remarks to the Author)
I co-reviewed this manuscript with one of the reviewers who provided the listed reports. This is part of the Nature Communications initiative to facilitate training in peer review and to provide appropriate recognition for Early Career Researchers who co-review manuscripts.

Version 1:

Reviewer comments:

Reviewer #1

(Remarks to the Author)
The authors have done an excellent job addressing my comments and those of the other reviewers. Since the last incarnation of this manuscript, they have done multiple additional experiments to unravel the mechanisms behind their findings. The manuscript is much stronger with more sound conclusions. I have no further comments for the authors at this time.

Reviewer #2

(Remarks to the Author)
The revised manuscript and the authors' responses to previous comments are satisfactory.

Reviewer #3

(Remarks to the Author)
The authors have done a commendable job in addressing reviewers' concerns. I have no further question.
Only a minor issue: there is a mislabeling in the legend of figure 3 (panel C is mentioned twice and the second time actually refers to D)

Reviewer #4

(Remarks to the Author)
I co-reviewed this manuscript with one of the reviewers who provided the listed reports. This is part of the Nature

Communications initiative to facilitate training in peer review and to provide appropriate recognition for Early Career Researchers who co-review manuscripts.

Open Access This Peer Review File is licensed under a Creative Commons Attribution 4.0 International License, which permits use, sharing, adaptation, distribution and reproduction in any medium or format, as long as you give appropriate credit to the original author(s) and the source, provide a link to the Creative Commons license, and indicate if changes were made.
In cases where reviewers are anonymous, credit should be given to 'Anonymous Referee' and the source.
The images or other third party material in this Peer Review File are included in the article's Creative Commons license, unless indicated otherwise in a credit line to the material. If material is not included in the article's Creative Commons license and your intended use is not permitted by statutory regulation or exceeds the permitted use, you will need to obtain permission directly from the copyright holder.
To view a copy of this license, visit https://creativecommons.org/licenses/by/4.0/

REVIEWER #1:

In this well written manuscript, the authors first tested the role of KRAS G12D inhibition on the DNA repair pathway in KRAS mutated cells (via RAD51 foci clearance rate after ionizing radiation) after which they treated immunocompromised and immunocompetent mice with vehicle, olaparib, KRAS G12D inhibition or combination therapy. In both models, interestingly, the combination treatment resulted in a prolonged OS of the animals without overt signs of untenable toxicity in the animals.

RESPONSE: We thank the reviewer for the positive and encouraging evaluation and for highlighting the improved overall survival without overt toxicity in both immunodeficient and immunocompetent models.

COMMENT 1:Do the authors have a hypothesis as to why the change in HR pathways was only observed in KRAS G12d mutated cell lines, while HR pathways of lines with KRAS G12V or KRAS G12C were unaffected by the pan-RAS inhibitor?

RESPONSE 1: We appreciate this insightful question. Based on our updated data, we proposal a two-arm model of KRAS control over HR that reconciles the apparent allele specificity:

Arm 1: Shared, ERK1/2–cell-cycle–dependent regulation (allele-independent under optimal dosing)

Initially, we observed minimal HR suppression in $KRAS^{G12V}$ or $KRAS^{G12C}$ cell lines treated with the pan-RAS inhibitor BI-2865. Upon further optimization, we found that the BI-2865 dose used in earlier experiments was suboptimal. After re-titration to 1–5 μM for 24–48 hours, BI-2865 achieved robust target engagement, with >80% suppression of pERK and pAKT across KRAS G12D, G12V, and G12C mutant lines (**Fig. S4A–C, N**).Under these optimized conditions, pan-RAS inhibition reduced

S-phase entry by ~30–45% (EdU⁺) (**Fig. S8C**) and downregulated S-phase–enriched HR genes (BRCA1, RAD51, RPA32), with concordant loss of DR-GFP HR activity across all mutant lines (**Fig. S4A–C, K–P**). These findings indicate a shared KRAS-dependent mechanism in which robust MAPK pathway blockade suppresses HR indirectly via curtailed S-phase progression.

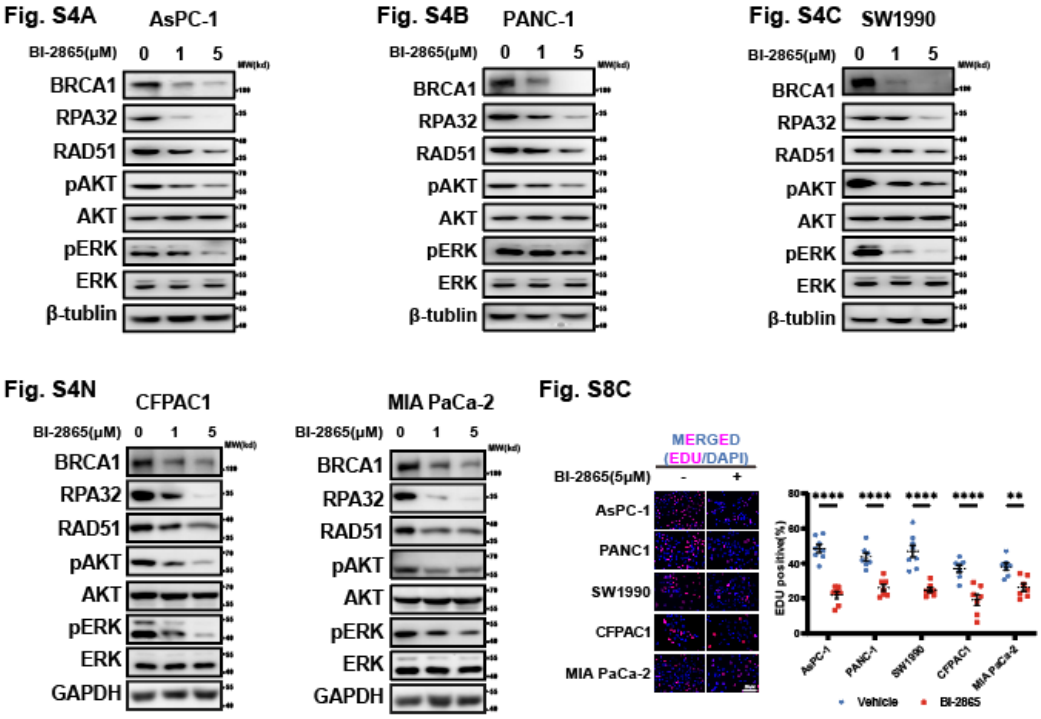

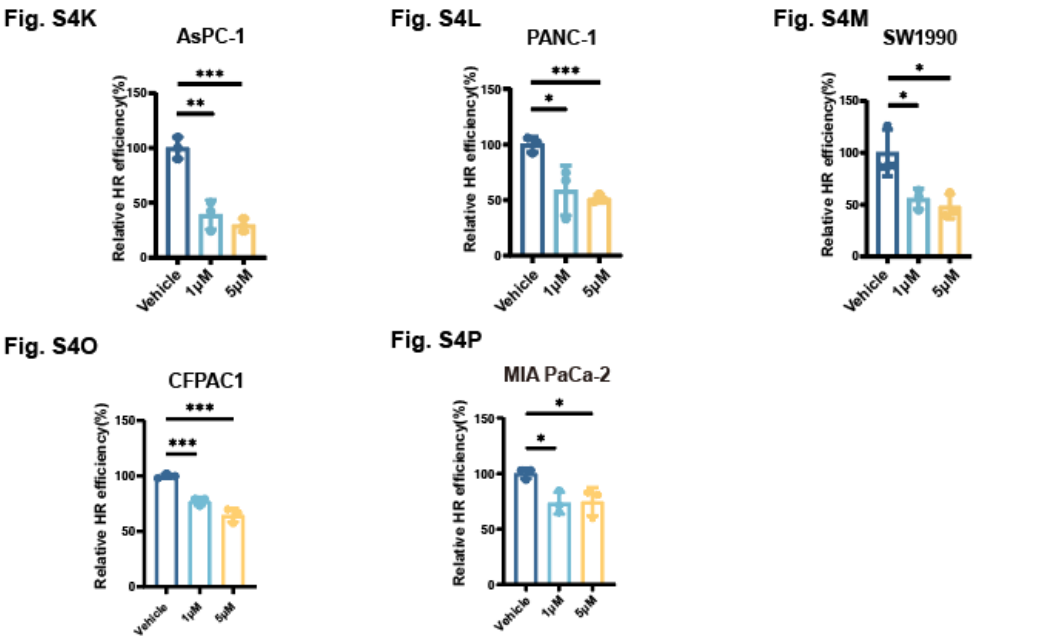

Supplementary Figure 4A-C. Western blot analysis of BRCA1, RPA32, RAD51, total ERK, total AKT, phospho-ERK, and phospho-AKT protein levels in $KRAS^{G12D}$ pancreatic cancer cell lines AsPC-1(A), PANC-1(B) and SW1990(C) treated with vehicle (DMSO) or BI-2865 at the indicated concentrations for 24 hours. Cell lysates were collected for immunoblotting. β-Tubulin served as the loading control.

Supplementary Figure 4N. Western blot analysis of BRCA1, RPA32, RAD51, total ERK, total AKT, phosphor-ERK and phosphor-AKT in CFPAC1(G12V) and MIA PaCa-2(G12C) cells treated with vehicle (DMSO), BI-2865 at indicated concentrations for 24h. Cell lysate were collected for immunoblotting for BRCA1, RPA32, RAD51, phosphor-ERK and phosphor-AKT. GAPDH served as the loading control.

Supplementary Figure 8C. G1/S phase staining in BI-2865 treated cell lines. Representative images of EdU (5-ethynyl-2'-deoxyuridine) staining for G1/S phase detection in pancreatic cancer cell lines at 24 hours following treatment with 5μM BI-2865. Quantification of EdU-positive cells indicating G1/S phase progression. Data are presented as scatter plots showing mean ± SEM with individual biological replicates. Statistical significance was determined by unpaired, two-tailed Student's t-test for each cell line. Scale bar: 50 μm. (**P<0.01, ****P<0.0001).

Supplementary Figure 4K-M. Inhibition of $KRAS^{G12D}$ by BI-2865 decreased HR repair efficiency in $KRAS^{G12D}$ pancreatic cancer cells. AsPC-1(K), PANC-1(L), and SW1990(M) were treated with BI-2865(1μM, 5μM). Efficiency was measured using DR-GFP reporter assay system. Data are shown as the mean ± SEM. Statistical significance of differences compared to vehicle control was determined by unpaired Student's t-test (*P<0.05, **P<0.01, ***P<0.001).

Supplementary Figure 4O-P. Inhibition by BI-2865 decreased HR repair efficiency in non-$KRAS^{G12D}$ pancreatic cancer cells. CFPAC1(G12V) and MIA PaCa-2(G12C) cell lines were treated with BI-2865(1μM, 5μM). Efficiency was measured using DR-GFP reporter assay system. Data are shown as the mean ± SEM. Statistical significance of differences compared to vehicle control was determined by unpaired Student's t-test (*P<0.05, **P<0.01, ***P<0.001).

Arm 2: A KRAS^{G12D}-specific, cell cycle–independent arm

To uncover allele-specific regulation beyond cell-cycle effects, we synchronized cells at the G1/S boundary using hydroxyurea (HU) and verified synchronization via EdU incorporation. Under these matched conditions, the KRAS^{G12D}-selective inhibitor MRTX1133 significantly suppressed HR gene transcripts, protein expression, and foci formation only in KRAS^{G12D}-mutant lines (**Fig. S7A–M**). In contrast, synchronized KRAS^{G12V} and KRAS^{G12C} cells treated with BI-2865 showed no reduction in HR protein expression, despite equivalent suppression of pERK and pAKT (**Fig. S8D–F**). These results suggest that KRAS^{G12D} uniquely sustains HR gene expression via a mechanism independent of MAPK signaling and cell-cycle control. Supporting this, ectopic expression of KRAS^{G12D} in KRAS wild-type BxPC-3 cells induced a stronger upregulation of HR-related transcripts compared to G12V or G12C (**Fig. S8B**), consistent with a heightened intrinsic HR program and increased dependence on HR machinery in KRAS^{G12D}-expressing cells.

Collectively, the initial lack of HR suppression in KRAS$^{G12V/C}$ cells in our previous experiment is likely stemmed from suboptimal BI-2865 exposure. With optimized dosing, pan-RAS inhibition suppresses HR via a cell-cycle–dependent mechanism common to all KRAS mutant alleles. However, KRAS^{G12D} inhibition additionally engages a unique, cell-cycle–independent mechanism that directly regulates HR gene expression. This dual-arm model explains the more consistent and robust HR suppression observed in KRAS^{G12D} cells and provides a mechanistic rationale for the selective synthetic lethality we observe with KRAS^{G12D} and PARP co-inhibition.

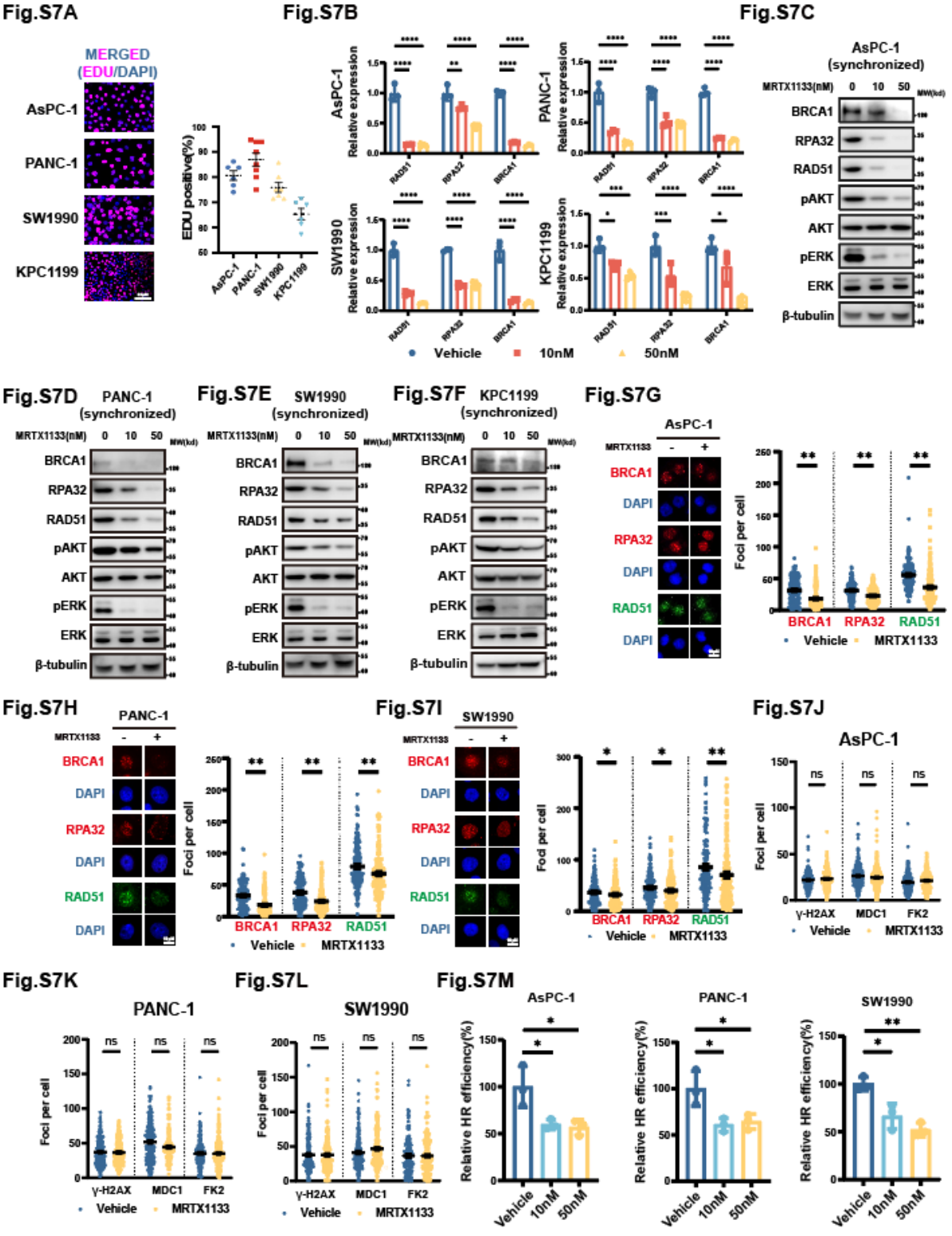

Supplementary Figure 7A. Synchronization efficiency in KRAS^{G12D} mutant cells. Representative images of EdU staining in four KRAS^{G12D} mutant pancreatic cancer cell lines (AsPC-1, PANC-1, SW1990 and KPC1199) following synchronization by hydroxyurea (HU),

accompanied by quantification of EdU-positive cell rates using ImageJ software. Data are shown as the mean ± SEM (n > 100 cells per time point from > 5 fields per group).

Supplementary Figure 7B. MRTX1133 downregulated the expression of homologous recombination-related genes in synchronized $KRAS^{G12D}$ mutant cells. Four synchronized pancreatic cancer cell lines (AsPC-1, PANC-1, SW1990, and KPC1199) were treated with vehicle, 10 nM, or 50 nM of MRTX1133 for 24 hours. The relative mRNA expression levels of key homologous recombination (HR) pathway genes, including RAD51, RPA32, and BRCA1, were determined by RT-qPCR. Expression levels were normalized to β-actin and are presented as fold change relative to the vehicle-treated group. Data are shown as mean ± SEM. Statistical significance was determined by one-way ANOVA. (*P<0.05, **P<0.01, ***P<0.001, ****P<0.0001).

Supplementary Figure 7C-F. Western blot analysis of BRCA1, RPA32, RAD51, phospho-ERK, and phospho-AKT protein levels in synchronized AsPC-1 (C), PANC-1 (D), SW1990 (E), and KPC1199 (F) treated with vehicle (DMSO) or MRTX1133 at the indicated concentrations for 24 hours. Cell lysates were collected for immunoblotting. β-Tubulin served as the loading control.

Supplementary Figure 7G-I. Immunofluorescence detection of HR marker foci in synchronized $KRAS^{G12D}$ PDAC cell lines treated with MRTX1133. Assessment of HR marker foci formation in synchronized AsPC-1 (G), PANC-1 (H), and SW1990 (I) cells treated with MRTX1133(50nM) ,at 1 h after 2Gy X-ray irradiation treatment (BRCA1) or at 6 h after 10Gy X-ray irradiation treatment (RPA32 and RAD51). Data were analyzed by the unpaired Student's t-test for significance. Black bars indicate the mean value from ≥ 100 cells. *P<0.05, **P<0.01, ***P<0.001. Mean ± SEM shown. The scale bar indicates 10 μm.

Supplementary Figure 7J-L. Immunofluorescence assay for DNA damage marker in synchronized $KRAS^{G12D}$ PDAC cell lines. Quantification data for γH2AX, MDC1 and FK2 foci formation in the AsPC-1 (J), PANC-1 (K), and SW1990 (L) with and without MRTX1133 treatment (50nM) at 1 h after 2Gy X-ray irradiation treatment (γ-H2AX, MDC1 and FK2). Statistical significance of differences was determined by unpaired Student's t-test (Ns represents no significant). Black bars indicate the mean value from > 100 cells. Mean ± SEM shown.

Supplementary Figure 7M. Inhibition of $KRAS^{G12D}$ effected HR repair efficiency in synchronized pancreatic cancer cells. AsPC-1, PANC-1, and SW1990 were treated with MRTX1133(10nM, 50nM). Efficiency was measured using DR-GFP reporter assay system. Data are shown as the mean ± SEM. Statistical significance of differences compared to vehicle control was determined by unpaired Student's t-test (*P<0.05, **P<0.01).

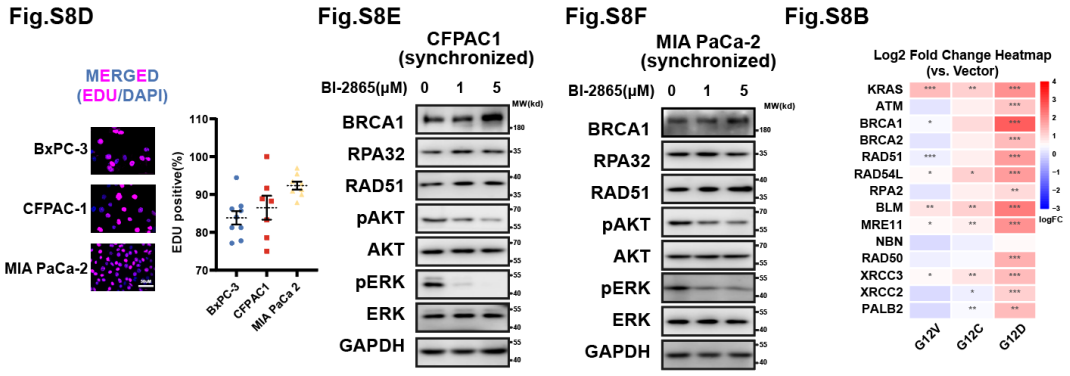

Supplementary Figure 8D. Synchronization efficiency in non-KRAS^{G12D} mutant cells. Representative images of EdU staining in BxPC-3(WT), CFPAC1(G12V) and MIA PaCa-2(G12C) cell lines following synchronization, accompanied by quantification of EdU-positive cell rates using ImageJ software. Data are shown as the mean ± SEM (n > 100 cells per time point from > 5 fields per group).

Supplementary Figure 8E-F. Western blot analysis of BRCA1, RPA32, RAD51, phosphor-AKT and phosphor-ERK in synchronized non-G12D pancreatic cell lines CFPAC1(E) and MIA PaCa-2(F) using HU block and treated with vehicle (DMSO), BI-2865 at indicated concentrations for 24h. Cell lysate were collected for immunoblotting for BRCA1, RPA32, RAD51, phosphor-AKT and phosphor-ERK. GAPDH served as the loading control.

Supplementary Figure 8B. Heatmap showing the log2 fold change (logFC) in mRNA expression of HR pathway genes in BxPC-3 cells overexpressing different KRAS mutants compared to a vector control. Data were obtained from RT-qPCR. Statistical significance was determined by Student's t-test for each mutant vs. control. (*P < 0.05, **P < 0.01, ***P < 0.001).

COMMENT 2. For the sake of completeness, the authors might consider treating the KRAS G12D cell lines with olaparib alone to ensure that the PARPi alone would not (albeit unexpectedly) result in decreased cell viability.

RESPONSE 2: We appreciate this valuable suggestion. To address it, we treated $KRAS^{G12D}$-mutant PDAC cell lines (PANC-1, AsPC-1, and SW1990) with olaparib alone (1 μM and 10 μM, 72 h) and quantified cell viability using CCK-8 assays. The resulting dose–response curves confirmed that olaparib monotherapy had minimal effects on overall cell growth within the concentration range used in our study **(Figure. S9J)**. These results verify that the biological outcomes observed under MRTX1133 + olaparib treatment reflect a true combinatorial effect rather than responses to PARP inhibition alone. The new data have been incorporated in the revised manuscript **(Figure. S9J**).

Fig. S9J

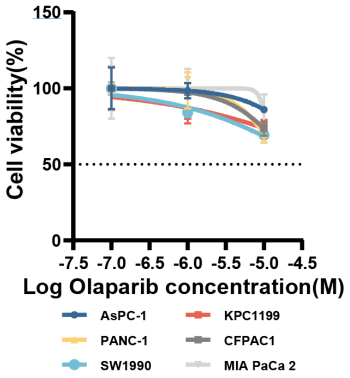

Supplementary Figure 9J. Sensitivity of PDAC cell lines to olaparib monotherapy. Dose-response curves of 6 PDAC cells lines treated with increasing concentrations of olaparib for 72 hours, measured by CCK8 assay.

COMMENT 3. Although the results are interesting preliminarily, it would behoove the authors to provide substantially more mechanistic insights into the combination of KRAS and PARPi therapy. For example, showing CD8 and CC3 increase with the combination of drugs does not in any way prove that there is T-cell mediated killing. Without additional mechanism insights, I do not think that this paper has sufficient interest for Nature Comm readership.

RESPONSE 3: We fully agree with the reviewer that demonstrating increased $CD8^+$ T-cell infiltration and cleaved caspase-3 (CC3) alone does not establish T-cell–mediated cytotoxicity. To directly address this, we performed additional mechanistic studies integrating single-cell transcriptomic profiling, flow cytometry, and $CD8^+$ T-cell depletion experiments, which collectively confirm a $CD8^+$ T-cell–dependent mechanism underlying the therapeutic synergy between KRAS inhibition and PARP blockade.

1. **Single-cell RNA sequencing reveals $CD8^+$ T-cell expansion and activation.**

   We conducted scRNA-seq of tumors from mice treated with vehicle, MRTX1133, olaparib, or the combination. Unsupervised clustering identified 24 cell populations, with a marked expansion of T/NK and myeloid compartments under combination treatment (**Fig. 8A–B; Fig. S13F, G**). Within the T/NK lineage, the combination group exhibited a significant enrichment of cytotoxic $CD8^+$ effector and activated $CD4^+$ T cells (**Fig. 8C–D; Fig. S13H, I**). Gene-set enrichment analyses further demonstrated upregulation of pathways associated with T-cell-mediated cytotoxicity, interferon-γ signaling, and inflammatory response (**Fig. 8E**), indicating robust activation of adaptive immunity.

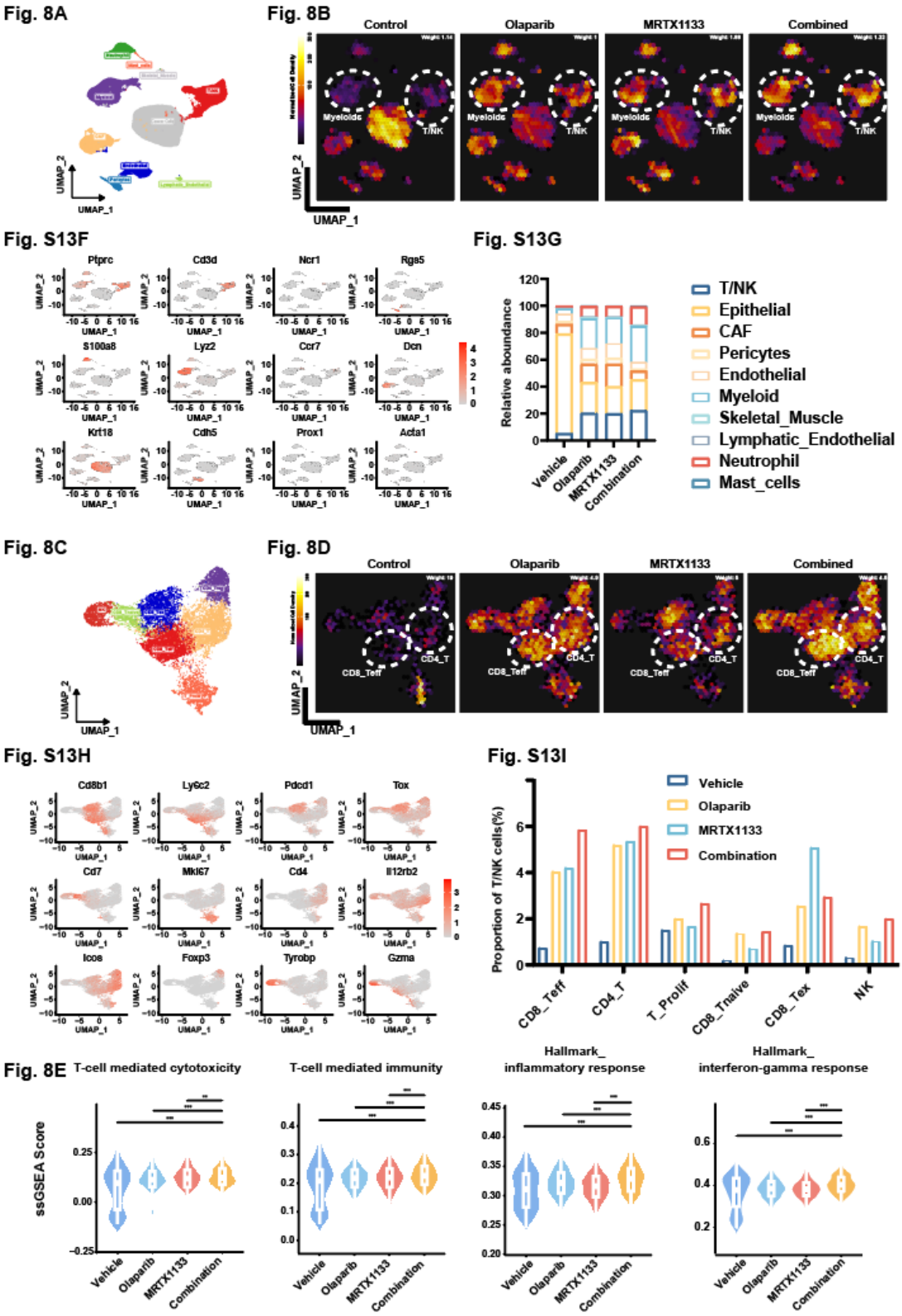

Figure 8A. Uniform Manifold Approximation and Projection (UMAP) plot of all identified cell types from pooled single-cell RNA sequencing data. Cells were sourced from KPC-1199 tumors grown in C57BL/6J mice and treated with vehicle, olaparib, MRTX1133, or

the combination for 7 days. Color coding indicates distinct cell clusters. CAF: Cancer-Associated Fibroblast.

Figure 8B. UMAP density plots comparing the distribution and density of major immune cell compartments across the four treatment groups. Normalized cell density is visualized by color (purple: low, yellow: high). Annotated clusters indicate major immune cell types, including T/NK (T and Natural Killer) cells and Myeloid cells.

Supplemental Figure 13F. UMAP feature plots showing the expression of canonical marker genes used to identify major cell lineages within the tumor microenvironment.

Supplemental Figure 13G. Stacked bar chart showing the relative abundance of major cell populations across the four treatment groups, as determined from the scRNA-seq data.

Figure 8C. UMAP plot showing the refined sub-clustering of the T and Natural Killer (T/NK) cell populations identified in (Figure 8A).

Figure 8D. UMAP density plots comparing the distribution of T cell subsets across the four treatment groups. Annotated clusters highlight key T cell subtypes, including CD8_Teff (CD8+ effector T cells) and CD4_T (CD4+ T cells).

Supplemental Figure 13H. UMAP feature plots displaying the expression of key marker genes used to further define T-cell and NK-cell subsets.

Supplemental Figure 13I. Bar chart showing the proportion of specific T-cell and NK-cell subsets as a percentage of the total T/NK cell population in each treatment group. (Teff: effector T-cell; T_Prolif: proliferating T-cell; Tnaive: naive T-cell; Tex: exhausted T-cell).

Figure 8E. Violin plots showing single-sample Gene Set Enrichment Analysis (ssGSEA) scores for four key immune-related signatures across the treatment groups. In each plot, the white dot represents the median, and the thick bar indicates the interquartile range. Statistical significance was determined by one-way ANOVA. **P<0.01, ***P<0.001.

2. Flow cytometry validates functional T-cell activation.

Flow-cytometric analysis of dissociated tumors confirmed significant increases in $CD8^+$ and $CD4^+$ T-cell infiltration in the combination group compared to monotherapy (**Fig. 8F**). Moreover, $CD8^+$ T cells displayed elevated TNF-α expression (**Fig. 8G**) and reduced PD-1 levels (**Fig. 8H**), signifying enhanced cytotoxic activity and decreased exhaustion.

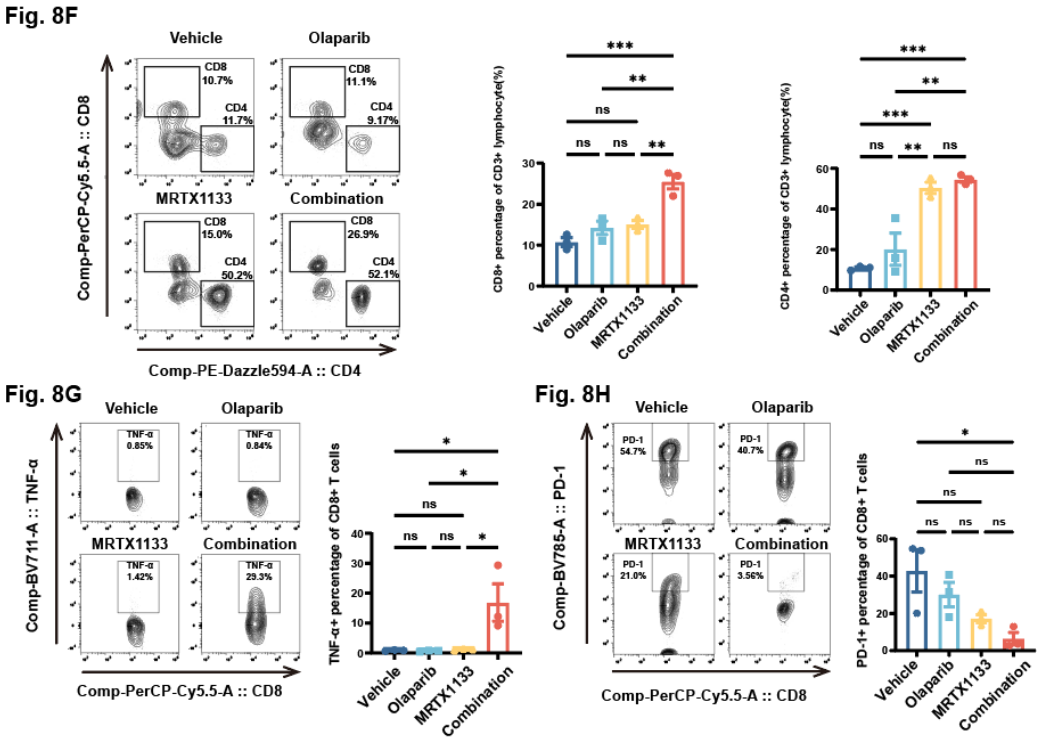

Figure 8F. Representative flow cytometry plots (left) and quantification (right) of CD4+ and CD8+ T cells within the total CD3+ lymphocyte population in tumors. For quantification, the bar graph represents the mean ± SEM, with individual data points from each mouse shown (n=3 per group). Statistical significance was determined by one-way ANOVA (**P < 0.01, ***P < 0.001, ns, no significant).

Figure 8G. Representative flow cytometry plots (left) and quantification (right) showing the percentage of TNF-α-producing cells within the CD8+ T cell population. For quantification, the bar graph represents the mean ± SEM, with individual data points from each mouse shown. Statistical significance was determined by one-way ANOVA (*P < 0.05, ns, no significant).

Figure 8H. Representative flow cytometry plots (left) and quantification (right) showing the percentage of PD-1-expressing cells within the CD8+ T cell population. For quantification, the bar graph represents the mean ± SEM, with individual data points from each mouse shown. Statistical significance was determined by one-way ANOVA(*P < 0.05, ns, no significant).

3. $CD8^+$ T-cell depletion abolishes combination efficacy.

To determine causality, we performed in vivo CD8⁺ T-cell depletion using anti-CD8α antibodies in immunocompetent mice bearing KPC1199 tumors. Depletion significantly attenuated the antitumor effect of MRTX1133 + olaparib, as evidenced by restored tumor growth and increased tumor weight relative to IgG-treated controls (**Fig. 9J-M**). These results conclusively demonstrate that CD8⁺ T cells are essential mediators of the therapeutic response to combined KRAS and PARP inhibition.

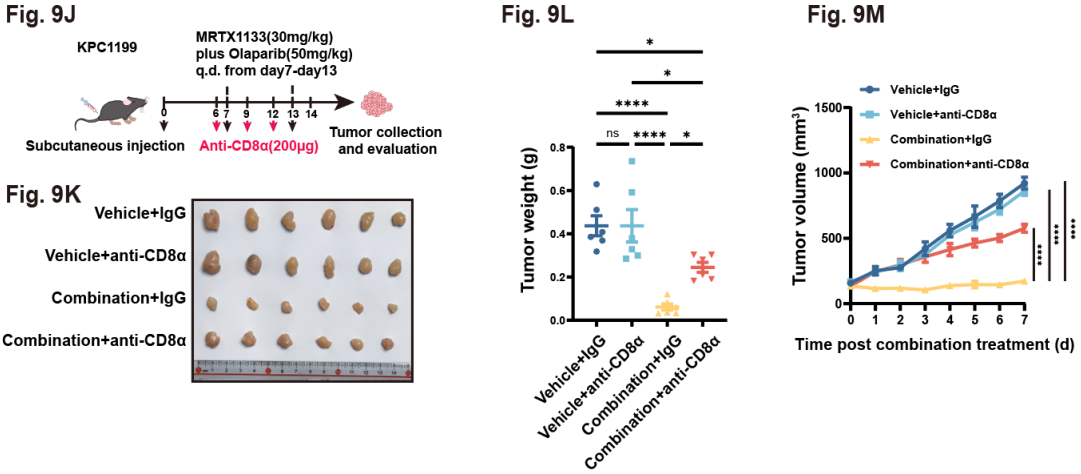

Figure 9J. Schematic of the dosing regimen for the CD8+ T cell depletion study in the subcutaneous KPC1199 tumor model. Immunocompetent C57BL/6J mice were subcutaneously inoculated with KPC1199 cells on day 0 to establish syngeneic tumors. CD8+ T cell depletion was initiated on day 6 with intraperitoneal administration of anti-CD8 antibodies (200 μg/dose) or isotype controls, repeated every 3 days throughout the study. Combination therapy with MRTX1133 (30 mg/kg intraperitoneal daily) and Olaparib (50 mg/kg intraperitoneal daily) commenced on day 7 and continued for 7 days (day7-day13). Vehicle controls were administered in parallel. Tumor volumes were monitored every day until the endpoint on day 14, at which point tumors were harvested for weight measurement and further analyses.

Figure 9K. Representative images of harvested tumors from the CD8+ T cell depletion study at the experimental endpoint (Day 14).

Figure 9L-M. Tumor weight (L) and volume (M) of mice bearing KPC1199. Mice were treated with vehicle+IgG(200 μg),vehicle+anti-CD8α(200 μg), combination(Olaparib 50 mg /kg; qd, MRTX1133 30mg/kg; qd)+IgG(200 μg), combination+anti-CD8α(200 μg). 6 animals per group. Statistical significance was determined by one-way ANOVA for (L) and two-way ANOVA for (M). Data are represented as the Mean ± SEM. *P<0.05, ****P<0.0001; ns, no significant.

These new datasets provide direct evidence that the combination of KRAS^{G12D} and

PARP inhibition enhances antitumor immunity through $CD8^+$ T-cell–driven cytotoxicity, beyond additive effects on apoptosis or DNA damage. The expanded mechanistic framework—incorporating immune activation, single-cell resolution profiling, and functional depletion studies—substantially strengthens the biological insight and translational relevance of our study for *Nature Communications* readership.

Reviewer #2 (Remarks to the Author):

The authors of this manuscript reported a new therapeutic strategy by combining PARPis and KRASG12D inhibitors to target pancreatic ductal adenocarcinoma (PDAC). Mechanistically, KRASG12D inhibitor reduces HR repair protein expression including BRCA1, RAD51 and RPA32 and thus impairs HR repair

capacity, sensitizing to PARPi treatment in multiple in vitro and in vivo PDAC models including CDX, PDX and syngeneic mouse models. Overall, The strength of this manuscript is providing a therapeutic strategy by combining PARPis and KRASG12D inhibitors, which can be readily translated into clinical testing. Results from mouse models clearly demonstrated efficacy of this combination strategy. There are several concerns regarding the mechanistic understanding of the combination treatment and also the clinical applications.

RESPONSE: We thank the reviewer for the positive and constructive feedback.

COMMENT 1. RAS/Raf/MEK/ERK and PI3K/ATKT/mTOR pathways are downstream of KRAS activation. The therapeutic efficacy of combining inhibitors of these two pathways (RAS/Raf/MEK/ERK and PI3K/ATKT/mTOR) have been studied and demonstrated in multiple cancer types such as ERK inhibitors, PI3K inhibitors and mTOR inhibitors. As KRASG12D inhibitors only target a specific KRAS activation mutation in a small subset of patients. What is the advantage of using KRASG12D inhibitors in combination with PARPis compared to these existing strategies targeting downstream signaling of KRAS activation regardless of specific mutation sites. Perhaps, this specific inhibitor targeting KRASG12D in combination of PARPis may reduce potential toxicity of combining inhibitors targeting RAS/Raf/MEK/ERK and PI3K/ATKT/mTOR in normal cells.

RESPONSE 1: We thank the reviewer for this thoughtful comment, which raises an important point regarding the therapeutic rationale and clinical positioning of combining $KRAS^{G12D}$-specific inhibition with PARP blockade.

We agree that inhibition of downstream signaling pathways—including MEK, PI3K, and mTOR—has demonstrated efficacy across multiple tumor types, but such agents often cause significant on-target toxicity in normal tissues due to their suppression of essential signaling networks required for normal cellular function. In contrast, $KRAS^{G12D}$ inhibitors such as MRTX1133 are designed to selectively target the oncogenic allele while sparing wild-type KRAS and downstream signaling in normal

cells. We therefore hypothesized that $KRAS^{G12D}$-specific inhibition combined with PARP inhibition could maintain anti-tumor efficacy while minimizing toxicity compared with broad downstream cotargeting.

To test this, we directly compared the effects of MRTX1133 + olaparib versus trametinib + alpelisib (MEK + PI3K inhibition) in normal epithelial cells (BEAS-2B and hTERT-HPNE). Both combinations reduced cell proliferation, but trametinib + alpelisib caused significantly greater growth inhibition than MRTX1133 + olaparib (**Fig. S9C–D**).

These findings support the reviewer's hypothesis that $KRAS^{G12D}$-specific targeting offers a superior therapeutic window. By selectively inhibiting the mutant allele rather than broadly blocking downstream pathways essential for normal cell homeostasis, the combination of $KRAS^{G12D}$ inhibition with PARP blockade achieves greater tumor selectivity with reduced collateral toxicity. The new data have been added to **Supplementary Fig. S9C–D**, and the Discussion has been revised to highlight this mechanistic and translational advantage.

Fig. S9C

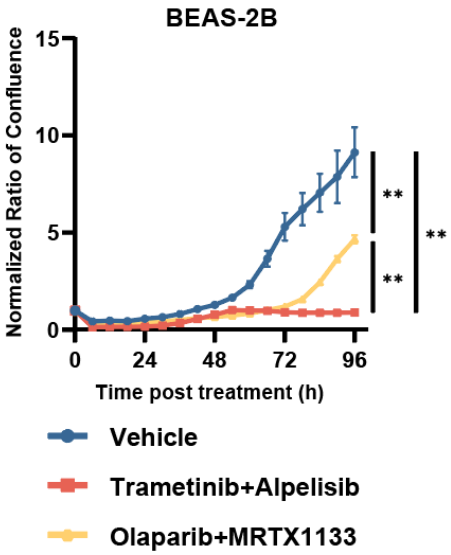

Fig. S9D

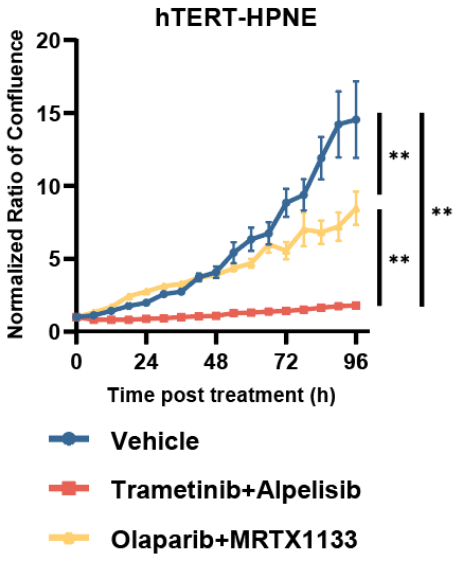

Supplementary Figure 9C-D. The combination of Olaparib and MRTX1133 shows minimal toxicity to non-cancerous cells. Real-time proliferation curves for human bronchial epithelial cells BEAS-2B (C) and pancreatic ductal epithelial cells hTERT-HPNE (D) were monitored by Incucyte. Cells were treated with concentrations used in cancer cells [Vehicle (0.1%DMSO), Trametinib （50nM） +Alpelisib (50nM), Olaparib (100nM)+MRTX1133(50nM)], and cell proliferation was monitored over 96 hours using Incucyte live-cell imaging. Data are presented as mean ± SEM. Statistical significance was assessed using two-way ANOVA. **P<0.01.

COMMENT 2. Inhibition of RAS/Raf/MEK/ERK or PI3K/ATKT/mTOR pathway has been shown to regulate key DNA repair proteins and DNA damage response signaling molecules in previous studies. It is not surprising to observe that KRASG12D inhibitors can also reduce multiple HR-related proteins. The mechanistic findings of KRASG12D inhibitors in HR regulation is logically expected due to these existing data, which diminish the novelty of this report.

RESPONSE 2: We thank the reviewer for this insightful comment. We agree that suppression of DNA repair pathways by inhibition of the RAS/RAF/MEK/ERK and PI3K/AKT/mTOR cascades has been previously documented, primarily through cell-cycle–dependent regulation of HR factors. However, our study identifies two previously unreported and mechanistically distinct features of $KRAS^{G12D}$ inhibition that extend beyond these known effects:

1. **$KRAS^{G12D}$-specific, cell-cycle–independent regulation of HR.**

We demonstrate that $KRAS^{G12D}$ inhibition uniquely suppresses HR gene expression and function even under synchronized cell-cycle conditions, where S-phase–dependent effects are eliminated. In synchronized $KRAS^{G12D}$-mutant cells, MRTX1133 markedly reduced BRCA1, RAD51, and RPA32 expression and foci formation (**Fig. S7A–M**), whereas BI-2865 or MEK/PI3K inhibition in KRASG12V/C cells failed to do so despite equivalent ERK and AKT suppression (**Fig. S8D–F**). This reveals a $KRAS^{G12D}$-specific, cell-cycle–independent mechanism that directly regulates HR gene expression—an effect not observed with inhibition of general downstream KRAS effectors.

2. **Decoupling of HR suppression from canonical MAPK/PI3K signaling.**

In MRTX1133-resistant $KRAS^{G12D}$ cell lines, downstream pERK and pAKT signaling were reactivated, yet BRCA1, RAD51, and RPA32 levels remained strongly suppressed and PARP inhibitor synergy persisted (**Fig. 6A–L; Fig. S12**). These results indicate that HR suppression is mechanistically separable from ERK/AKT pathway inhibition, implying a non-canonical $KRAS^{G12D}$-driven

mechanism for HR regulation.

Together, these results support a two-arm model in which KRAS signaling regulates HR through both a shared, MAPK- and cell-cycle–dependent pathway common to multiple KRAS variants and a $KRAS^{G12D}$-specific, cell-cycle–independent arm. This dual mechanism provides new insight into how $KRAS^{G12D}$ inhibition establishes a synthetic-lethal interaction with PARP blockade. We acknowledge that the precise molecular mediators of this $KRAS^{G12D}$-specific arm remain to be elucidated, and future work will aim to define the downstream effectors responsible for this noncanonical HR regulation. Nonetheless, our findings reveal a previously unrecognized regulatory dimension of $KRAS^{G12D}$ biology that helps explain its distinct therapeutic vulnerabilities and potential for allele-targeted combination strategies.

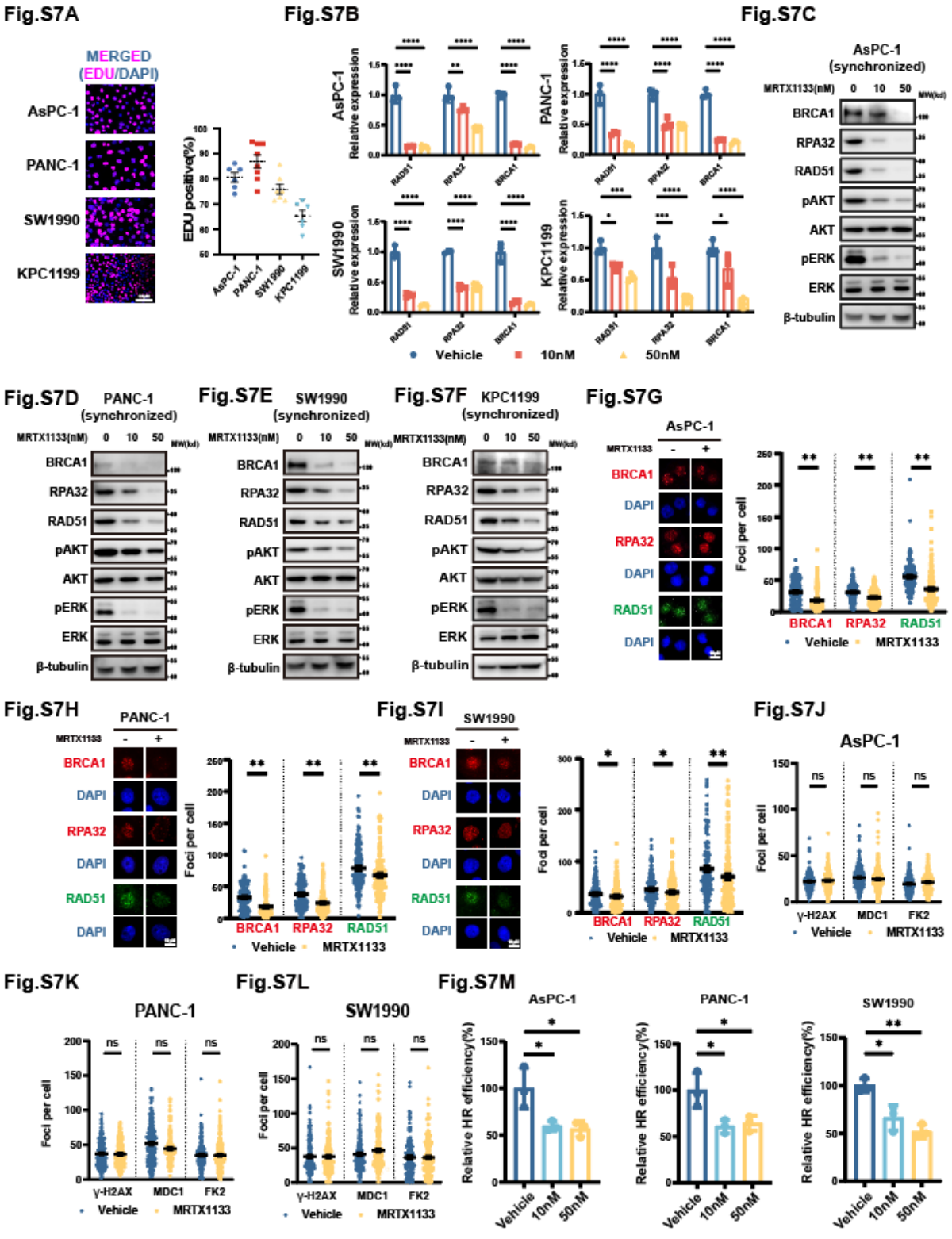

Supplementary Figure 7A. Synchronization efficiency in KRAS^{G12D} mutant cells. Representative images of EdU staining in four KRAS^{G12D} mutant pancreatic cancer cell lines (AsPC-1, PANC-1, SW1990 and KPC1199) following synchronization by hydroxyurea (HU),

accompanied by quantification of EdU-positive cell rates using ImageJ software. Data are shown as the mean ± SEM (n > 100 cells per time point from > 5 fields per group).

Supplementary Figure 7B. MRTX1133 downregulated the expression of homologous recombination-related genes in synchronized $KRAS^{G12D}$ mutant cells. Four synchronized pancreatic cancer cell lines (AsPC-1, PANC-1, SW1990, and KPC1199) were treated with vehicle, 10 nM, or 50 nM of MRTX1133 for 24 hours. The relative mRNA expression levels of key homologous recombination (HR) pathway genes, including RAD51, RPA32, and BRCA1, were determined by RT-qPCR. Expression levels were normalized to β-actin and are presented as fold change relative to the vehicle-treated group. Data are shown as mean ± SEM. Statistical significance was determined by one-way ANOVA. (*P<0.05, **P<0.01, ***P<0.001, ****P<0.0001).

Supplementary Figure 7C-F. Western blot analysis of BRCA1, RPA32, RAD51, phospho-ERK, and phospho-AKT protein levels in synchronized AsPC-1 (C), PANC-1 (D), SW1990 (E), and KPC1199 (F) treated with vehicle (DMSO) or MRTX1133 at the indicated concentrations for 24 hours. Cell lysates were collected for immunoblotting. β-Tubulin served as the loading control.

Supplementary Figure 7G-I. Immunofluorescence detection of HR marker foci in synchronized $KRAS^{G12D}$ PDAC cell lines treated with MRTX1133. Assessment of HR marker foci formation in synchronized AsPC-1 (G), PANC-1 (H), and SW1990 (I) cells treated with MRTX1133(50nM) ,at 1 h after 2Gy X-ray irradiation treatment (BRCA1) or at 6 h after 10Gy X-ray irradiation treatment (RPA32 and RAD51). Data were analyzed by the unpaired Student's t-test for significance. Black bars indicate the mean value from ≥ 100 cells. *P<0.05, **P<0.01, ***P<0.001. Mean ± SEM shown. The scale bar indicates 10 μm.

Supplementary Figure 7J-L. Immunofluorescence assay for DNA damage marker in synchronized $KRAS^{G12D}$ PDAC cell lines. Quantification data for γH2AX, MDC1 and FK2 foci formation in the AsPC-1 (J), PANC-1 (K), and SW1990 (L) with and without MRTX1133 treatment (50nM) at 1 h after 2Gy X-ray irradiation treatment (γ-H2AX, MDC1 and FK2). Statistical significance of differences was determined by unpaired Student's t-test (Ns represents no significant). Black bars indicate the mean value from > 100 cells. Mean ± SEM shown.

Supplementary Figure 7M. Inhibition of $KRAS^{G12D}$ effected HR repair efficiency in synchronized pancreatic cancer cells. AsPC-1, PANC-1, and SW1990 were treated with MRTX1133(10nM, 50nM). Efficiency was measured using DR-GFP reporter assay system. Data are shown as the mean ± SEM. Statistical significance of differences compared to vehicle control was determined by unpaired Student's t-test (*P<0.05, **P<0.01).

Fig.S8D

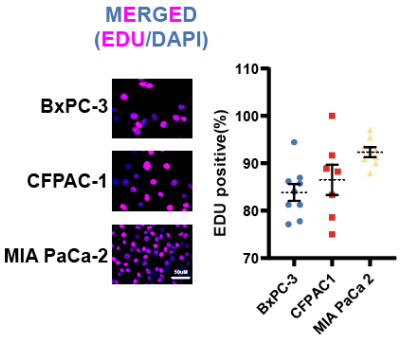

Fig.S8E

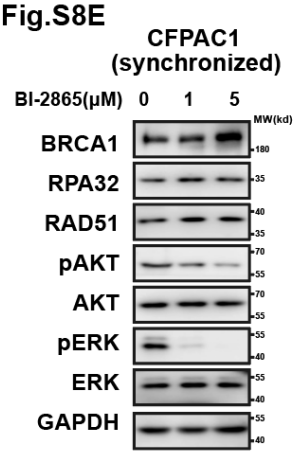

Fig.S8F

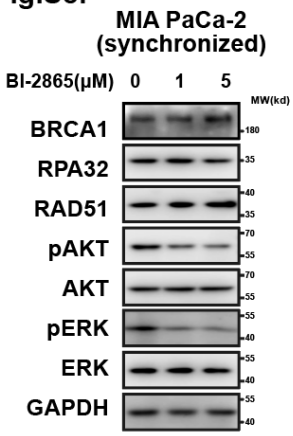

Supplementary Figure 8D. Synchronization efficiency in non-KRAS^{G12D} mutant cells. Representative images of EdU staining in BxPC-3(WT), CFPAC1(G12V) and MIA PaCa-2(G12C) cell lines following synchronization, accompanied by quantification of EdU-positive cell rates using ImageJ software. Data are shown as the mean ± SEM (n > 100 cells per time point from > 5 fields per group).

Supplementary Figure 8E-F. Western blot analysis of BRCA1, RPA32, RAD51, phosphor-AKT and phosphor-ERK in synchronized non-G12D pancreatic cell lines CFPAC1(E) and MIA PaCa-2(F) using HU block and treated with vehicle (DMSO), BI-2865 at indicated concentrations for 24h. Cell lysate were collected for immunoblotting for BRCA1, RPA32, RAD51, phosphor-AKT and phosphor-ERK. GAPDH served as the loading control.

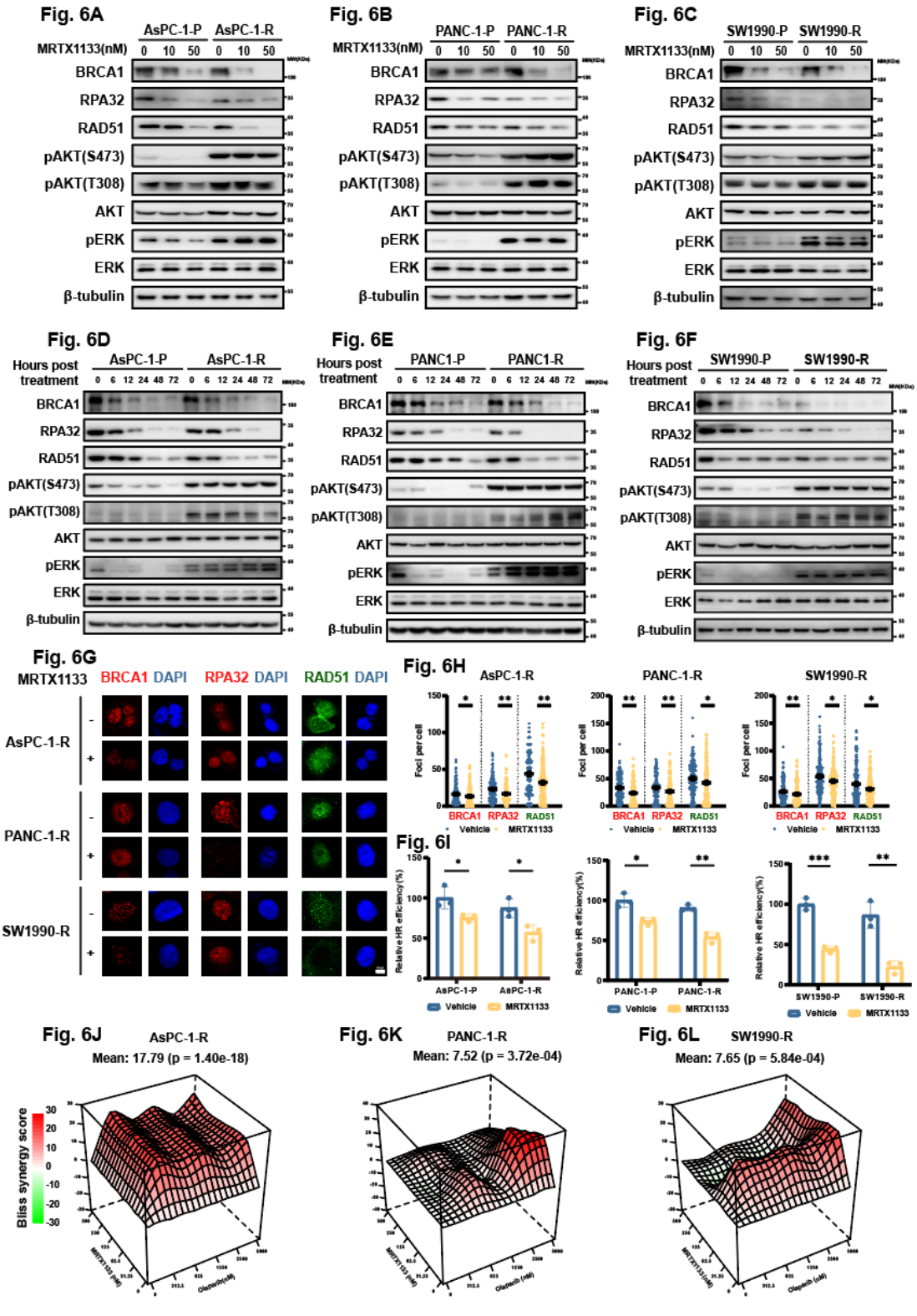

Figure 6A-C. Dose-dependent effects of MRTX1133 on HR and signaling proteins. Parental (P) and MRTX1133-resistant (R) variants of AsPC-1, PANC-1, and SW1990 cells were treated with the indicated concentrations of MRTX1133 for 24 hours. Cell lysates were analyzed by Western blot for BRCA1, RPA32, RAD51, total AKT, total

ERK, phospho-AKT (S473, T308), and phospho-ERK. β-Tubulin served as the loading control.

Figure 6D-F. Time-dependent effects of MRTX1133 on HR and signaling proteins. Parental (P) and resistant (R) cells were treated with 50 nM MRTX1133 for the indicated times (6-72 hours). Protein levels were assessed by Western blot as described above.

Figure 6G-H. Immunofluorescence assay for HR-related protein in MRTX1133-resistant KRASG12D PDAC cell lines. Representative immunofluorescence images (G) and quantification (H) of BRCA1, RPA32, and RAD51 foci in resistant cell lines are shown. For quantification, data from one representative experiment are presented as a scatter plot ($n \geq 100$ cells), with black bars indicating the mean. Statistical significance was determined by the unpaired Student's t-test (*P<0.05, **P<0.01). The experiment was repeated three times independently with similar results.

Figure 6I. MRTX1133 treatment reduces HR repair efficiency. Parental and resistant cells were treated with MRTX1133 (50 nM) for 24 hours, and HR efficiency was measured using a DR-GFP reporter assay. Data are shown as mean ± SEM of technical replicates (n=3) from one representative experiment. Statistical significance was determined by the unpaired, two-tailed Student's t-test (*P<0.05, **P<0.01, ***P<0.001). This experiment was also repeated three times with similar results.

Figure 6J-L. Synergistic anti-tumor effect of MRTX1133 combined with Olaparib in resistant pancreatic cancer cells. Three-dimensional synergy plots show the interaction between MRTX1133 and Olaparib in AsPC-1-R (J), PANC-1-R (K), and SW1990-R (L) cells after 144 hours of treatment. Red peaks indicate synergy, and green valleys indicate antagonism. The overall mean synergy score and p-value for each combination are shown in the title of each plot.

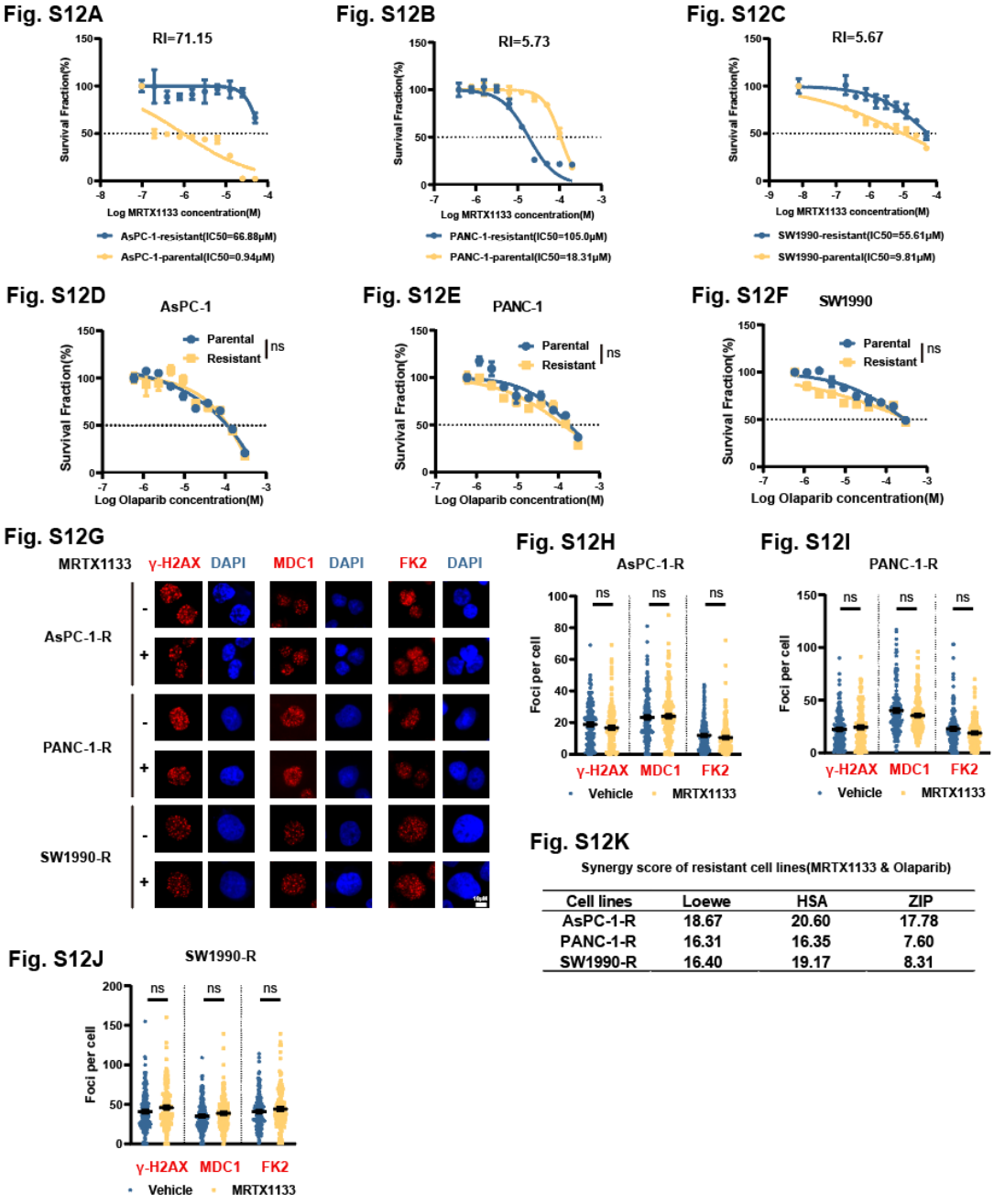

Fig. S12K

Synergy score of resistant cell lines(MRTX1133 & Olaparib)

Cell lines	Loewe	HSA	ZIP
AsPC-1-R	18.67	20.60	17.78
PANC-1-R	16.31	16.35	7.60
SW1990-R	16.40	19.17	8.31

Supplementary Figure 12A-C. Establishment and validation of MRTX1133-resistant cell lines. Dose-response curves show the increased IC50 values for MRTX1133 in resistant (-R) versus parental cell lines for AsPC-1 (A), PANC-1 (B), and SW1990 (C). The Resistance Index (RI) is the ratio of IC50 values (resistant/parental).

Supplementary Figure 12D-F. MRTX1133-resistant cells do not exhibit cross-resistance to Olaparib. Dose-response curves for Olaparib in parental versus resistant AsPC-1 (D), PANC-1 (E), and SW1990 (F) cells show no significant

difference in sensitivity after 72 hours of treatment. Data are presented as mean ± SEM, and statistical significance between curves was assessed by two-way ANOVA. Ns indicates no significant difference between parental and resistant cells.

Supplementary Figure 12G-J. Immunofluorescence assay for DNA damage marker in MRTX1133-resistant $KRAS^{G12D}$ PDAC cell lines. Representative micrographs (G) and quantification data for γ-H2AX, MDC1 and FK2 in AsPC-1-R (H), PANC-1-R (I), and SW1990-R (J) cell lines following MRTX1133 treatment(50nM). Statistical significance was determined by unpaired, two-tailed Student's t-test. Ns represents no significant.

Supplementary Figure 12K. Synergy score of Olaparib combined with MTRX1133 in resistant cell lines. Synergy score was analyzed using HSA, Loewe and ZIP models and listed in the table.

COMMENT 3. The mechanism underlying KRASG12D inhibitor-induced HR repair gene suppression is not clear.

First, it remains unknown whether the reduction in HR gene expression induced by KRASG12D inhibitor is at protein level or at transcriptional level.

RESPONSE 3： We appreciate the reviewer's insightful comments. To clarify, we have now performed quantitative RT-qPCR in $KRAS^{G12D}$-mutated pancreatic cancer cells (AsPC-1, PANC-1, SW1990 and KPC1199) treated with MRTX1133. MRTX1133 significantly reduced RAD51, RPA32, and BRCA1 mRNA (RT-qPCR)(**Fig. S2B**) with concordant decreases in protein (WB) in $KRAS^{G12D}$-mutant cells (**Fig. 2A–D**). These data demonstrate a transcriptional component to HR suppression, accompanied by protein-level reduction.

Fig. S2B

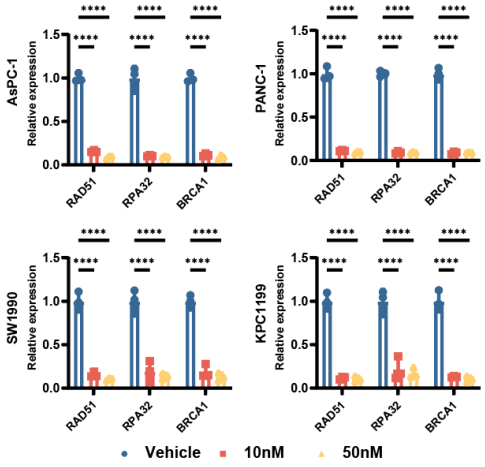

Fig. 2A

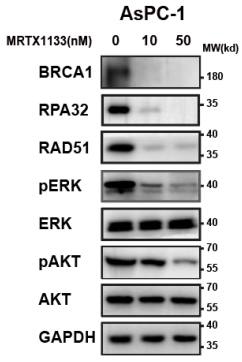

Fig. 2B

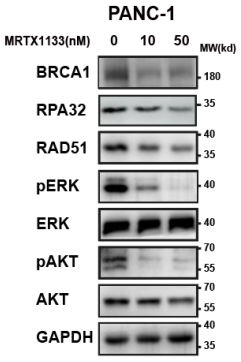

Fig. 2C

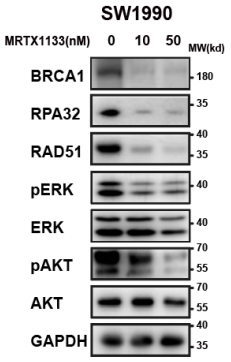

Fig. 2D

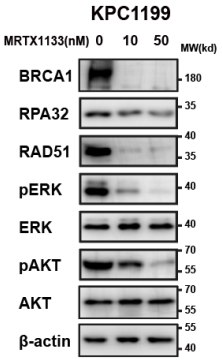

Supplementary Figure 2B. Relative mRNA expression of key HR genes (RAD51, RPA32, BRCA1) in four KRAS^{G12D} mutant cell lines treated with MRTX1133 (10 nM or 50 nM) for 24 hours. Data were determined by RT-qPCR and are presented as mean ± SEM from three biological replicates, with individual technical replicates shown as dots. Statistical significance was determined by one-way ANOVA. (****P<0.0001).

Figure 2A-D. Western blot analysis of BRCA1, RPA32, RAD51, total ERK, total AKT, phospho-ERK, and phospho-AKT in AsPC-1(A), PANC-1(B), SW1990(C), and KPC1199(D) cells treated with vehicle (DMSO) or MRTX1133 at indicated concentrations for 24h. GAPDH or β-actin served as the loading control.

Second, KRAS^{G12D} inhibitor can ablate its downstream signaling ERK1/2 and AKT, which directly regulate cell proliferation. HR repair capacity, the transcriptional expression of BRCA1, RAD51 are known associated with s phase cells. In Fig. 2SE, the authors tested the cell cycle distribution by PI staining and concluded that the reduction of HR and HR repair proteins is not resulted from cell cycle arrest. This experiment was conducted at one time point at 24 hrs. Multiple time points might provide a better assessment of the impact of KRAS^{G12D} inhibitor on cell cycle. BrdU labeling assay for S phase evaluation is more accurate than PI staining. Testing the effect of KRAS^{G12D} inhibitor in synchronized cells on HR repair protein expression could be more convincing to exclude the indirect contribution from cell cycle arrest.

RESPONSE 3： We agree with the reviewer that the single 24-hour PI analysis was insufficient to fully exclude the influence of cell-cycle changes. To address this, we performed time-course EdU incorporation assays at 24, 48, and 72 hours following MRTX1133 treatment. The proportion of EdU^{+} S-phase cells gradually decreased over time (**Fig. S6A–E**), indicating progressive cell-cycle slowing. To determine whether HR suppression persists independently of this effect, we next synchronized KRAS^{G12D}-mutant cells at the G1/S boundary using hydroxyurea (HU) and verified synchronization by EdU staining. Under these S-phase–matched conditions, MRTX1133 (50 nM, 24 h) continued to reduce BRCA1, RAD51, and RPA32 expression at both mRNA and protein levels (**Fig. S7A–F**) and significantly decreased HR-associated foci formation (**Fig. S7G–L**). Furthermore, DR-GFP assays confirmed a corresponding reduction in HR repair efficiency (**Fig. S7M**). Together, these data demonstrate that KRAS^{G12D} inhibition suppresses HR through both cell-cycle–dependent and cell-cycle–independent mechanisms, and that the observed HR repression cannot be explained solely by altered cell-cycle distribution.

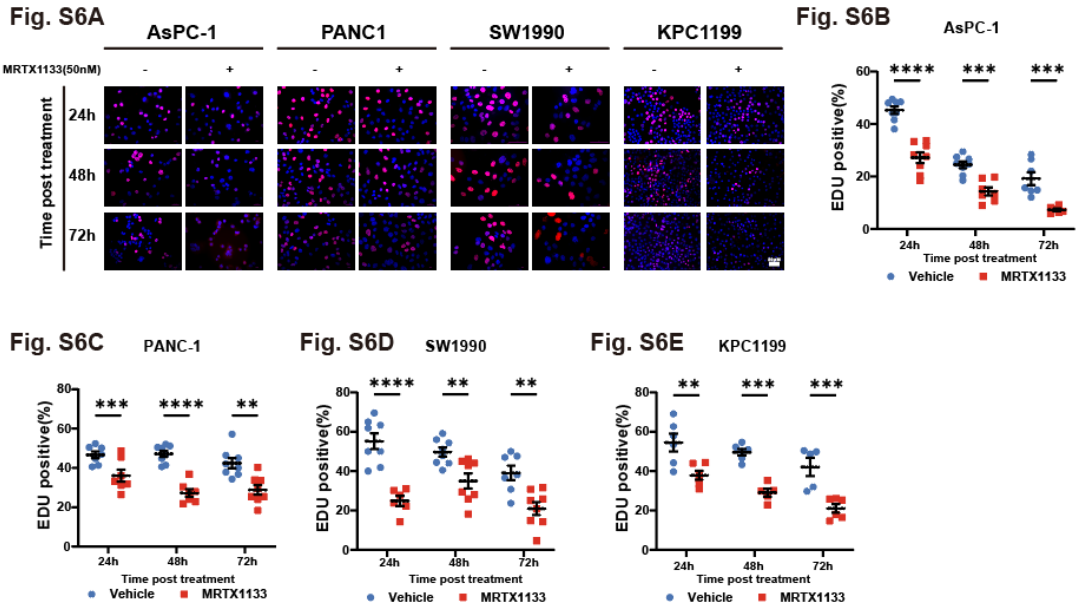

Supplementary Figure 6A. G1/S phase staining in MRTX1133-treated cell lines.(A) Representative images of EdU (5-ethynyl-2'-deoxyuridine) staining for G1/S phase detection in pancreatic cancer cell lines (AsPC-1, PANC-1, SW1990 and KPC1199) at 24, 48, and 72 hours following treatment with 50 nM MRTX1133. Scale bar: 50 μm.

Supplementary Figure 6B-E. Quantification of the percentage of EdU-positive cells for AsPC-1 (B), PANC-1 (C), SW1990 (D), and KPC1199 (E). Data are presented as scatter plots showing the mean ± SEM, with each individual point representing a biological replicate (n > 100 cells per time point from≥5 random fields per group). Statistical analysis was performed using a two-way ANOVA (**P<0.01, ***P<0.001, ****P<0.0001).

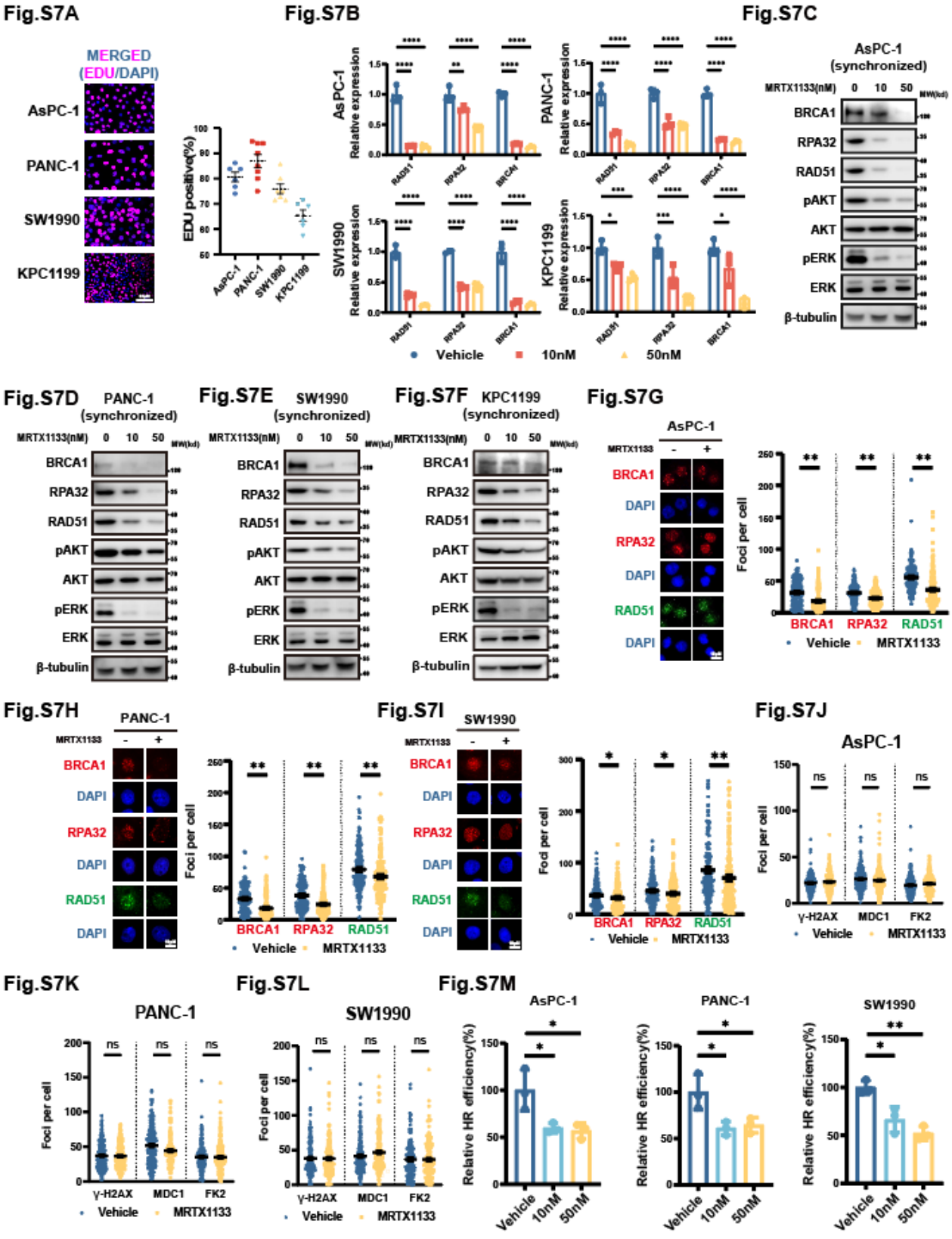

Supplementary Figure 7A. Synchronization efficiency in KRAS^{G12D} mutant cells. Representative

images of EdU staining in four $KRAS^{G12D}$ mutant pancreatic cancer cell lines (AsPC-1, PANC-1, SW1990 and KPC1199) following synchronization by hydroxyurea (HU), accompanied by quantification of EdU-positive cell rates using ImageJ software. Data are shown as the mean ± SEM (n > 100 cells per time point from > 5 fields per group).

Supplementary Figure 7B. MRTX1133 downregulated the expression of homologous recombination-related genes in synchronized $KRAS^{G12D}$ mutant cells. Four synchronized pancreatic cancer cell lines (AsPC-1, PANC-1, SW1990, and KPC1199) were treated with vehicle, 10 nM, or 50 nM of MRTX1133 for 24 hours. The relative mRNA expression levels of key homologous recombination (HR) pathway genes, including RAD51, RPA32, and BRCA1, were determined by RT-qPCR. Expression levels were normalized to β-actin and are presented as fold change relative to the vehicle-treated group. Data are shown as mean ± SEM. Statistical significance was determined by one-way ANOVA. (*P<0.05, **P<0.01, ***P<0.001, ****P<0.0001).

Supplementary Figure 7C-F. Western blot analysis of BRCA1, RPA32, RAD51, phospho-ERK, and phospho-AKT protein levels in synchronized AsPC-1 (C), PANC-1 (D), SW1990 (E), and KPC1199 (F) treated with vehicle (DMSO) or MRTX1133 at the indicated concentrations for 24 hours. Cell lysates were collected for immunoblotting. β-Tubulin served as the loading control.

Supplementary Figure 7G-I. Immunofluorescence detection of HR marker foci in synchronized $KRAS^{G12D}$ PDAC cell lines treated with MRTX1133. Assessment of HR marker foci formation in synchronized AsPC-1 (G), PANC-1 (H), and SW1990 (I) cells treated with MRTX1133(50nM) ,at 1 h after 2Gy X-ray irradiation treatment (BRCA1) or at 6 h after 10Gy X-ray irradiation treatment (RPA32 and RAD51). Data were analyzed by the unpaired Student's t-test for significance. Black bars indicate the mean value from ≥ 100 cells. *P<0.05, **P<0.01, ***P<0.001. Mean ± SEM shown. The scale bar indicates 10 μm.

Supplementary Figure 7J-L. Immunofluorescence assay for DNA damage marker in synchronized $KRAS^{G12D}$ PDAC cell lines. Quantification data for γH2AX, MDC1 and FK2 foci formation in the AsPC-1 (J), PANC-1 (K), and SW1990 (L) with and without MRTX1133 treatment (50nM) at 1 h after 2Gy X-ray irradiation treatment (γ-H2AX, MDC1 and FK2). Statistical significance of differences was determined by unpaired Student's t-test (Ns represents no significant). Black bars indicate the mean value from > 100 cells. Mean ± SEM shown.

Supplementary Figure 7M. Inhibition of $KRAS^{G12D}$ effected HR repair efficiency in synchronized pancreatic cancer cells. AsPC-1, PANC-1, and SW1990 were treated with MRTX1133(10nM, 50nM). Efficiency was measured using DR-GFP reporter assay system. Data are shown as the mean ± SEM. Statistical significance of differences compared to vehicle control was determined by unpaired Student's t-test (*P<0.05, **P<0.01).

Thirdly, the pan-KRAS inhibitor BI-2865 did not induce HR deficiency in KRAS G12V or KRAS G12C cells (Fig. S2). Does this pan-RAS BI-2865 inhibit RAS downstream signaling ERK1/2 and AKT in these cells? Is inhibition of RAS downstream signaling required or sufficient for the reduction of HR repair expression by KRASG12D inhibitor?

RESPONSE 3： We thank the reviewer for raising this important mechanistic point. We clarify that our initial BI-2865 dose was suboptimal, as acknowledged in the revised manuscript. After optimizing exposure (BI-2865, 1–5 μM, 24–48 h), we achieved >80% suppression of pERK and pAKT in KRAS G12D, G12V, and G12C cells (**Fig. S4A–C, S4N**), confirming robust downstream inhibition. In asynchronous cultures, BI-2865 reduced S-phase entry (EdU) and partially downregulated HR genes across all alleles (**Fig. S8C, S4A–C, S4N**); similarly, MEK inhibition lowered BRCA1/RAD51/RPA32 (**Fig. S5B–G**). These findings indicate that suppression of RAS downstream signaling is sufficient to reduce HR gene expression through a shared, cell-cycle–dependent mechanism.

However, in G1/S-synchronized $KRAS^{G12V/G12C}$ cells, BI-2865—despite equivalent inhibition of ERK/AKT—failed to decrease HR proteins (**Fig. S8D–F**), showing that MAPK/PI3K inhibition alone is not sufficient to repress HR when cell-cycle effects are controlled. In contrast, in $KRAS^{G12D}$-mutant cells, the selective inhibitor MRTX1133 still reduced HR gene expression and HR repair activity under synchronized conditions (**Fig. S7A–M**). Moreover, in MRTX1133-resistant $KRAS^{G12D}$ lines, where pERK and pAKT remain elevated, MRTX1133 continued to suppress BRCA1, RAD51, and RPA32 and impair HR efficiency (**Fig. 6A–I**).

Together, these data demonstrate that while inhibition of RAS downstream signaling can indirectly suppress HR through cell-cycle regulation, $KRAS^{G12D}$ inhibition exerts an additional, allele-specific, cell-cycle–independent effect. Therefore, ERK/AKT inhibition is sufficient to induce HR suppression in a shared, cell-cycle–dependent manner but is not required for the unique HR repression observed in $KRAS^{G12D}$-mutant cells.

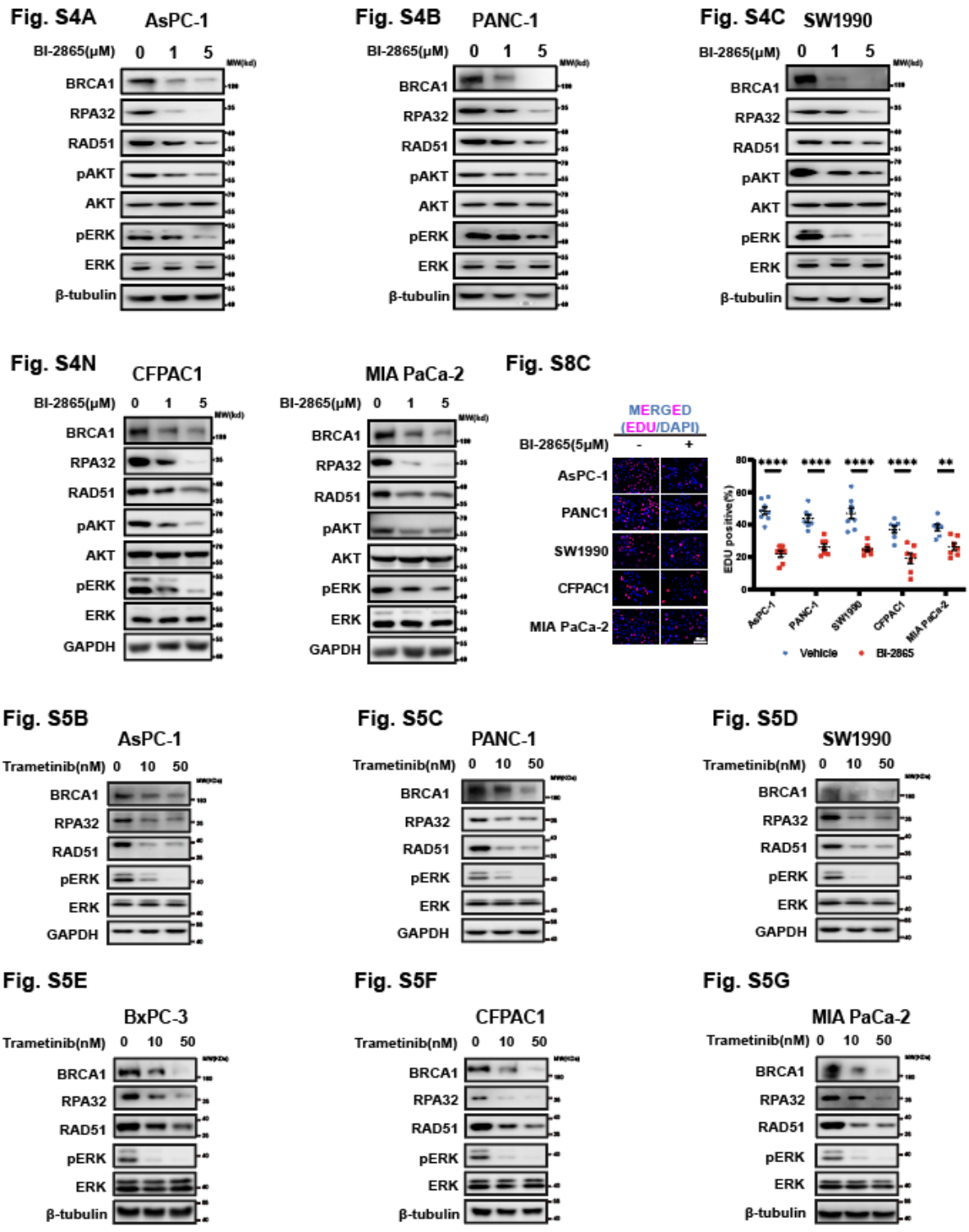

Supplementary Figure 4A-C. Western blot analysis of BRCA1, RPA32, RAD51, total ERK, total AKT, phospho-ERK, and phospho-AKT protein levels in KRASG12D pancreatic cancer cell lines AsPC-1(A), PANC-1(B) and SW1990(C) treated with vehicle (DMSO) or BI-2865 at the indicated concentrations for 24 hours. Cell lysates were collected for immunoblotting. β-Tubulin served as the loading control.

Supplementary Figure 4N. Western blot analysis of BRCA1, RPA32, RAD51, phosphor-ERK and phosphor-AKT in CFPAC1(G12V) and MIA PaCa-2(G12C) cells treated with vehicle (DMSO), BI-2865 at indicated concentrations for 24h. Cell lysate were collected for immunoblotting for BRCA1, RPA32, RAD51, phosphor-ERK and phosphor-AKT. GAPDH served as the loading control.

Supplementary Figure 8C. G1/S phase staining in BI-2865 treated cell lines. Representative images of EdU (5-ethynyl-2'-deoxyuridine) staining for G1/S phase detection in pancreatic cancer cell lines at 24 hours following treatment with 5μM BI-2865. Quantification of EdU-positive cells indicating G1/S phase progression. Data are shown as the mean ± SEM (n > 100 cells per time point from > 5 fields per group). Statistical significance of differences was determined by unpaired Student's t-test (**P<0.01, ****P<0.0001).

Supplementary Figure 5B-G. Western blot analysis of BRCA1, RPA32, RAD51 and phosphor-ERK in pancreatic cell lines treated with vehicle (DMSO), Trametinib at indicated concentrations for 24h. Cell lysate were collected for immunoblotting for BRCA1, RPA32, RAD51 and phosphor-ERK. GAPDH and β-tubulin served as the indicated loading control.

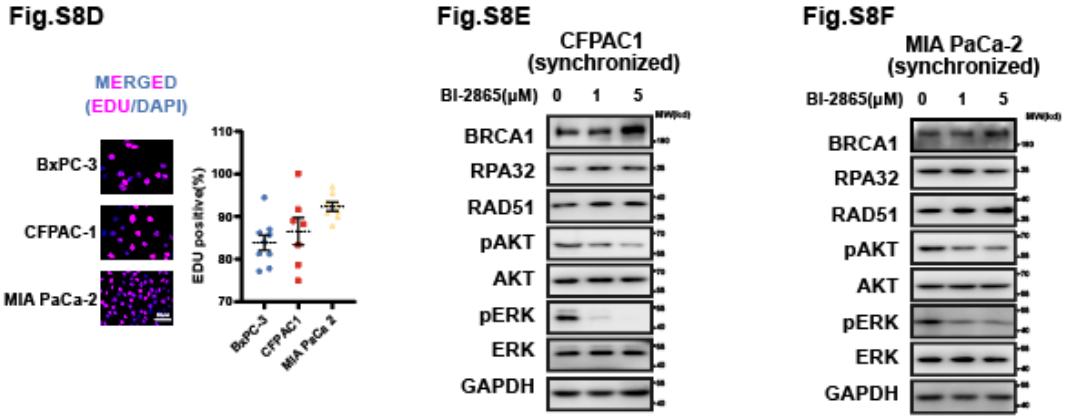

Supplementary Figure 8D. Synchronization efficiency in non-KRAS^{G12D} mutant cells. Representative images of EdU staining in BxPC-3(WT), CFPAC1(G12V) and MIA PaCa-2(G12C) cell lines following synchronization, accompanied by quantification of EdU-positive cell rates using ImageJ software. Data are shown as the mean ± SEM (n > 100 cells per time point from > 5 fields per group).

Supplementary Figure 8E-F. Western blot analysis of BRCA1, RPA32, RAD51, phosphor-AKT and phosphor-ERK in synchronized non-G12D pancreatic cell lines CFPAC1(E) and MIA PaCa-2(F) using HU block and treated with vehicle (DMSO), BI-2865 at indicated concentrations for 24h. Cell lysate were collected for immunoblotting for BRCA1, RPA32, RAD51, phosphor-AKT and phosphor-ERK. GAPDH served as the loading control.

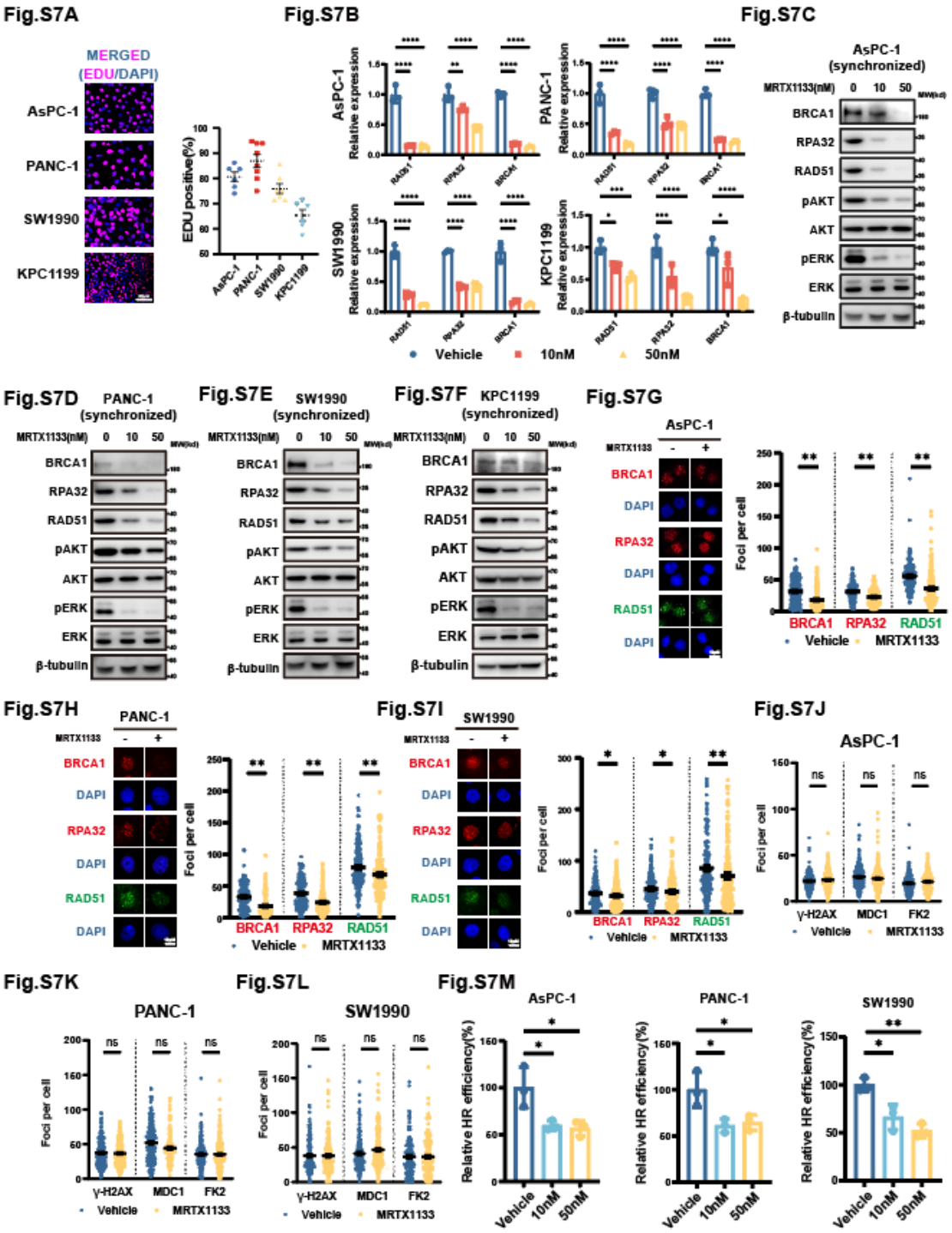

Supplementary Figure 7A. Synchronization efficiency in KRAS^{G12D} mutant cells. Representative images of EdU staining in four KRAS^{G12D} mutant pancreatic cancer cell lines (AsPC-1, PANC-1, SW1990 and KPC1199) following synchronization by hydroxyurea (HU), accompanied by quantification of EdU-positive cell rates using ImageJ software. Data are shown as the mean ± SEM (n > 100 cells per time point from > 5 fields per group).

Supplementary Figure 7B. MRTX1133 downregulated the expression of homologous recombination-related genes in synchronized $KRAS^{G12D}$ mutant cells. Four synchronized pancreatic cancer cell lines (AsPC-1, PANC-1, SW1990, and KPC1199) were treated with vehicle, 10 nM, or 50 nM of MRTX1133 for 24 hours. The relative mRNA expression levels of key homologous recombination (HR) pathway genes, including RAD51, RPA32, and BRCA1, were determined by RT-qPCR. Expression levels were normalized to β-actin and are presented as fold change relative to the vehicle-treated group. Data are shown as mean ± SEM. Statistical significance was determined by one-way ANOVA. (*P<0.05, **P<0.01, ***P<0.001, ****P<0.0001).

Supplementary Figure 7C-F. Western blot analysis of BRCA1, RPA32, RAD51, phospho-ERK, and phospho-AKT protein levels in synchronized AsPC-1 (C), PANC-1 (D), SW1990 (E), and KPC1199 (F) treated with vehicle (DMSO) or MRTX1133 at the indicated concentrations for 24 hours. Cell lysates were collected for immunoblotting. β-Tubulin served as the loading control.

Supplementary Figure 7G-I. Immunofluorescence detection of HR marker foci in synchronized $KRAS^{G12D}$ PDAC cell lines treated with MRTX1133. Assessment of HR marker foci formation in synchronized AsPC-1 (G), PANC-1 (H), and SW1990 (I) cells treated with MRTX1133(50nM) ,at 1 h after 2Gy X-ray irradiation treatment (BRCA1) or at 6 h after 10Gy X-ray irradiation treatment (RPA32 and RAD51). Data were analyzed by the unpaired Student's t-test for significance. Black bars indicate the mean value from ≥ 100 cells. *P<0.05, **P<0.01, ***P<0.001. Mean ± SEM shown. The scale bar indicates 10 μm.

Supplementary Figure 7J-L. Immunofluorescence assay for DNA damage marker in synchronized $KRAS^{G12D}$ PDAC cell lines. Quantification data for γH2AX, MDC1 and FK2 foci formation in the AsPC-1 (J), PANC-1 (K), and SW1990 (L) with and without MRTX1133 treatment (50nM) at 1 h after 2Gy X-ray irradiation treatment (γ-H2AX, MDC1 and FK2). Statistical significance of differences was determined by unpaired Student's t-test (Ns represents no significant). Black bars indicate the mean value from > 100 cells. Mean ± SEM shown.

Supplementary Figure 7M. Inhibition of $KRAS^{G12D}$ effected HR repair efficiency in synchronized pancreatic cancer cells. AsPC-1, PANC-1, and SW1990 were treated with MRTX1133(10nM, 50nM). Efficiency was measured using DR-GFP reporter assay system. Data are shown as the mean ± SEM. Statistical significance of differences compared to vehicle control was determined by unpaired Student's t-test (*P<0.05, **P<0.01).

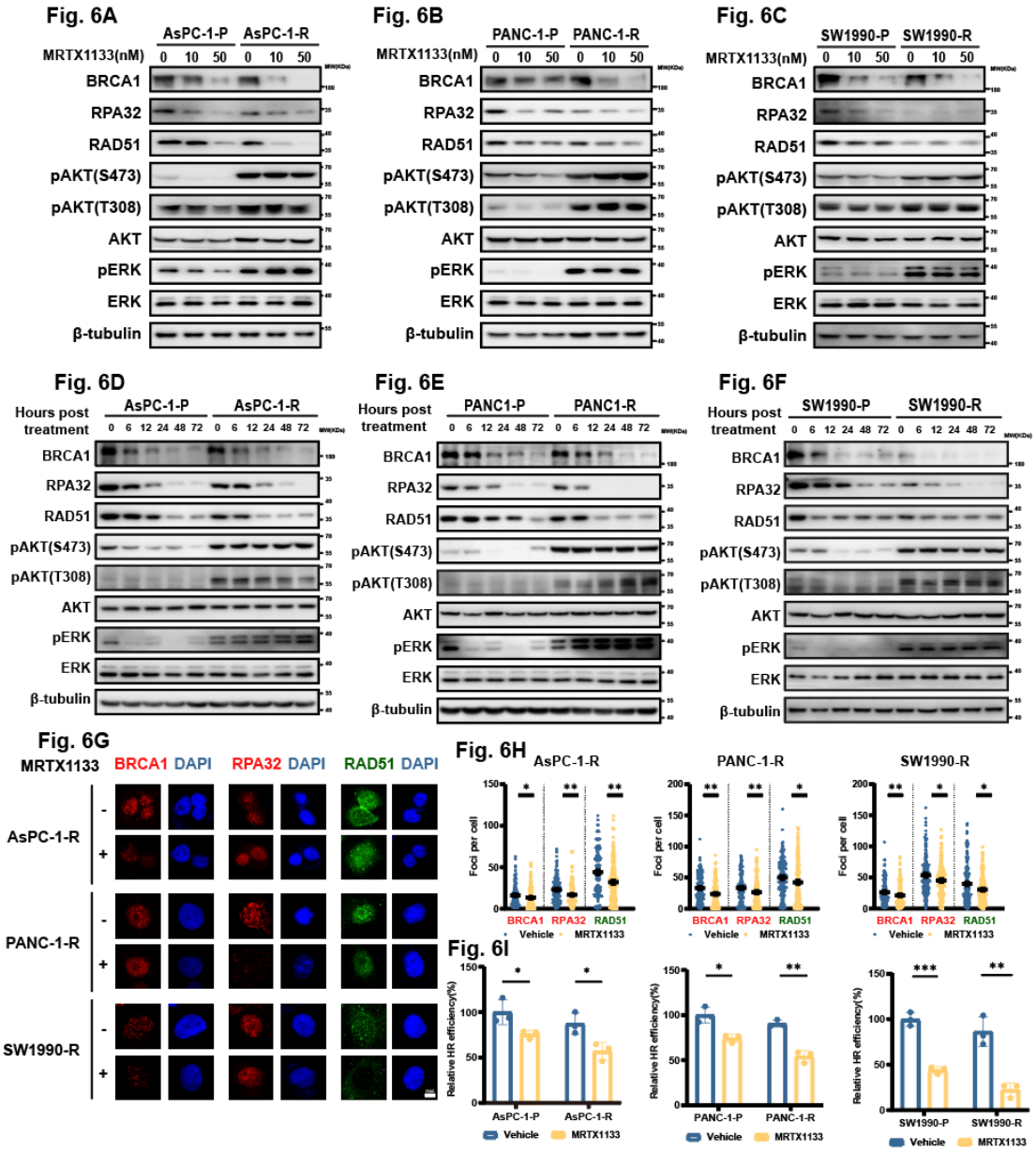

Figure 6A-C. Dose-dependent effects of MRTX1133 on HR and signaling proteins. Parental (P) and MRTX1133-resistant (R) variants of AsPC-1, PANC-1, and SW1990 cells were treated with the indicated concentrations of MRTX1133 for 24 hours. Cell lysates were analyzed by Western blot for BRCA1, RPA32, RAD51, total AKT, total ERK, phospho-AKT (S473, T308), and phospho-ERK. β-Tubulin served as the loading control.

Figure 6D-F. Time-dependent effects of MRTX1133 on HR and signaling proteins. Parental (P) and resistant (R) cells were treated with 50 nM MRTX1133 for the indicated times (6-72 hours). Protein levels were assessed by Western blot as described above.

Figure 6G-H. Immunofluorescence assay for HR-related protein in MRTX1133-

resistant KRASG12D PDAC cell lines. Representative immunofluorescence images (G) and quantification (H) of BRCA1, RPA32, and RAD51 foci in resistant cell lines are shown. For quantification, data from one representative experiment are presented as a scatter plot (n ≥ 100 cells), with black bars indicating the mean. Statistical significance was determined by the unpaired Student's t-test (*P<0.05, **P<0.01). The experiment was repeated three times independently with similar results.

Figure 6I. MRTX1133 treatment reduces HR repair efficiency. Parental and resistant cells were treated with MRTX1133 (50 nM) for 24 hours, and HR efficiency was measured using a DR-GFP reporter assay. Data are shown as mean ± SEM of technical replicates (n=3) from one representative experiment. Statistical significance was determined by the unpaired, two-tailed Student's t-test (*P<0.05, **P<0.01, ***P<0.001). This experiment was also repeated three times with similar results.

COMMENT 4. As the authors discussed that the resistance to KRASG12D inhibitor is a clinical chanllenge, does KRASG12D inhibitor suppress HR repair capacity and HR repair protein expression in KRASG12D inhibitor-resistant cells? Does this combination regimen work for KRASG12D inhibitor-resistant tumors? The models used in the current study are KRASG12D inhibitor-naïve models.

RESPONSE 4: We agree that addressing acquired resistance is critical for clinical translation. To directly test this, we generated MRTX1133-resistant $KRAS^{G12D}$ derivatives from three PDAC cell lines (AsPC-1-R, PANC-1-R, SW1990-R). These resistant cells displayed markedly elevated IC_{50} values for MRTX1133 (**Fig. S12A–C**) but retained similar baseline sensitivity to olaparib compared with parental lines (**Fig. S12D–F**).

1) $KRAS^{G12D}$ inhibition still suppresses HR in resistant cells.

Despite persistent activation of downstream signaling (pERK/pAKT), MRTX1133 re-treatment in resistant cells caused dose- and time-dependent decreases in BRCA1, RAD51, and RPA32 (**Fig. 6A–F**), reduced HR foci formation (**Fig. 6G–H; S12G-J**), and impaired DR-GFP HR efficiency (**Fig. 6I**). These findings demonstrate that $KRAS^{G12D}$ inhibition continues to suppress HR repair capacity even in the resistant state, through a mechanism decoupled from canonical MAPK/PI3K signaling.

2) KRAS^{G12D} + PARP inhibition remains effective in resistant models *in vitro* and *in vivo*.

In all three resistant lines, MRTX1133 + olaparib produced strong synergy (Bliss > 15; HSA/ZIP/Loewe > 5) (**Fig. 6J–L; S12K**). Consistently, in xenografts derived from SW1990-R and PANC-1-R, MRTX1133 alone had minimal effect, whereas the combination regimen achieved the greatest tumor growth inhibition (**Fig. 7A–F**). Histological analyses showed reduced RAD51, increased γH2AX, and elevated cleaved caspase-3 (**Fig. 7G–P**), confirming enhanced DNA damage and apoptosis in resistant tumors.

Thus, KRAS^{G12D} inhibition maintains HR suppression and PARPi synergy in resistant settings, and the MRTX1133 + olaparib combination remains therapeutically effective both *in vitro* and in resistant tumor models *in vivo*. These results underscore the durability and translational potential of this strategy beyond inhibitor-naïve contexts.

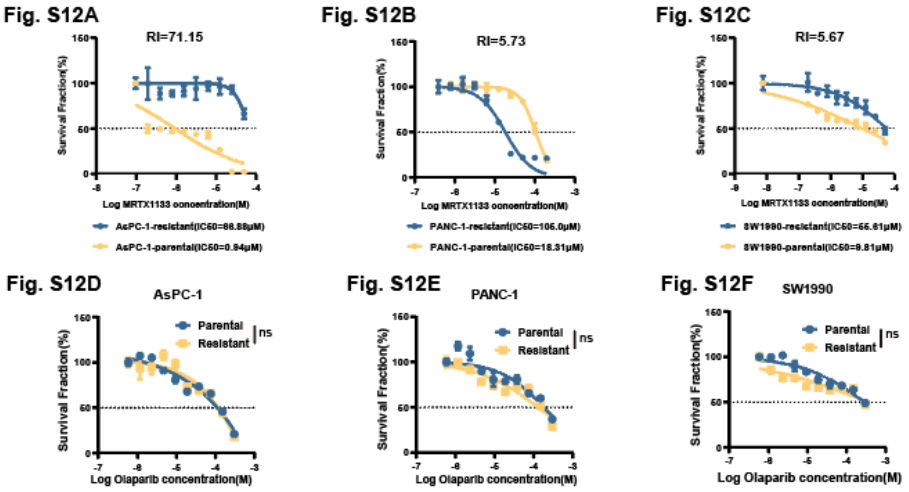

Supplementary Figure 12A-C. Establishment and validation of MRTX1133-resistant cell lines. Dose-response curves show the increased IC50 values for MRTX1133 in resistant (-R) versus parental cell lines for AsPC-1 (A), PANC-1 (B), and SW1990 (C). The Resistance Index (RI) is the ratio of IC50 values (resistant/parental).

Supplementary Figure 12D-F. MRTX1133-resistant cells do not exhibit cross-resistance to Olaparib. Dose-response curves for Olaparib in parental versus resistant AsPC-1 (D), PANC-1 (E), and SW1990 (F) cells show no significant difference in sensitivity after 72 hours of treatment. Data are presented as mean ± SEM, and statistical significance between curves was assessed by two-way ANOVA. Ns indicates no significant difference between parental and resistant cells.

.

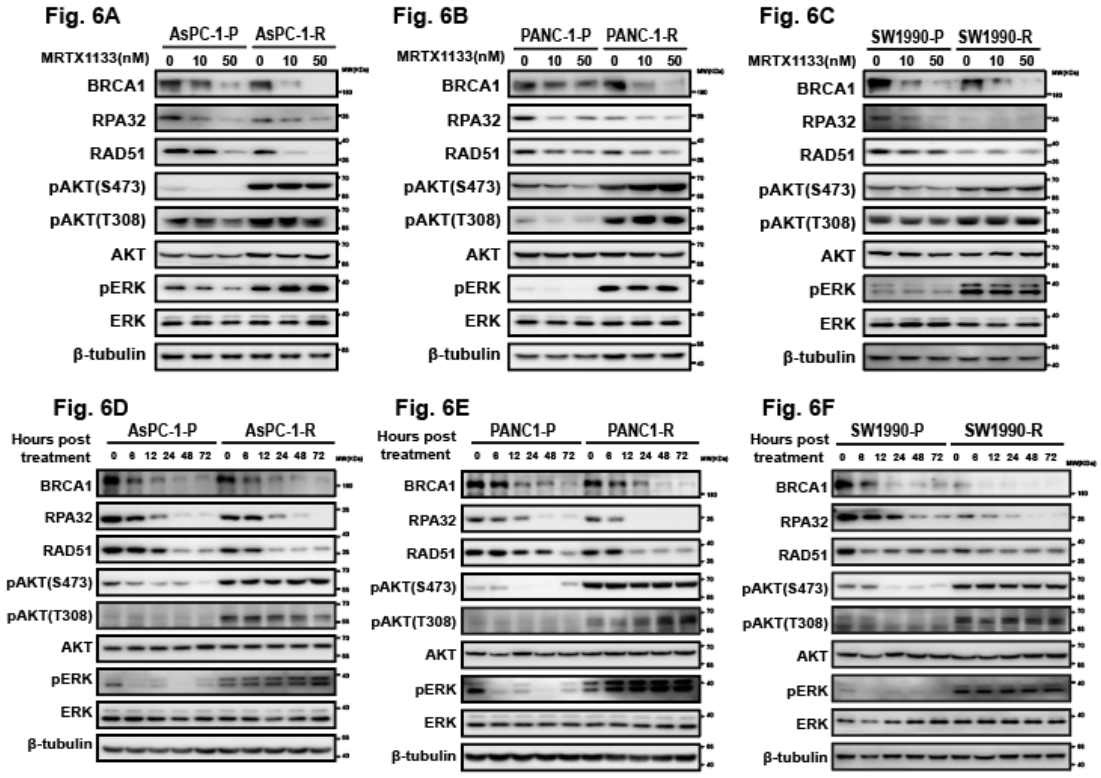

Figure 6A-C. Dose-dependent effects of MRTX1133 on HR and signaling proteins. Parental (P) and MRTX1133-resistant (R) variants of AsPC-1, PANC-1, and SW1990 cells were treated with the indicated concentrations of MRTX1133 for 24 hours. Cell lysates were analyzed by Western blot for BRCA1, RPA32, RAD51, total AKT, total ERK, phospho-AKT (S473, T308), and phospho-ERK. β-Tubulin served as the loading control.

Figure 6D-F. Time-dependent effects of MRTX1133 on HR and signaling proteins. Parental (P) and resistant (R) cells were treated with 50 nM MRTX1133 for the indicated times (6-72 hours). Protein levels were assessed by Western blot as described above.

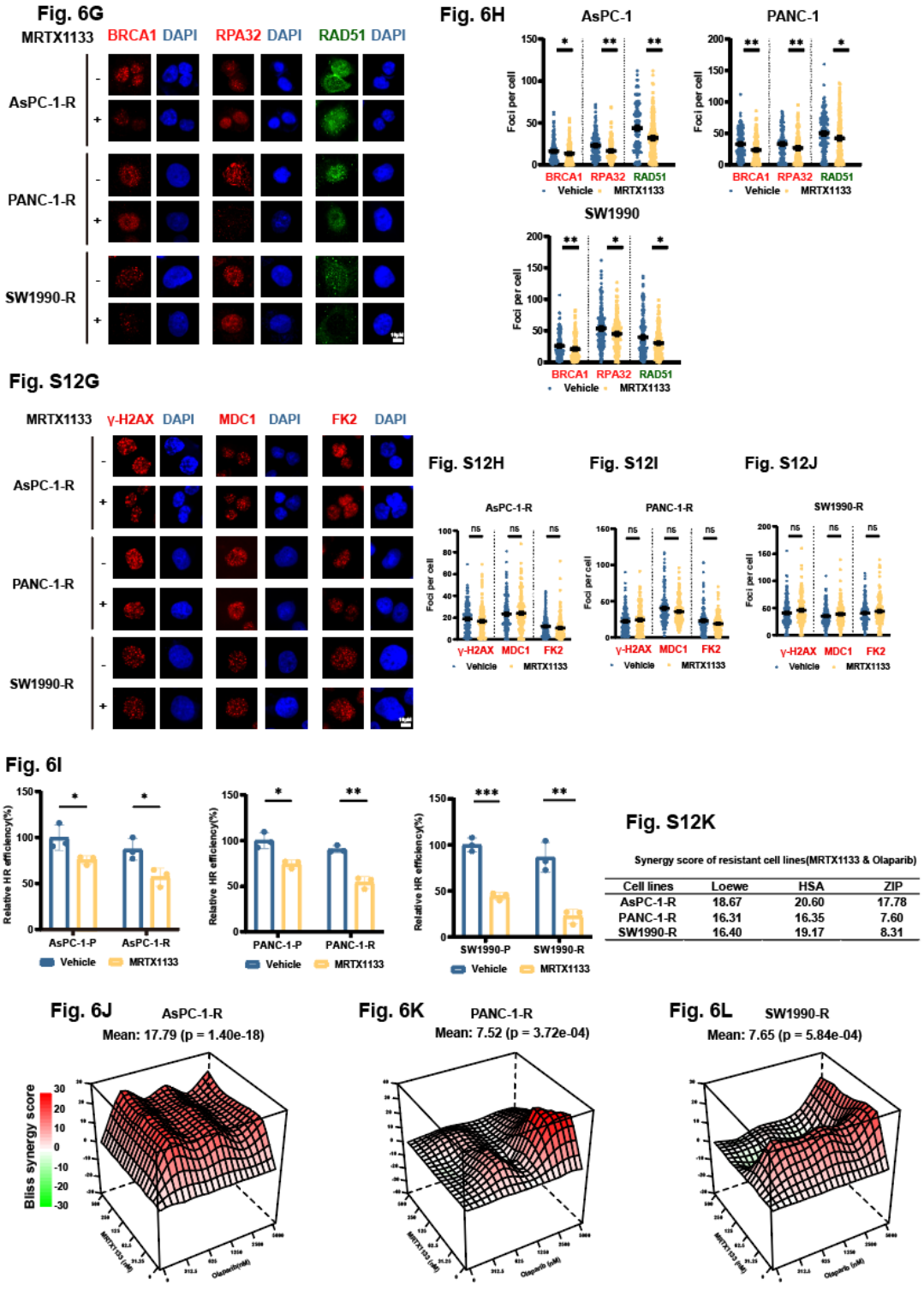

Figure 6G-H. Immunofluorescence assay for HR-related protein in MRTX1133-resistant KRASG12D PDAC cell lines. Representative immunofluorescence images (G) and quantification (H) of BRCA1, RPA32, and RAD51 foci in resistant cell lines are shown. For quantification, data from one representative experiment are presented as a scatter plot (n ≥ 100 cells), with black bars indicating the mean. Statistical significance

was determined by the unpaired Student's t-test (*P<0.05, **P<0.01). The experiment was repeated three times independently with similar results.

Supplementary Figure 12G-J. Immunofluorescence assay for DNA damage marker in MRTX1133-resistant $KRAS^{G12D}$ PDAC cell lines. Representative micrographs (G) and quantification data for γ-H2AX, MDC1 and FK2 in AsPC-1-R (H), PANC-1-R (I), and SW1990-R (J) cell lines following MRTX1133 treatment(50nM). Statistical significance was determined by unpaired, two-tailed Student's t-test. Ns represents no significant.

Figure 6I. MRTX1133 treatment reduces HR repair efficiency. Parental and resistant cells were treated with MRTX1133 (50 nM) for 24 hours, and HR efficiency was measured using a DR-GFP reporter assay. Data are shown as mean ± SEM of technical replicates (n=3) from one representative experiment. Statistical significance was determined by the unpaired, two-tailed Student's t-test (*P<0.05, **P<0.01, ***P<0.001). This experiment was also repeated three times with similar results.

Figure 6J-L. Synergistic anti-tumor effect of MRTX1133 combined with Olaparib in resistant pancreatic cancer cells. Three-dimensional synergy plots show the interaction between MRTX1133 and Olaparib in AsPC-1-R (J), PANC-1-R (K), and SW1990-R (L) cells after 144 hours of treatment. Red peaks indicate synergy, and green valleys indicate antagonism. The overall mean synergy score and p-value for each combination are shown in the title of each plot.

Supplementary Figure 12K. Synergy score of Olaparib combined with MTRX1133 in resistant cell lines. Synergy score was analyzed using HSA, Loewe and ZIP models and listed in the table.

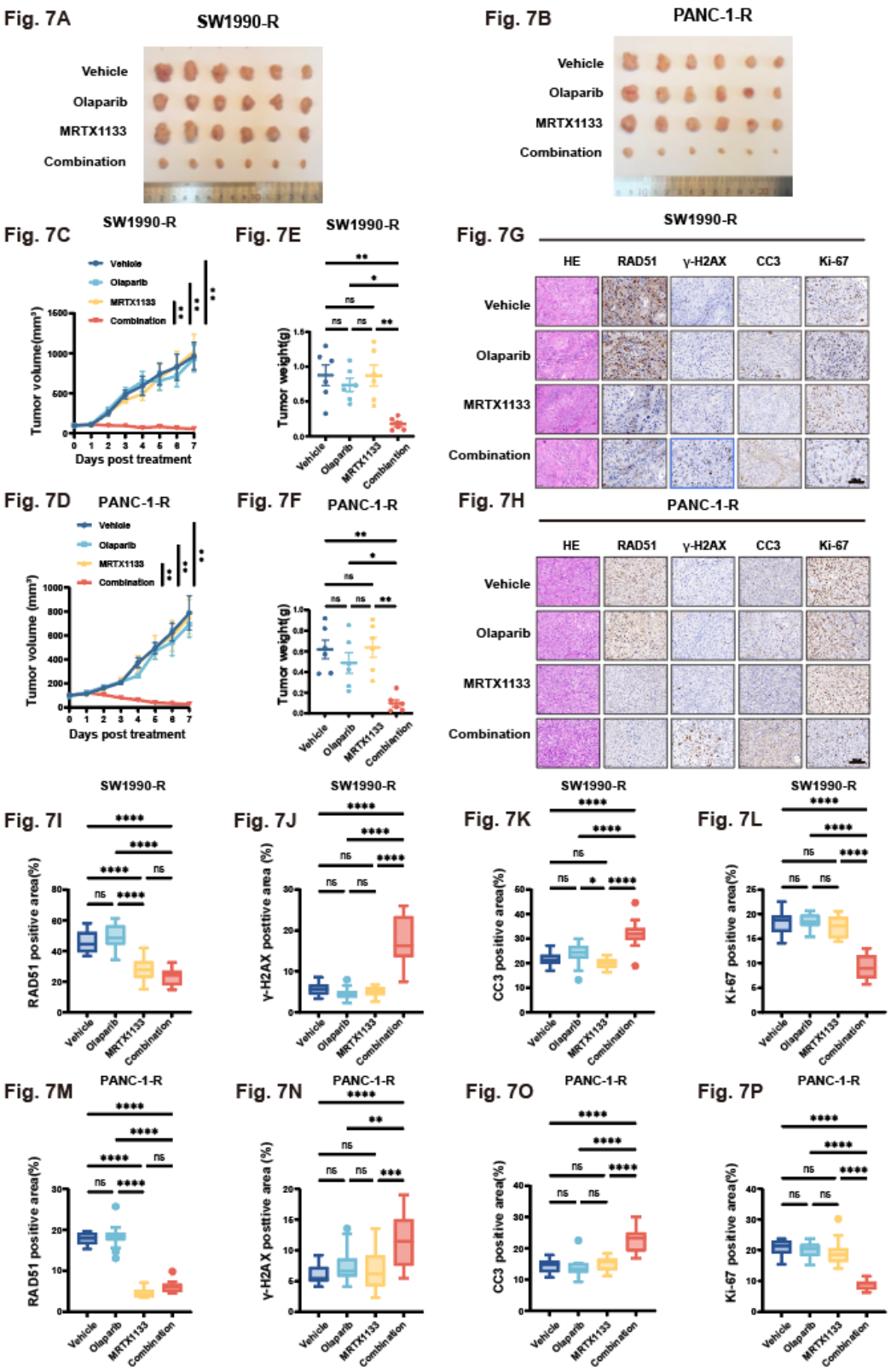

Figure 7A. Represent image of tumors of SW1990-R cell derived xenograft.

Figure 7B. Represent image of tumors of PANC-1-R cell derived xenograft.

Figure 7C-F. Tumor volume (C-D) and weight (E-F) of mice bearing SW1990-R cells (C, E) and PANC-1-R cells (D, F). When tumors reached approximately 80-120 mm^3, treatment was initiated (defined as Day 0). Mice (n=6 per group) were treated daily with vehicle, MRTX1133 (30 mg/kg), olaparib (50 mg/kg), or the combination. Statistical significance was determined by Two-way ANOVA for (C, D), one-way ANOVA for (E-F). Ns, no significant. *P<0.05, **P<0.01. Mean ± SEM shown.

Figure 7G-H. Tumor tissues from SW1990-R and PANC-1-R xenografts were subjected to HE and IHC analyses and probed with indicated antibodies. Representative images(20× magnification) of IHC are shown with treatment indicated. The scale bar indicates 50 μm. CC3: cleaved-caspase 3.

Figure 7I-P. Quantification of indicated markers shown in (G-H). Data are presented as box-and-whisker plots. For quantification, tissues from 3 mice per group were analyzed, with 5 randomly selected high-power fields quantified per tumor. Statistical significance was determined by one-way ANOVA. Ns, no significant. *P<0.05, **P<0.01, ***P<0.001, ****P<0.0001.

Reviewer #3 (Remarks to the Author):

In this manuscript, Xu and colleagues investigate the specific effect of KRAS G12D inhibition with MRTX1133 to induce homologous repair (HR) deficiency in pancreatic cancer cells, which could be exploited therapeutically by combining KRAS inhibition with PARP inhibitors. The authors used both human and mouse pancreatic cancer cell lines harboring the KRAS G12D mutation to show that effective inhibition of the MAPK pathway induces downregulation of HR genes, including RAD51, and impairs the cellular response to double-strand breaks induced through irradiation. Notably, inhibition of the pathway per se does not increase DNA damage but rather reduces the efficiency of repairing induced damage.

The specificity of this induced phenotype is addressed by showing that the downregulation of HR genes does not occur in KRAS wild-type cells (e.g., BXPC-3) treated with MRTX1133 nor in pancreatic cancer cells harboring other KRAS mutations (e.g., G12V) treated with a pan-Ras inhibitor. Importantly, the treatment-induced phenotype is not solely attributable to a reduced cell proliferation index. The authors further demonstrate synergistic effects between MRTX1133 and the PARP inhibitor Olaparib in both in vitro and in vivo settings.

This is a timely and interesting manuscript given the interest around KRAS inhibition in pancreatic cancer. Previous studies have shown that KRAS inhibitors, including MRTX1133, often have transient efficacy with resistance mechanisms—both genetic and non-genetic—emerging rapidly. Additionally, rapid pathway rewiring following treatment necessitates close monitoring of pathway dynamics to interpret findings robustly. I think the last two aspects are a bit overlooked in this manuscript.

While the findings in this manuscript are potentially impactful, the study lacks rigor in conducting and reporting experiments, with significant gaps in statistical

analysis and experimental controls.

RESPONSE: We sincerely thank the reviewer for the thoughtful and constructive comments. We appreciate the recognition of the novelty and potential impact of our study and fully agree that pathway rewiring and resistance mechanisms are critical for understanding the long-term consequences of KRAS inhibition. In the revised manuscript, we have incorporated additional time-course and resistant-model analyses to address these important aspects and have strengthened statistical presentation and experimental details throughout. Specific revisions and supporting data are provided in the point-by-point responses below.

One important point that needs clarification is the specificity of HR deficiency induction. The question here is whether the treatment of G12D cells with pan-Ras inhibitors would result in the same phenotype, i.e. HR deficiency. In my opinion, the following experiments should be conducted:

COMMENT.(i) Evaluate the effect of pan-RAS inhibitors on KRAS G12D-driven cancer cells, as the authors have access to this drug;

RESPONSE I #: We thank the reviewer for this thoughtful suggestion. We performed additional experiments using the pan-RAS inhibitor BI-2865 in $KRAS^{G12D}$-mutant PDAC cell lines (AsPC-1, PANC-1, SW1990). Treatment with BI-2865 (1–5 μM, 24–48 h) achieved >80% inhibition of pERK and pAKT (**Fig. S4A–C**), confirming robust target engagement. Under these optimized conditions, BI-2865 markedly reduced BRCA1, RAD51, and RPA32 protein levels, decreased HR-foci formation after ionizing radiation, and significantly impaired HR repair efficiency as measured by the

DR-GFP assay (**Fig. S4G-M**). These results demonstrate that pan-RAS inhibition is sufficient to induce HR deficiency in $KRAS^{G12D}$-mutant cells, primarily through suppression of downstream MAPK/PI3K signaling and associated S-phase reduction. However, when the cell cycle was synchronized, only the $KRAS^{G12D}$-selective inhibitor MRTX1133 continued to suppress HR gene expression (**Fig. S7A–M**), whereas BI-2865 no longer had this effect in non-G12D lines (**Fig. S8D-F**). This indicates that $KRAS^{G12D}$ inhibition uniquely triggers a cell-cycle–independent mechanism of HR repression, distinguishing it mechanistically from pan-RAS inhibition and reinforcing the allele-specific nature of the response.

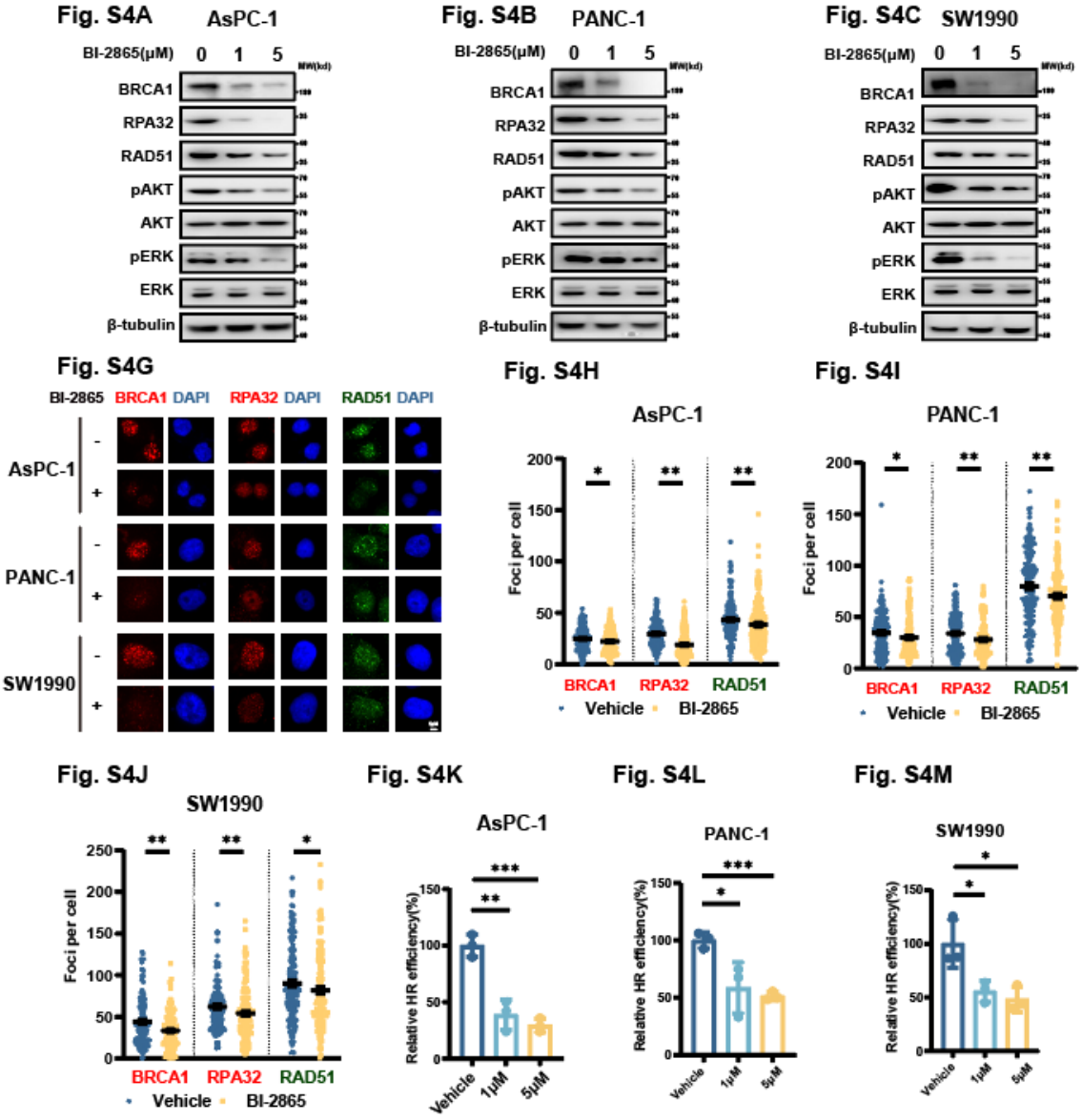

Supplementary Figure 4A-C. Western blot analysis of BRCA1, RPA32, RAD51, total ERK, total AKT, phospho-ERK, and phospho-AKT protein levels in KRASG12D pancreatic cancer cell lines AsPC-1(A), PANC-1(B) and SW1990(C) treated with vehicle (DMSO) or BI-2865 at the indicated concentrations for 24 hours. Cell lysates were collected for immunoblotting. β-Tubulin served as the loading control.

Supplementary Figure 4G-J. Immunofluorescence detection of HR marker foci in $KRAS^{G12D}$ pancreatic cancer cells treated with BI-2865. Representative micrographs (G) and quantification data for BRCA1, RPA32 and RAD51 foci formation (H-J) in the indicated cell lines with and without BI-2865 treatment (5μM), at 1 h after 2Gy X-ray irradiation treatment (BRCA1), at 6 h after 2Gy X-ray irradiation treatment (RPA32 and RAD51). Statistical significance of differences was determined by unpaired Student's t-test (*P<0.05, **P<0.01). Black bars indicate the mean from > 100 cells. Mean ± SEM shown. The scale bar indicates 10 μm.

Supplementary Figure 4K-M. Inhibition of $KRAS^{G12D}$ by BI-2865 decreased HR repair efficiency in $KRAS^{G12D}$ pancreatic cancer cells. AsPC-1(K), PANC-1(L), and SW1990(M) were treated with BI-2865(1μM，5μM). Efficiency was measured using DR-GFP reporter assay system. Data are shown as the mean ± SEM. Statistical significance of differences compared to vehicle control was determined by unpaired Student's t-test (*P<0.05, **P<0.01, ***P<0.001).

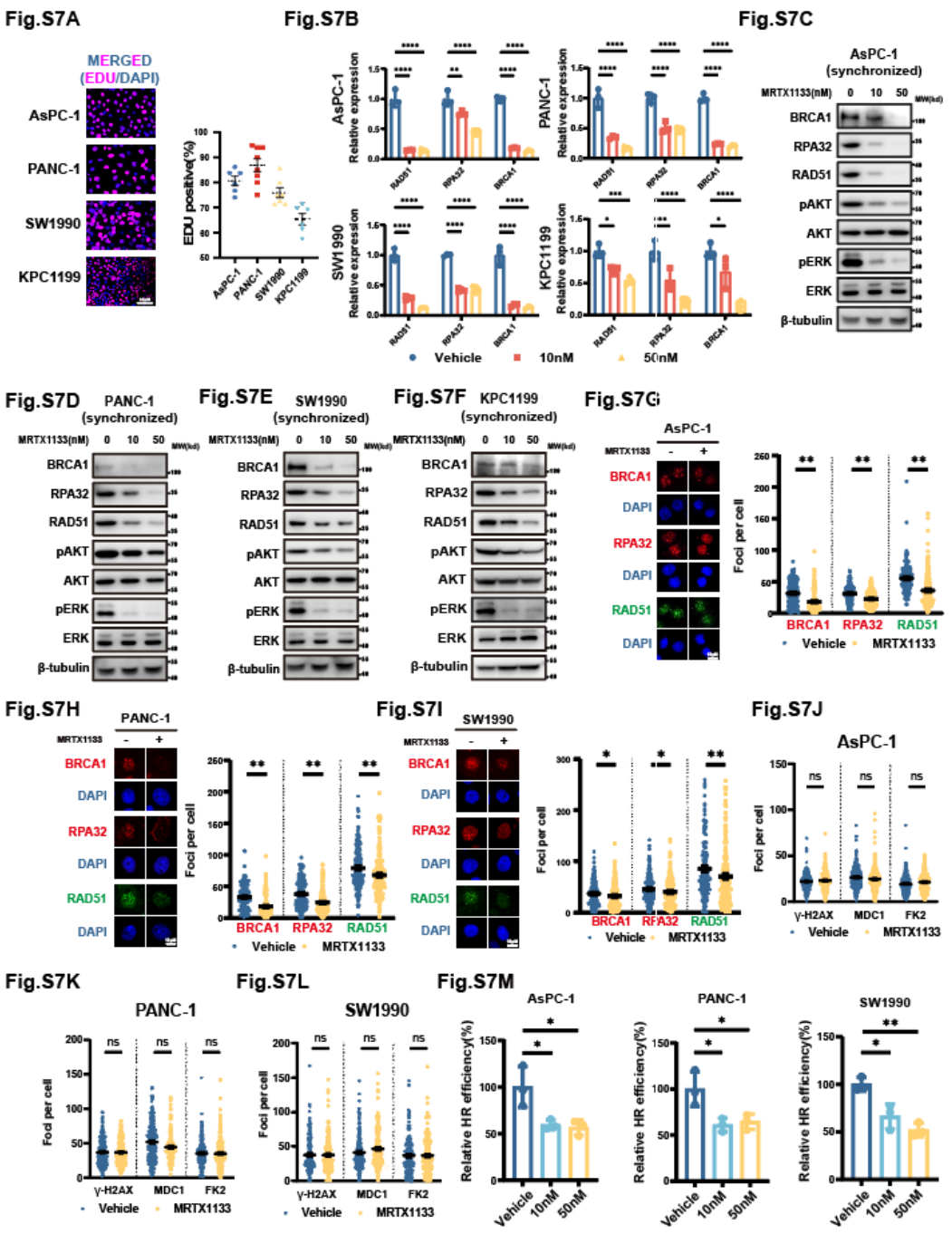

Supplementary Figure 7A. Synchronization efficiency in KRAS^{G12D} mutant cells. Representative images of EdU staining in four KRAS^{G12D} mutant pancreatic cancer cell lines (AsPC-1, PANC-1, SW1990 and KPC1199) following synchronization by hydroxyurea (HU), accompanied by quantification of EdU-positive cell rates using ImageJ software. Data are shown as the mean ± SEM (n > 100 cells per time point from > 5 fields per group).

Supplementary Figure 7B. MRTX1133 downregulated the expression of homologous recombination-related genes in synchronized $KRAS^{G12D}$ mutant cells. Four synchronized pancreatic cancer cell lines (AsPC-1, PANC-1, SW1990, and KPC1199) were treated with vehicle, 10 nM, or 50 nM of MRTX1133 for 24 hours. The relative mRNA expression levels of key homologous recombination (HR) pathway genes, including RAD51, RPA32, and BRCA1, were determined by RT-qPCR. Expression levels were normalized to β-actin and are presented as fold change relative to the vehicle-treated group. Data are shown as mean ± SEM. Statistical significance was determined by one-way ANOVA. (*P<0.05, **P<0.01, ***P<0.001, ****P<0.0001).

Supplementary Figure 7C-F. Western blot analysis of BRCA1, RPA32, RAD51, phospho-ERK, and phospho-AKT protein levels in synchronized AsPC-1 (C), PANC-1 (D), SW1990 (E), and KPC1199 (F) treated with vehicle (DMSO) or MRTX1133 at the indicated concentrations for 24 hours. Cell lysates were collected for immunoblotting. β-Tubulin served as the loading control.

Supplementary Figure 7G-I. Immunofluorescence detection of HR marker foci in synchronized $KRAS^{G12D}$ PDAC cell lines treated with MRTX1133. Assessment of HR marker foci formation in synchronized AsPC-1 (G), PANC-1 (H), and SW1990 (I) cells treated with MRTX1133(50nM) ,at 1 h after 2Gy X-ray irradiation treatment (BRCA1) or at 6 h after 10Gy X-ray irradiation treatment (RPA32 and RAD51). Data were analyzed by the unpaired Student's t-test for significance. Black bars indicate the mean value from ≥ 100 cells. *P<0.05, **P<0.01, ***P<0.001. Mean ± SEM shown. The scale bar indicates 10 μm.

Supplementary Figure 7J-L. Immunofluorescence assay for DNA damage marker in synchronized $KRAS^{G12D}$ PDAC cell lines. Quantification data for γH2AX, MDC1 and FK2 foci formation in the AsPC-1 (J), PANC-1 (K), and SW1990 (L) with and without MRTX1133 treatment (50nM) at 1 h after 2Gy X-ray irradiation treatment (γ-H2AX, MDC1 and FK2). Statistical significance of differences was determined by unpaired Student's t-test (Ns represents no significant). Black bars indicate the mean value from > 100 cells. Mean ± SEM shown.

Supplementary Figure 7M. Inhibition of $KRAS^{G12D}$ effected HR repair efficiency in synchronized pancreatic cancer cells. AsPC-1, PANC-1, and SW1990 were treated with MRTX1133(10nM, 50nM). Efficiency was measured using DR-GFP reporter assay system. Data are shown as the mean ± SEM. Statistical significance of differences compared to vehicle control was determined by unpaired Student's t-test (*P<0.05, **P<0.01).

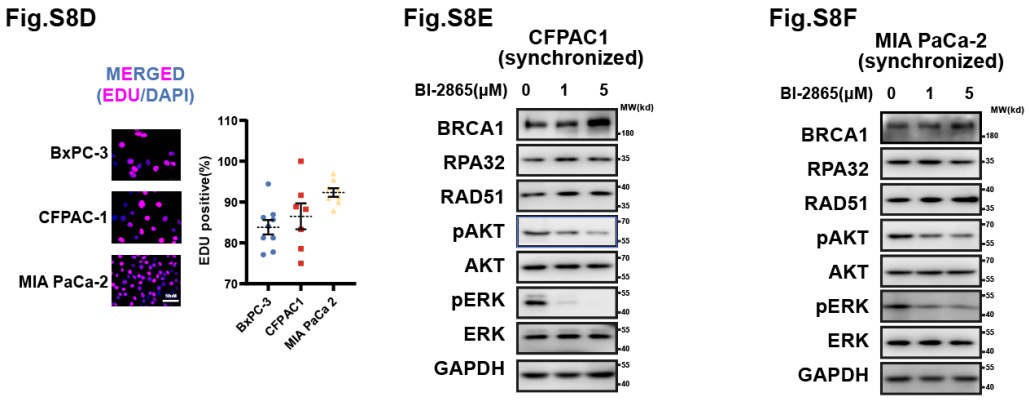

Supplementary Figure 8D. Synchronization efficiency in non-KRAS^{G12D} mutant cells. Representative images of EdU staining in BxPC-3(WT), CFPAC1(G12V) and MIA PaCa-2(G12C) cell lines following synchronization, accompanied by quantification of EdU-positive cell rates using ImageJ software. Data are shown as the mean ± SEM (n > 100 cells per time point from > 5 fields per group).

Supplementary Figure 8E-F. Western blot analysis of BRCA1, RPA32, RAD51, phosphor-AKT and phosphor-ERK in synchronized non-G12D pancreatic cell lines CFPAC1(E) and MIA PaCa-2(F) using HU block and treated with vehicle (DMSO), BI-2865 at indicated concentrations for 24h. Cell lysate were collected for immunoblotting for BRCA1, RPA32, RAD51, phosphor-AKT and phosphor-ERK. GAPDH served as the loading control.

COMMENT. (ii) test another MAPK pathway inhibitor (trametinib) in KRAS G12D-mutant and non-G12D-mutant tumor cells.

RESPONSE ii#: We thank the reviewer for this insightful suggestion. We addressed this point by evaluating the MEK inhibitor trametinib, which specifically targets the MAPK cascade downstream of KRAS, in both $KRAS^{G12D}$-mutant (AsPC-1, PANC-1, SW1990) and non-G12D-mutant (BxPC-3 [WT], CFPAC-1 [G12V], MIA PaCa-2 [G12C]) pancreatic cancer cell lines. Cells were treated with trametinib (0–50 nM, 24 h), and pERK1/2, BRCA1, RAD51, and RPA32 were analyzed by western blot (**Fig. S5B–G**). Trametinib treatment led to a dose-dependent decrease in pERK across all genotypes, accompanied by concomitant downregulation of HR-related proteins regardless of KRAS allele status. These findings confirm that MAPK pathway suppression alone can downregulate HR gene expression through a shared, cell-cycle–dependent mechanism, consistent with the pan-RAS inhibitor results. However, unlike $KRAS^{G12D}$-specific inhibition (MRTX1133), trametinib did not induce HR suppression under synchronized conditions (**Fig. S8G-L**), highlighting that $KRAS^{G12D}$ blockade engages an additional, cell-cycle–independent mechanism distinct from generalized MAPK inhibition. These results have been incorporated into the revised manuscript (**Supplementary Fig. S5 and S8**) and discussed as supportive evidence for the dual-arm model of KRAS-mediated HR regulation.

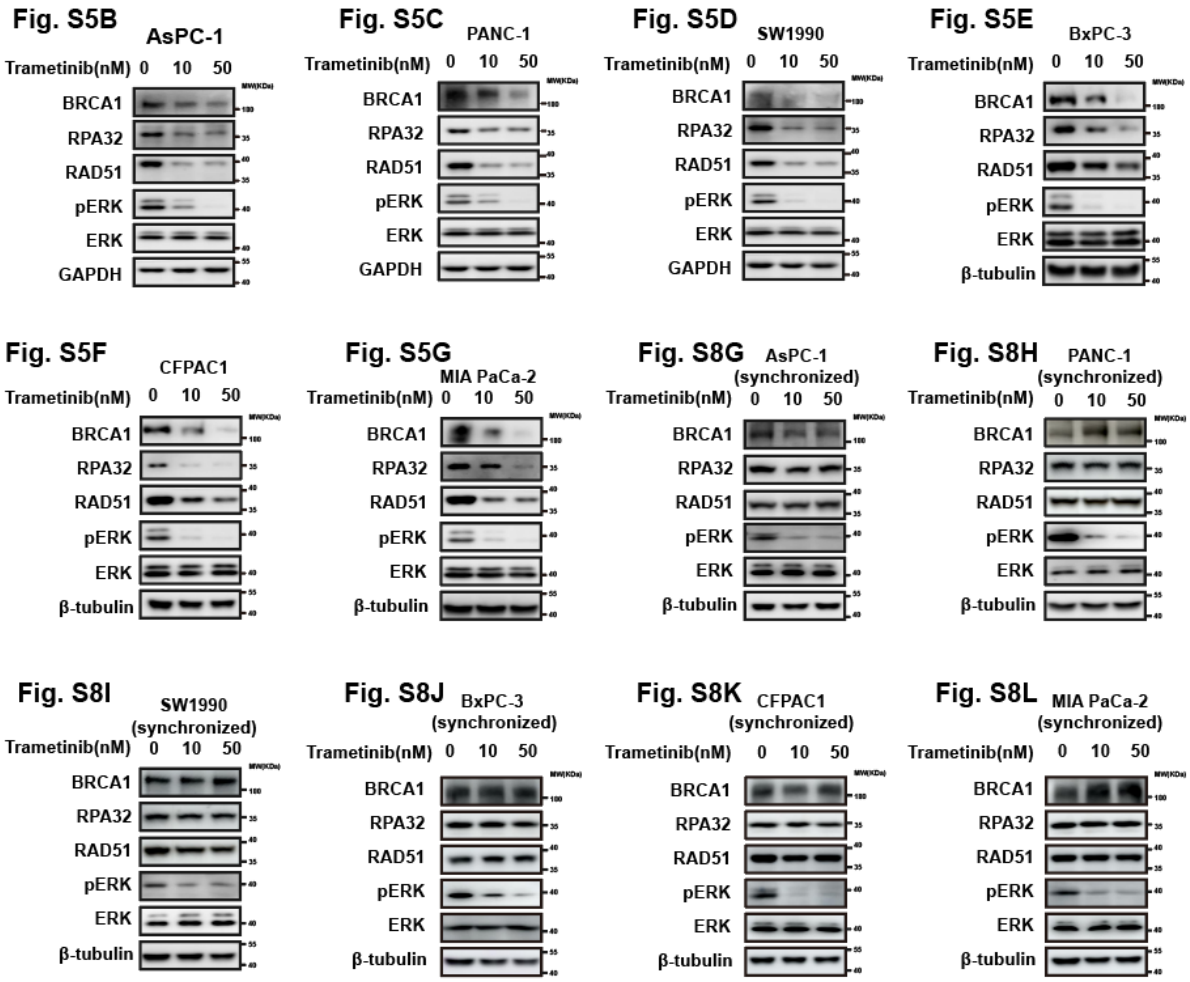

Supplementary Figure 5B-G. Western blot analysis of HR proteins and ERK signaling in pancreatic cell lines treated with vehicle (DMSO), Trametinib at indicated concentrations for 24h. Cell lysate were collected for immunoblotting for BRCA1, RPA32, RAD51 and phosphor-ERK. GAPDH and β-tubulin served as the indicated loading control.

Supplementary Figure 8G-L. Western blot analysis of HR proteins and ERK signaling in synchronized pancreatic cell lines treated with vehicle (DMSO), Trametinib at indicated concentrations for 24h. Cell lysate were collected for immunoblotting for BRCA1, RPA32, RAD51 and phosphor-ERK. β-tubulin served as the indicated loading control.

COMMENT.(iii) Perform genetic perturbation (e.g., KRAS G12D knockdown/knockout) to determine if the HR-deficient phenotype is allele-specific or drug-specific. Furthermore, I think that the HRD phenotype needs a more rigorous validation by, among other things, use a validated HRD score to quantitatively assess homologous repair deficiency across cell lines. The authors might consider using the COMET assays to measure DSB formation accurately and correlate results with HR efficiency and test synthetic lethality by targeting RAD51 or BRCA1/2 genetically in combination with KRAS inhibition.

RESPONSE III#: We thank the reviewer for these excellent suggestions, which guided us to perform additional genetic and functional validation experiments to confirm that the HR-deficient phenotype is allele-specific and not drug-dependent, and to quantitatively substantiate the HRD phenotype.

To determine allele specificity, we performed KRAS knockdown using shRNA in $KRAS^{G12D}$-mutant cell lines (AsPC-1, PANC-1, SW1990). KRAS depletion significantly reduced HR-foci formation (BRCA1, RAD51, RPA32) without affecting early DNA damage sensors (γ-H2AX, MDC1, FK2) (**Fig. S3C–H**). DR-GFP assays further confirmed a substantial loss of HR repair efficiency following KRAS knockdown (**Fig. S3I–K**), reproducing the pharmacologic effects of MRTX1133, thereby confirming that the HRD phenotype is allele-specific rather than drug-specific.

For quantitative HRD validation, we calculated validated HRD scores (LOH: loss of heterozygosity; TAI: telomeric allelic imbalance; LST: large-scale state transitions) using whole-genome sequencing data. KRAS knockdown increased HRD scores in all three cell lines: AsPC-1 (LOH: 5 to 6; TAI: 11 to 13; LST: 7 to 11); PANC-1 (LOH: 3 to 9; TAI: 10 to 14; LST: 10 to 16); SW1990 (LOH: 5 to 9; TAI: 6 to 14; LST: 10 to 15) (**Fig. S3L-N**). As a positive control, shBRCA1 in PANC-1 cells markedly elevated scores (LOH: 3 to 17; TAI: 10 to 12; LST: 10 to 10; **Fig. S3O**), confirming assay sensitivity.

To further corroborate these findings, we conducted COMET assays to measure DNA double-strand break (DSB) formation following irradiation. KRAS knockdown cells displayed markedly increased tail DNA percentage, confirming impaired DSB repair capacity (**Fig. S3A–B**). Moreover, given that $KRAS^{G12D}$ inhibition transcriptionally downregulates BRCA1 and RAD51, we used BRCA1 knockdown as a genetic benchmark. As shown in **Supplementary Figure 9K**, BRCA1 depletion in AsPC-1, PANC-1, and SW1990 phenocopied the effects of $KRAS^{G12D}$ inhibition and resulted in increased PARP inhibitor sensitivity, validating that HR loss underlies the observed synthetic lethality with PARP inhibition.

Together, these experiments demonstrate that $KRAS^{G12D}$ depletion induces HR deficiency through transcriptional downregulation of BRCA1/RAD51, and that this HRD state directly mediates synthetic lethality with PARP inhibition. These findings confirm that the HRD phenotype is allele-specific, genetically reproducible, and quantitatively validated, thus strengthening the mechanistic and translational significance of our study.

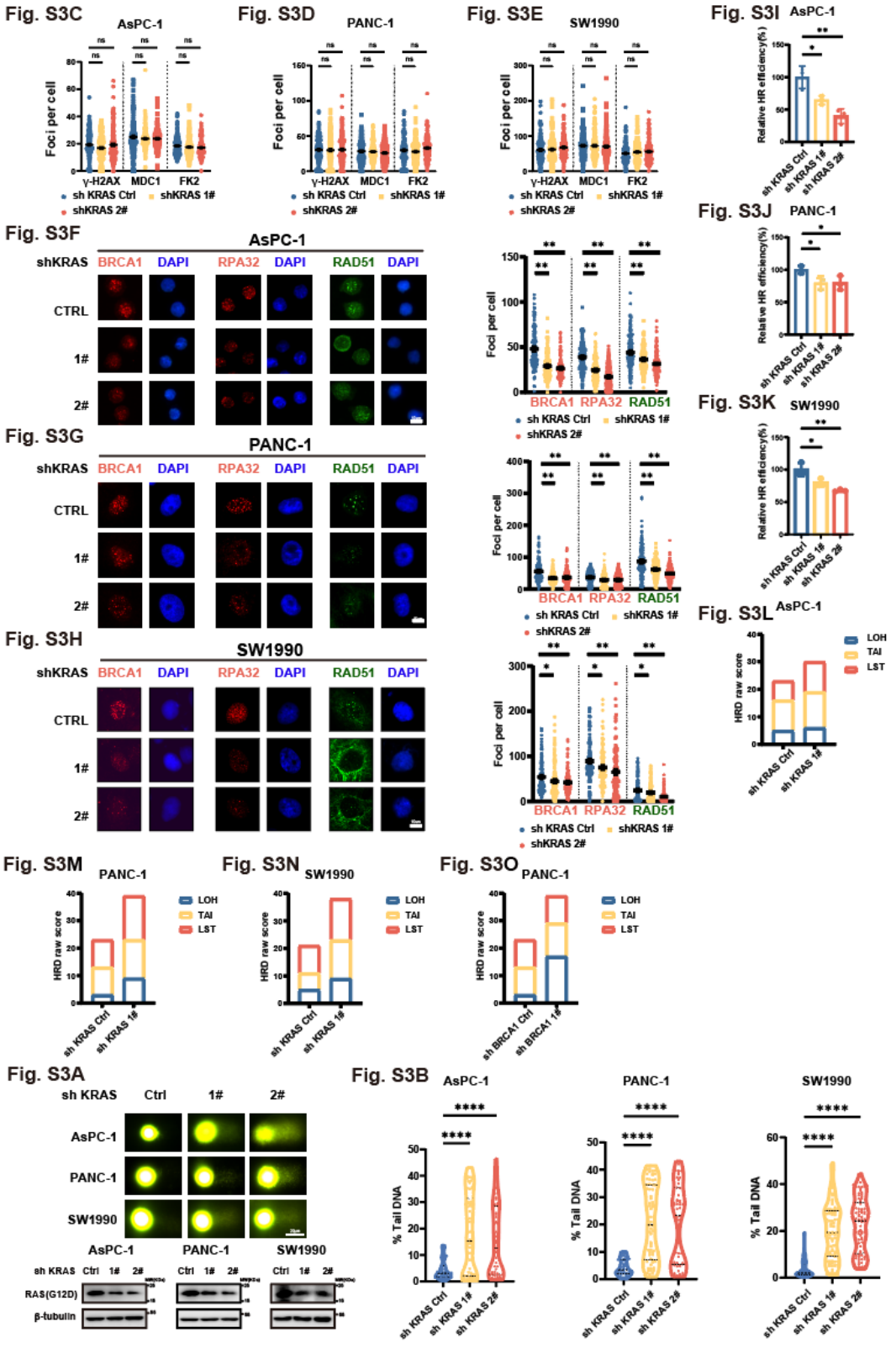

Supplementary Figure 3C-E. Quantification of early DNA damage response foci (γ-H2AX, MDC1, FK2) in AsPC-1 (C), PANC-1 (D), and SW1990 (E) cells following KRAS knockdown. Data are presented as scatter plots, where each dot represents a

single cell (n>100), and the black bar indicates the mean ± SEM. Statistical significance was determined by one-way ANOVA. Ns represents no significant. The scale bar indicates 10 μm.

Supplementary Figure 3F-H. Immunofluorescence analysis of key HR protein foci in AsPC-1 (F), PANC-1 (G), and SW1990 (H) cells after KRAS knockdown. For each cell line, representative images (left) and quantification (right) of BRCA1, RPA32, and RAD51 foci are shown. Quantification is presented as scatter plots, where each dot is a single cell (n>100), and the black bar indicates the mean ± SEM. Statistical significance was determined by one-way ANOVA tests (*P < 0.05, **P < 0.01).

Supplementary Figure 3I-K. HR efficiency in KRAS-knockdown cells using the DR-GFP reporter system. Measurement of homologous recombination (HR) efficiency in AsPC-1 (I), PANC-1 (J), and SW1990 (K) cell lines following KRAS knockdown, assessed via the DR-GFP reporter system and flow cytometry analysis. Data represent mean ± SEM was shown. Statistical significance of differences was determined by one-way ANOVA (*P < 0.05, **P < 0.01).

Supplementary Figure 3L-O. HRD scores in pancreatic cancer cell lines with different KRAS expression. (L-N) Bar graphs depicting HRD scores, including loss of heterozygosity (LOH), telomeric allelic imbalance (TAI), and large-scale state transitions (LST), in control (Ctrl) and KRAS-knockdown (1#) conditions for AsPC-1 (L), PANC-1 (M), and SW1990 (N) cell lines. KRAS knockdown modestly elevated HRD scores (AsPC-1: LOH from 5 to 6, TAI from 11 to 13, LST from 7 to 11; PANC-1: LOH from 3 to 9, TAI from 10 to 14, LST from 10 to 16; SW1990: LOH from 5 to 9, TAI from 6 to 14, LST from 10 to 15). (O) As a positive control, BRCA1 knockdown (shBRCA1) in PANC-1 cells markedly increased HRD scores (LOH from 3 to 17, TAI from 10 to 12, LST from 10 to 10).

Supplementary Figure 3A. Comet assay analysis of DNA damage in KRAS-knockdown cells. (A) Representative images from comet assays performed on three KRASG12D mutant pancreatic cancer cell lines (AsPC-1, PANC-1, and SW1990) after transduction with two different shRNAs targeting KRAS (1#, 2#) compared to a non-targeting control (Ctrl). Western blot confirming the successful knockdown of KRAS protein by the shRNAs. β-tubulin serves as a loading control

Supplementary Figure 3B. Quantification of DNA damage (A) using tail DNA percentage as the metric. Data are presented as violin plots, where each dot represents a single comet (n≥50 per group) (****P < 0.0001).

Fig. S9K

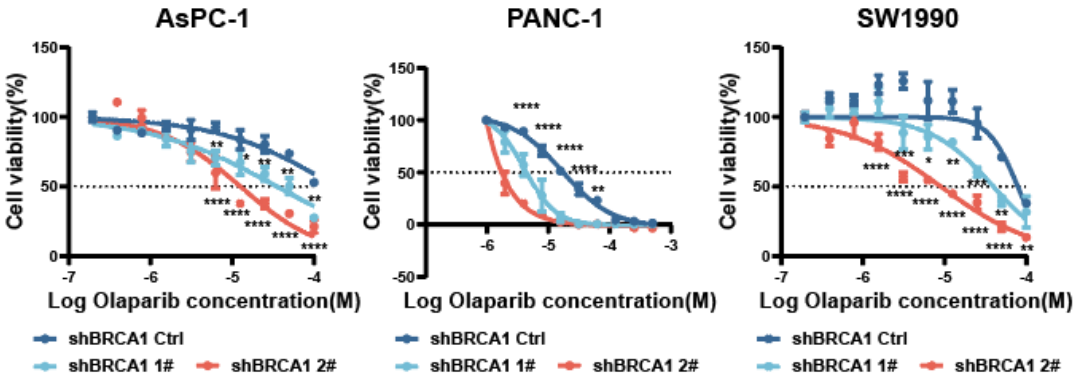

Supplementary Figure 9K. BRCA1 knockdown sensitizes KRAS^{G12D} pancreatic cancer cells to Olaparib. Dose-response curves were generated by CCK8 assay. Data are presented as mean ± SEM. Statistical significance was determined by two-way ANOVA comparing each knockdown line to the control(*P < 0.05, **P < 0.01, ***P < 0.001, ****P < 0.0001).

COMMENT 4. As I already said above, the emergence of resistance is overlooked in this work. The authors should conduct long-term studies to investigate resistance mechanisms to KRAS inhibitors and/or the combination with the respect to the HR-deficient phenotype. Moreover, I think it is very important for the authors to evaluate pathway dynamics (e.g., pERK levels) over time to understand the kinetics of pathway rewiring after KRAS inhibition.

RESPONSE 4#: We thank the reviewer for raising this important point regarding the clinical challenge of resistance to KRAS inhibitors and its implications for the HR-deficient phenotype. To investigate resistance mechanisms and pathway dynamics over time, we performed time-course analyses and established MRTX1133-resistant KRAS^{G12D} cell lines (AsPC-1-R, PANC-1-R, SW1990-R) through chronic exposure to escalating drug doses **(Fig. S12A–C).**

In parental cells, pERK and pAKT suppression was transient, with pathway activity

recovering within 48–72 h, consistent with rapid MAPK/PI3K feedback rewiring **(Fig. 6D–F)**. Importantly, even after downstream reactivation, HR suppression persisted, as shown by sustained downregulation of BRCA1, RAD51, and RPA32, reduced HR-foci formation, and decreased DR-GFP repair efficiency **(Fig. 6D–I).**

In the resistant derivatives, re-treatment with MRTX1133 failed to inhibit pERK/pAKT, confirming pathway reactivation as a dominant resistance mechanism **(Fig. 6D–F)**. Nevertheless, the HR-deficient phenotype remained intact **(Fig. 6I)**, demonstrating that $KRAS^{G12D}$ inhibition decouples HR suppression from canonical MAPK/PI3K signaling.

To evaluate whether this phenotype translates into therapeutic efficacy, we assessed the combination of MRTX1133 + olaparib in both resistant cell lines and resistant xenograft models. In vitro, resistant cells retained robust synergy (Bliss > 15; HSA, ZIP, and Loewe scores 7–18) between the two agents (**Fig. 6J–L**). Consistently, in vivo studies using SW1990-R and PANC-1-R xenografts (n=6 per group) showed that MRTX1133 monotherapy was ineffective, whereas the combination achieved marked tumor growth suppression (**Fig. 7A–F**). Histological analyses confirmed sustained HR deficiency (RAD51 loss) and increased DNA damage and apoptosis markers (γ-H2AX and cleaved caspase-3; **Fig. 7G–P**).

Together, these results demonstrate that $KRAS^{G12D}$ inhibition continues to suppress HR despite downstream pathway reactivation and that the combination regimen remains effective in resistant settings. This indicates that $KRAS^{G12D}$ inhibition decouples HR suppression from MAPK/PI3K feedback reactivation, supporting its potential as a durable therapeutic strategy for $KRAS^{G12D}$-driven cancers.

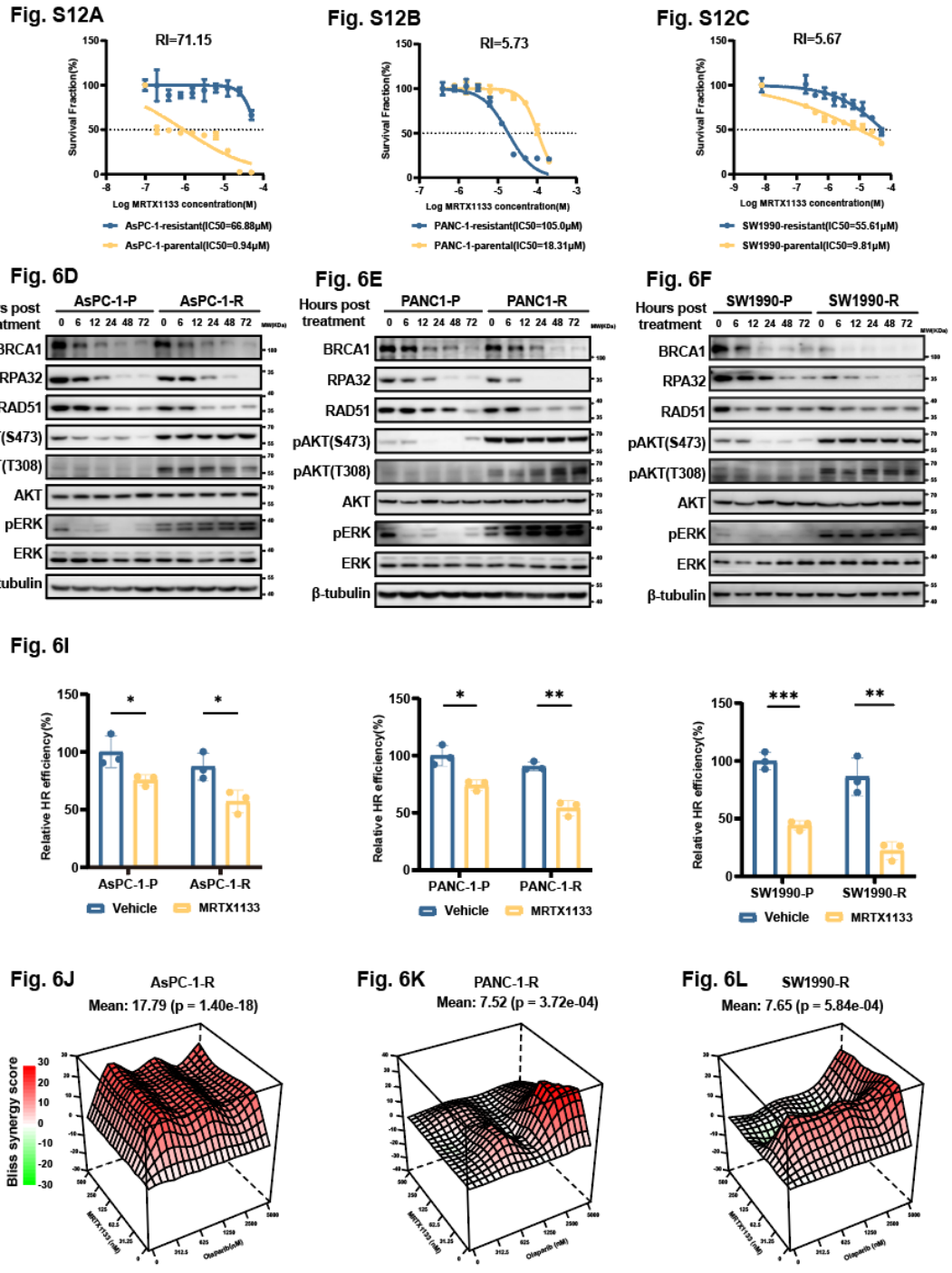

Supplementary Figure 12A-C. Establishment and validation of MRTX1133-resistant cell lines. Dose-response curves show the increased IC50 values for MRTX1133 in resistant (-R) versus parental cell lines for AsPC-1 (A), PANC-1 (B), and SW1990 (C). The Resistance Index (RI) is the ratio of IC50 values (resistant/parental).

Figure 6D-F. Time-dependent effects of MRTX1133 on HR and signaling proteins. Parental (P) and resistant (R) cells were treated with 50 nM MRTX1133 for the indicated times (6-72 hours). Protein levels were assessed by Western blot as described

above.

Figure 6G-H. Immunofluorescence assay for HR-related protein in MRTX1133-resistant KRASG12D PDAC cell lines. Representative immunofluorescence images (G) and quantification (H) of BRCA1, RPA32, and RAD51 foci in resistant cell lines are shown. For quantification, data from one representative experiment are presented as a scatter plot ($n \geq 100$ cells), with black bars indicating the mean. Statistical significance was determined by the unpaired Student's t-test (*P<0.05, **P<0.01). The experiment was repeated three times independently with similar results.

Figure 6I. MRTX1133 treatment reduces HR repair efficiency. Parental and resistant cells were treated with MRTX1133 (50 nM) for 24 hours, and HR efficiency was measured using a DR-GFP reporter assay. Data are shown as mean ± SEM of technical replicates (n=3) from one representative experiment. Statistical significance was determined by the unpaired, two-tailed Student's t-test (*P<0.05, **P<0.01, ***P<0.001). This experiment was also repeated three times with similar results.

Figure 6J-L. Synergistic anti-tumor effect of MRTX1133 combined with Olaparib in resistant pancreatic cancer cells. Three-dimensional synergy plots show the interaction between MRTX1133 and Olaparib in AsPC-1-R (J), PANC-1-R (K), and SW1990-R (L) cells after 144 hours of treatment. Red peaks indicate synergy, and green valleys indicate antagonism. The overall mean synergy score and p-value for each combination are shown in the title of each plot.

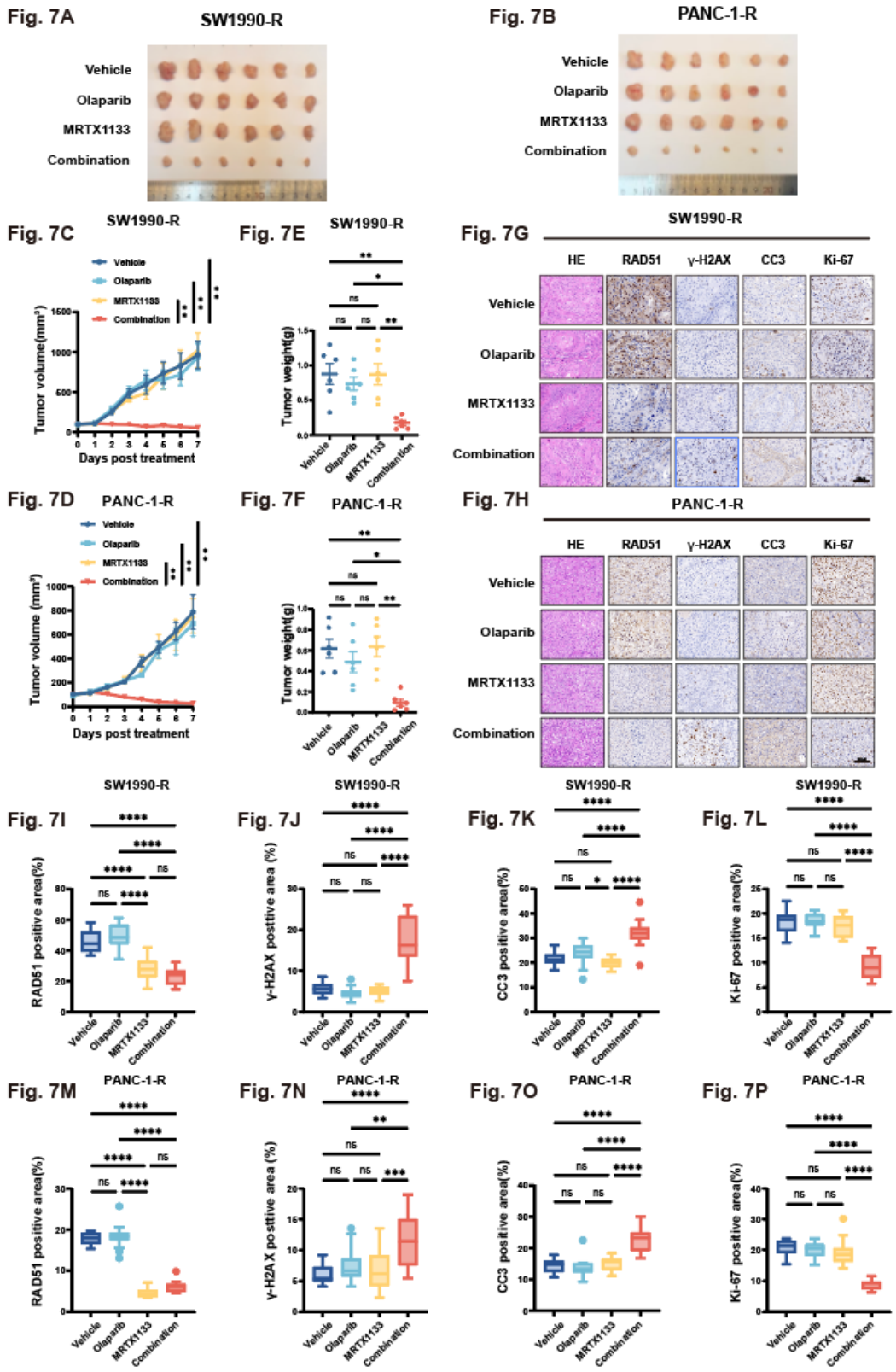

Figure 7A. Represent image of tumors of SW1990-R cell derived xenograft.

Figure 7B. Represent image of tumors of PANC-1-R cell derived xenograft.

Figure 7C-F. Tumor volume (C-D) and weight (E-F) of mice bearing SW1990-R cells (C, E) and PANC-1-R cells (D, F). When tumors reached approximately 80-120 mm³,

treatment was initiated (defined as Day 0). Mice (n=6 per group) were treated daily with vehicle, MRTX1133 (30 mg/kg), olaparib (50 mg/kg), or the combination. Statistical significance was determined by Two-way ANOVA for (C, D), one-way ANOVA for (E-F). Ns, no significant. *P<0.05, **P<0.01. Mean ± SEM shown.

Figure 7G-H. Tumor tissues from SW1990-R and PANC-1-R xenografts were subjected to HE and IHC analyses and probed with indicated antibodies. Representative images(20× magnification) of IHC are shown with treatment indicated. The scale bar indicates 50 μm. CC3: cleaved-caspase 3.

Figure 7I-P. Quantification of indicated markers shown in (G-H). Data are presented as box-and-whisker plots. For quantification, tissues from 3 mice per group were analyzed, with 5 randomly selected high-power fields quantified per tumor. Statistical significance was determined by one-way ANOVA. Ns, no significant. *P<0.05, **P<0.01, ***P<0.001, ****P<0.0001.

COMMENT 5. To the clinical relevance of the work, I think that it would be very important to investigate potential synergism with cis-platinum and exclude activity from other chemotherapy agents commonly used in pancreatic cancer.

RESPONSE 5: We thank the reviewer for this valuable recommendation, which enhances the clinical relevance of our study by testing potential synergy with standard chemotherapeutic agents used in pancreatic cancer, particularly those that exploit HR deficiency. To address this, we systematically evaluated the effects of MRTX1133 in combination with cisplatin, gemcitabine, or paclitaxel in $KRAS^{G12D}$-mutant PDAC cell lines (AsPC-1, PANC-1, SW1990).

In vitro drug combination assays showed robust synergy with cisplatin, with Bliss scores >15 and consistent synergy across HSA, ZIP, and Loewe models (**Fig. 3D; Fig. S9E**). This finding aligns with the expected hypersensitivity of HR-deficient cells to platinum-based agents, as cisplatin directly induces DNA crosslinks that require HR for repair. In contrast, combinations of MRTX1133 with gemcitabine or paclitaxel produced minimal or no synergy (Bliss <10; most HSA/ZIP/Loewe <10; **Fig. S9F–I**), confirming that these effects are specific to HR-dependent DNA-damaging agents rather than general cytotoxic synergy.

Together, these results demonstrate that $KRAS^{G12D}$ inhibition selectively enhances sensitivity to platinum-based chemotherapy through HR suppression, while excluding nonspecific effects with other standard agents. These data have been incorporated into the revised manuscript (**Fig. 3D, Fig. S9E–I**) and discussed as additional evidence of the translational potential of the $KRAS^{G12D}$ + DNA damage–targeting strategy in pancreatic cancer.

Fig. 3D

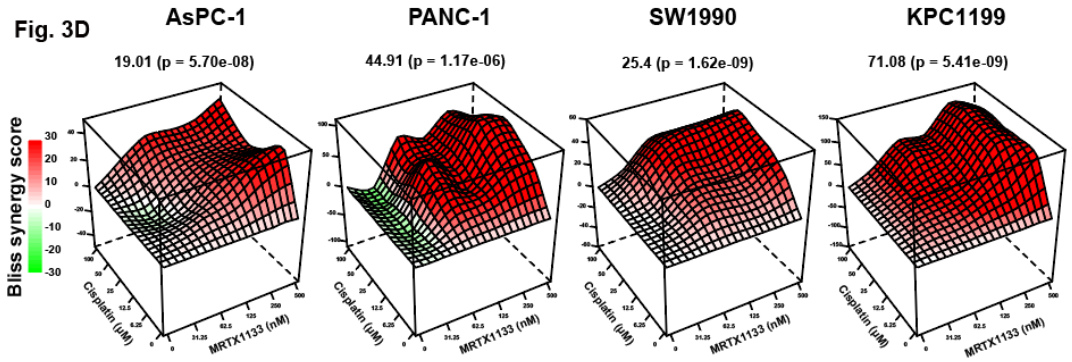

Fig. S9E

Synergy score(MRTX1133 & Cisplatin)

Cell lines	Loewe	HSA	ZIP
AsPC-1	12.94	14.56	19.64
PANC-1	30.74	30.30	40.54
SW1990	35.79	39.07	25.57
KPC1199	59.44	54.85	73.55

Fig. S9G

Synergy score(MRTX1133 & Gemcitabine)

Cell lines	Loewe	HSA	ZIP
AsPC-1	2.79	3.62	-7.44
PANC-1	5.28	6.41	-0.08
SW1990	11.23	14.79	5.95
KPC1199	7.89	3.50	2.24

Fig. S9I

Synergy score(MRTX1133 & Taxol)

Cell lines	Loewe	HSA	ZIP
AsPC-1	4.84	5.53	-3.07
PANC-1	6.55	7.04	3.78
SW1990	2.91	3.51	-1.30
KPC1199	8.23	11.63	-0.69

Fig. S9F

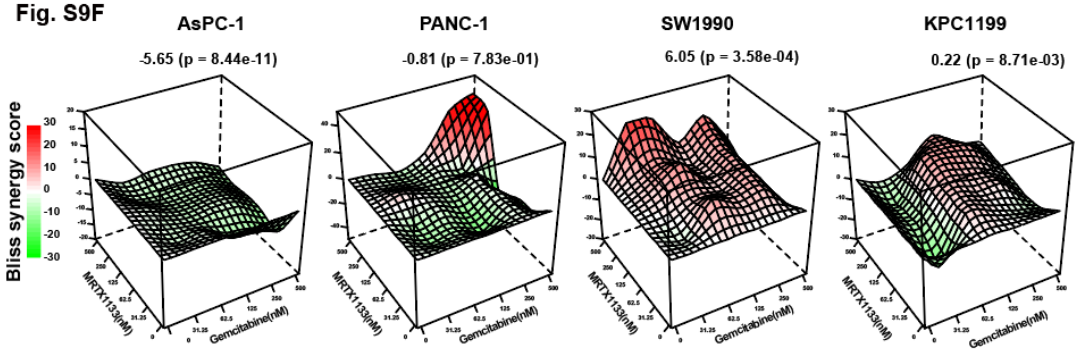

Fig. S9H

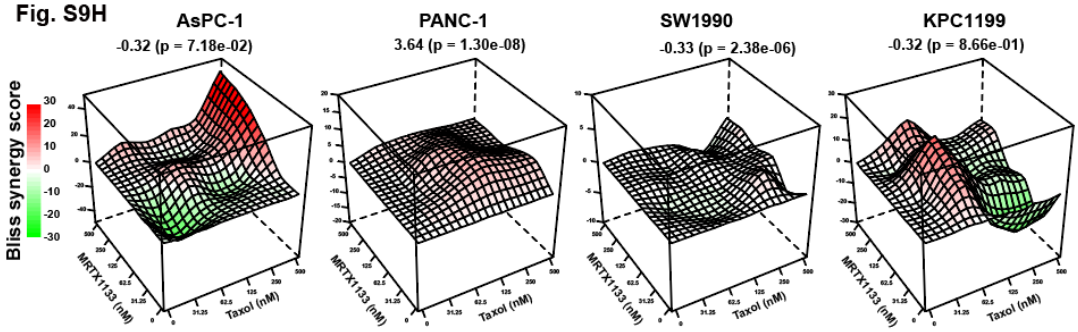

Figure 3D. Evaluation of the synergistic score of KRAS^{G12D} cell lines to combination treatment of MRTX1133 with Cisplatin for 96 h with Bliss model.

Supplementary Figure 9E. Synergy score of Cisplatin combined with MTRX1133. Synergy score was analyzed using HSA, Loewe and ZIP models and listed in the table.

Supplementary Figure 9F. 3D Bliss synergy landscapes for four KRAS^{G12D} cell lines treated with combinations of MRTX1133 and Gemcitabine. Red peaks indicate synergy, while green valleys indicate antagonism.

Supplementary Figure 9G. Synergy score of Gemcitabine combined with MTRX1133.

Synergy score was analyzed using HSA, Loewe and ZIP models and listed in the table.

Supplementary Figure 9H. 3D Bliss synergy landscapes for four KRASG12D cell lines treated with combinations of MRTX1133 and Taxol.

Supplementary Figure 9I. Synergy score of Taxol combined with MTRX1133. Synergy score was analyzed using HSA, Loewe and ZIP models and listed in the table.

COMMENT 6. Finally, if the activation of the immune system is responsible for the in vivo efficacy of the drug, this should be investigated deeply. For example, performing experiments with mouse pancreatic cancer cells in immunodeficient and immunocompetent settings. Alternatively, the authors might consider the specific depletion of CD8+ T cells to further distinguish immune-related effects from direct tumor effects. Moreover, the authors should assess the effect of treatment on the composition and activation status of tumor microenvironment cells, potentially using single-cell sequencing or cytometric analysis.

RESPONSE 6: We thank the reviewer for this valuable comment highlighting the need to clarify the immune contribution to the therapeutic efficacy of the $KRAS^{G12D}$ and PARP inhibitor combination. To address this, we performed additional *in vivo* and *ex vivo* experiments focusing on the role of $CD8^+$ T cells and the tumor immune microenvironment using immunocompetent settings.

To directly assess the requirement of $CD8^+$ T cells, we conducted $CD8^+$ T-cell depletion experiments in C57BL/6 mice bearing subcutaneous KPC1199 tumors. When tumors reached approximately 100 mm^3, mice received anti-CD8α antibodies (or isotype control) intraperitoneally every three days throughout treatment with MRTX1133 (30 mg/kg) and olaparib (50 mg/kg) for seven consecutive days (dosing schematic shown in **Fig. 9J**). In control (IgG-treated) mice, the combination treatment significantly reduced tumor volume and weight compared to monotherapies ($p < 0.05$; **Fig. 9J–M**). In contrast, $CD8^+$ T-cell depletion abolished this therapeutic benefit, resulting in tumor

growth comparable to vehicle-treated controls (**Fig. 9J–M**). These findings demonstrate that CD8⁺ T cells are essential mediators of the antitumor effect of the combination regimen.

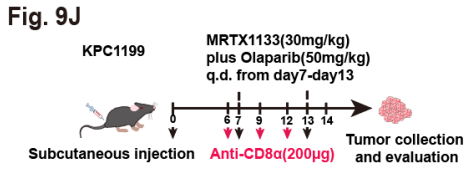

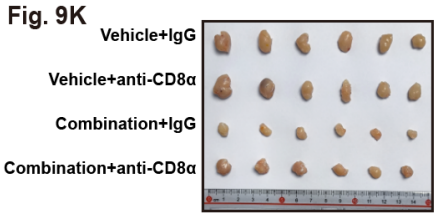

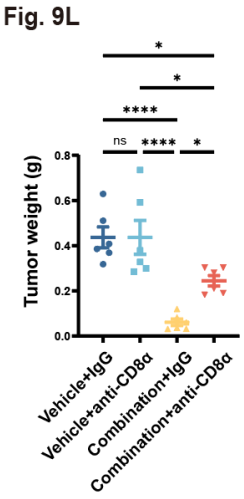

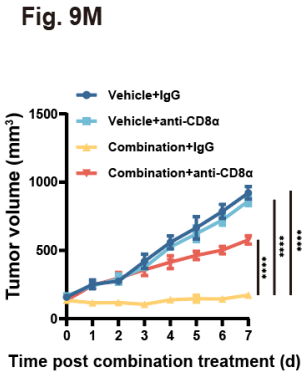

Figure 9J. Schematic of the dosing regimen for the CD8+ T cell depletion study in the subcutaneous KPC1199 tumor model. Immunocompetent C57BL/6J mice were subcutaneously inoculated with KPC1199 cells on day 0 to establish syngeneic tumors. CD8+ T cell depletion was initiated on day 6 with intraperitoneal administration of anti-CD8 antibodies (200 μg/dose) or isotype controls, repeated every 3 days throughout the study. Combination therapy with MRTX1133 (30 mg/kg intraperitoneal daily) and Olaparib (50 mg/kg intraperitoneal daily) commenced on day 7 and continued for 7 days (day7-day13). Vehicle controls were administered in parallel. Tumor volumes were monitored every day until the endpoint on day 14, at which point tumors were harvested for weight measurement and further analyses.

Figure 9K. Representative images of harvested tumors from the CD8+ T cell depletion study at the experimental endpoint (Day 14).

Figure 9L-M. Tumor weight (L) and volume (M) of mice bearing KPC1199. Mice were treated with vehicle+IgG(200 μg),vehicle+anti-CD8α(200 μg), combination(Olaparib 50 mg /kg; qd, MRTX1133 30mg/kg; qd)+IgG(200 μg), combination+anti-CD8α(200 μg). 6 animals per group. Statistical significance was determined by one-way ANOVA for (L) and two-way ANOVA for (M). Data are represented as the Mean ± SEM. *P<0.05, ****P<0.0001; ns, no significant.

In parallel, to comprehensively evaluate the tumor immune microenvironment, we conducted single-cell RNA sequencing (scRNA-seq) on subcutaneous tumors across

treatment groups. This revealed enhanced infiltration of CD8+ T cells and NK cells in the combination treatment group compared to monotherapy or controls (**Fig. 8A-B, Fig. S13F, G**). Further analysis of T cell subsets revealed that $CD8^+$ effector T cells and $CD4^+$ T cells were enriched in the combination treatment group (**Fig. 8C-D, Fig.S13H, I**). Notably, effector T cell scores (based on gene signatures for cytotoxicity and activation) were highest in the combination group (**Fig. 8E**), supporting enhanced functional activity of infiltrating T cells.

Third, to complement the scRNA-seq, we conducted flow cytometry on dissociated tumors from all treatment groups. This confirmed elevated levels of $CD4^+$ and $CD8^+$ T cells in the combination group(**Fig. 8F**), along with increased expression of TNF-α as markers of activation and cytotoxicity(**Fig. 8G**). Interestingly, PD-1 expression was reduced (**Fig. 8H**), suggesting diminished T cell exhaustion and potentially enhanced effector function. These quantitative data are included in new Figure 8.

Collectively, these results demonstrate that the immune activation induced by combined $KRAS^{G12D}$ and PARP inhibition is driven by $CD8^+$ T-cell–mediated cytotoxicity, and that the in vivo efficacy of the therapy depends on adaptive immune engagement. These new data have been incorporated into the revised manuscript (**Fig. 8, 9 and Fig. S13**) and discussed to highlight the immune-dependent mechanism underlying the enhanced therapeutic response.

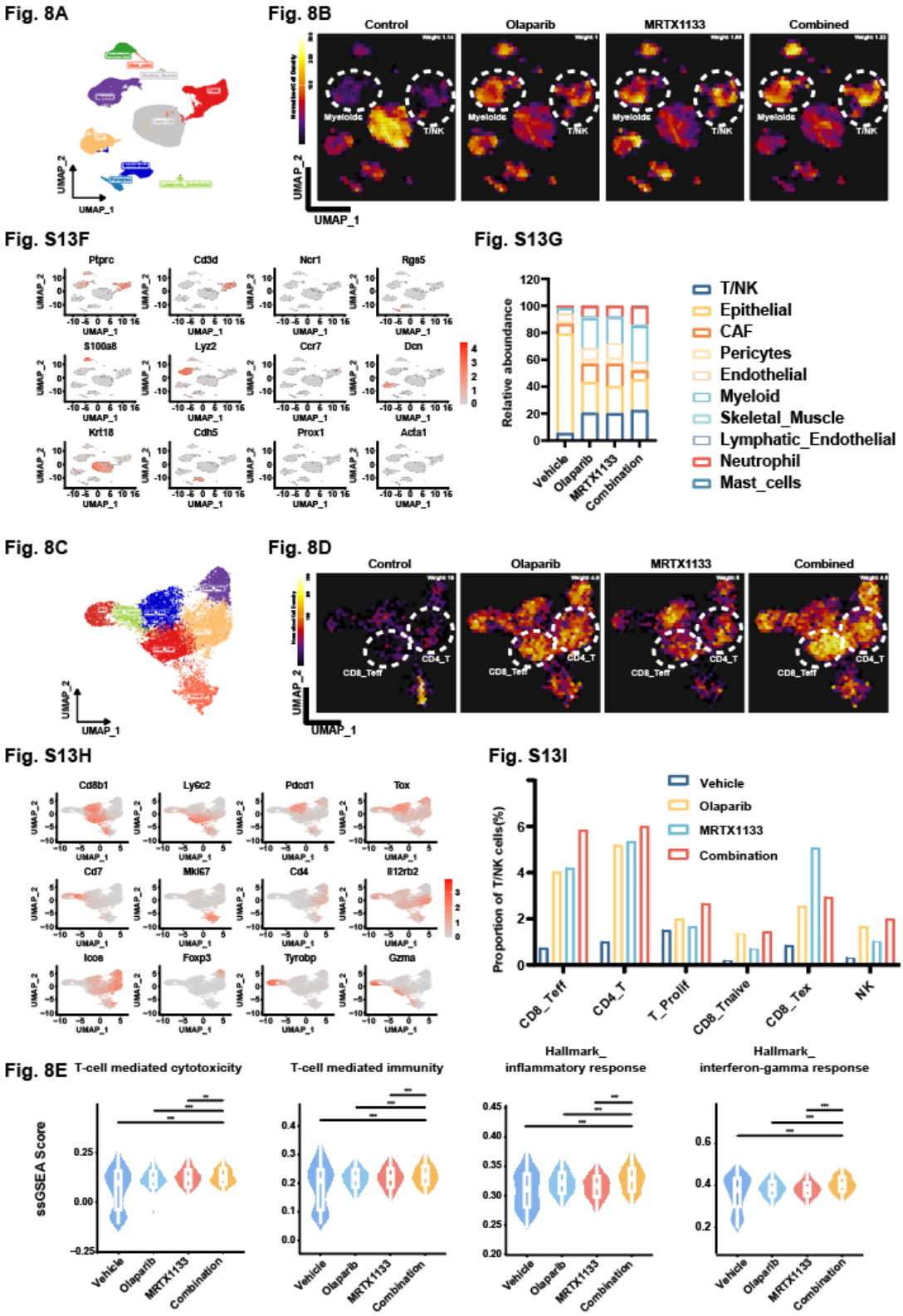

Figure 8A. Uniform Manifold Approximation and Projection (UMAP) plot of all identified cell types from pooled single-cell RNA sequencing data. Cells were sourced from KPC-1199 tumors grown in C57BL/6J mice and treated with vehicle,

olaparib, MRTX1133, or the combination for 7 days. Color coding indicates distinct cell clusters. CAF: Cancer-Associated Fibroblast.

Figure 8B. UMAP density plots comparing the distribution and density of major immune cell compartments across the four treatment groups. Normalized cell density is visualized by color (purple: low, yellow: high). Annotated clusters indicate major immune cell types, including T/NK (T and Natural Killer) cells and Myeloid cells.

Supplemental Figure 13F. UMAP feature plots showing the expression of canonical marker genes used to identify major cell lineages within the tumor microenvironment.

Supplemental Figure 13G. Stacked bar chart showing the relative abundance of major cell populations across the four treatment groups, as determined from the scRNA-seq data.

Figure 8C. UMAP plot showing the refined sub-clustering of the T and Natural Killer (T/NK) cell populations identified in (Figure 8A).

Figure 8D. UMAP density plots comparing the distribution of T cell subsets across the four treatment groups. Annotated clusters highlight key T cell subtypes, including CD8_Teff (CD8+ effector T cells) and CD4_T (CD4+ T cells).

Supplemental Figure 13H. UMAP feature plots displaying the expression of key marker genes used to further define T-cell and NK-cell subsets.

Supplemental Figure 13I. Bar chart showing the proportion of specific T-cell and NK-cell subsets as a percentage of the total T/NK cell population in each treatment group. (Teff: effector T-cell; T_Prolif: proliferating T-cell; Tnaive: naive T-cell; Tex: exhausted T-cell).

Figure 8E. Violin plots showing single-sample Gene Set Enrichment Analysis (ssGSEA) scores for four key immune-related signatures across the treatment groups. In each plot, the white dot represents the median, and the thick bar indicates the interquartile range. Statistical significance was determined by one-way ANOVA. **P<0.01, ***P<0.001.

Fig. 8F

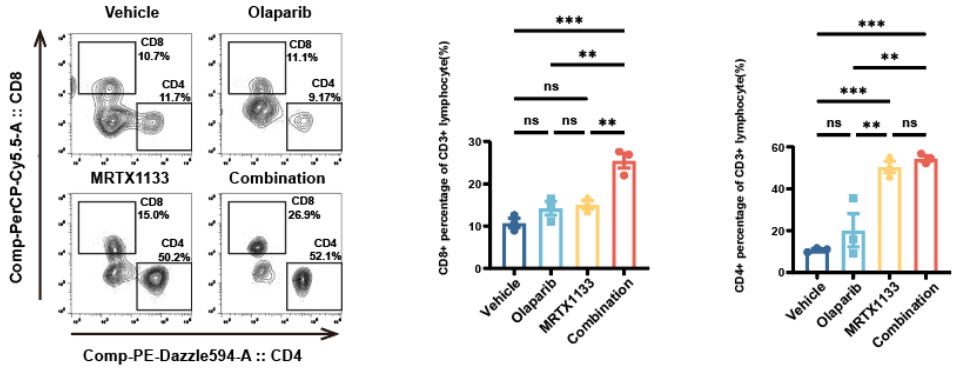

Fig. 8G

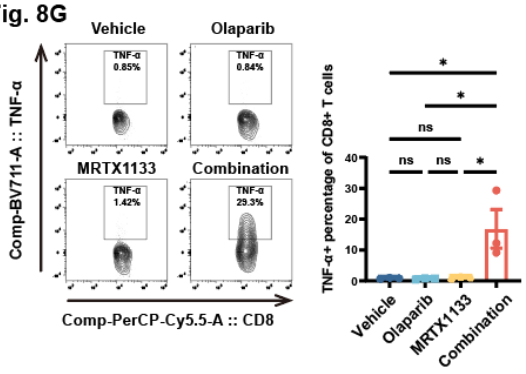

Fig. 8H

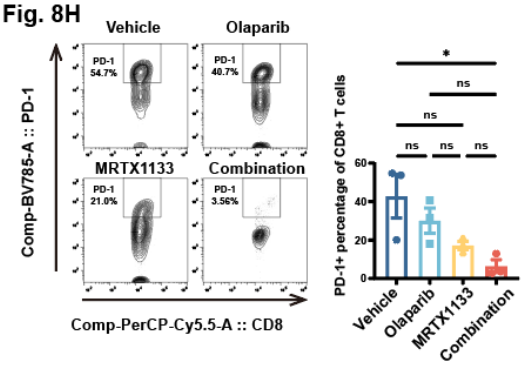

Figure 8F. Representative flow cytometry plots (left) and quantification (right) of CD4+ and CD8+ T cells within the total CD3+ lymphocyte population in tumors. For quantification, the bar graph represents the mean ± SEM, with individual data points from each mouse shown (n=3 per group). Statistical significance was determined by one-way ANOVA (**P < 0.01, ***P < 0.001, ns, no significant).

Figure 8G. Representative flow cytometry plots (left) and quantification (right) showing the percentage of TNF-α-producing cells within the CD8+ T cell population. For quantification, the bar graph represents the mean ± SEM, with individual data points from each mouse shown. Statistical significance was determined by one-way ANOVA (*P < 0.05, ns, no significant).

Figure 8H. Representative flow cytometry plots (left) and quantification (right) showing the percentage of PD-1-expressing cells within the CD8+ T cell population. For quantification, the bar graph represents the mean ± SEM, with individual data points from each mouse shown. Statistical significance was determined by one-way ANOVA(*P < 0.05, ns, no significant).

COMMENT 7. Finally, I found quite difficult to follow the manuscript when it comes to treatment timepoints. The (in vivo) treatment seems to last from 10 to 14 days. Then, the tumor burden is assessed at 7 days in the immunodeficient setting and at 7 and 14 days in the immunocompetent setting (using KPC derived cell lines). This is also in contrast with the timeline of the survival experiments. It is very confusing. The authors should be more clear in outlining the timeline of the experiments, which again is quite important considering the dynamics of pathway rewiring.

RESPONSE 7#: We thank the reviewer for pointing out the confusion regarding experimental timelines. We apologize for the lack of clarity in the original submission and have carefully revised both the figures and the Methods section to clearly define the treatment schedules for all in vivo models. The correction also includes an updated **Figure 4A**, where the treatment duration in the immunodeficient model was previously mislabeled.

Specifically, the timeline has now been clarified as follows:

- Immunodeficient models (SW1990 and PANC-1 xenografts): Subcutaneous tumor implantation was performed on day 0, and treatment (vehicle, MRTX1133 [30 mg/kg], olaparib [50 mg/kg], or the combination) was initiated once tumors reached ~100 mm^3 (typically day 12). Dosing was performed daily for 7 days (day 12–18), and tumors were collected on day 19 for endpoint analyses (tumor weight, histology, and molecular assays).
- Immunocompetent models (KPC1199): Treatment was similarly administered daily for 7 days following tumor establishment. Tumor progression was monitored by bioluminescence at day 7 and day 14 to evaluate short-term and intermediate responses, including pathway rewiring and immune activation. Complete tumor regression was frequently observed by day 14 in the combination group, which precluded molecular analysis at that point. To compensate, we extended the observation period in separate cohorts to allow sample collection for histological and immunological characterization after

tumor relapse or at later stages of response.

- Survival studies: Conducted independently in the KPC1199 immunocompetent model, with daily dosing for up to 30 days or until humane endpoints. To avoid confounding survival data, no interim tissue sampling was performed. Tumors from control animals were collected at the onset of morbidity, while remaining mice were euthanized at the experimental endpoint for IHC, WB, and RT-qPCR analyses. The Kaplan–Meier survival curve (now **Fig. 9C**) shows a significant survival benefit for the combination group (log-rank p = 0.0004 vs. vehicle).

Together, these revisions ensure consistent and transparent reporting of experimental durations across immunodeficient, immunocompetent, and survival studies, clarifying the relationship between treatment windows, pathway dynamics, and immune remodeling.

Specific Comments

Figures and Analysis

•Figure 1A: Clearly indicate how many cases are included in the analysis and justify the use of non-KRAS G12D as a control. Would non-G12D KRAS alleles be more appropriate?

RESPONSE: We appreciate the reviewer's thoughtful feedback. In the revised Figure 1A, we have reanalyzed the TCGA PDAC cohort and categorized cases into three distinct groups to enhance clarity and interpretability: KRAS wild-type (n = 64), KRAS non-G12D mutant alleles (n = 60), and $KRAS^{G12D}$ mutant (n = 42). The updated Kaplan–Meier survival analysis revealed significant survival differences among these groups. Specifically, patients harboring $KRAS^{G12D}$ mutations exhibited markedly worse overall survival compared with both wild-type ($p < 0.005$) and non-G12D KRAS mutant cases ($p = 0.02$). Additionally, a moderate but statistically significant difference was observed between wild-type and non-G12D mutant groups ($p = 0.04$).

We agree that comparing $KRAS^{G12D}$ with other KRAS mutant alleles is a more appropriate control for isolating allele-specific effects. Accordingly, we now include a

separate differential expression analysis directly comparing KRAS^{G12D} versus other KRAS mutants (G12V, G12C, and G13D) in the revised figure. These updated results reinforce the conclusion that KRAS^{G12D} confers a uniquely adverse prognostic signature among KRAS variants.

We appreciate this constructive suggestion, which has improved both the analytical rigor and the clarity of our presentation, ensuring that the prognostic distinction of KRAS^{G12D} is clearly delineated.

Fig. 1A

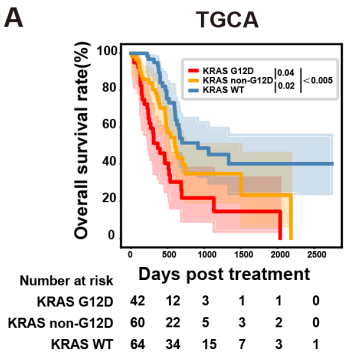

Figure 1A. Harboring KRAS ^{G12D} predicted a poorer survival in PDAC patients. Kaplan–Meier overall survival analysis of PDAC patients from the TCGA cohort stratified by KRAS mutation status. Patients were grouped into KRAS wild-type (n = 64), KRAS non-G12D mutant alleles (n = 60), and KRAS G12D mutant (n = 42). "Number at risk" values are shown below the Kaplan–Meier curves. The survival difference among the three groups was statistically significant, with G12D mutants showing the worst prognosis. Log-rank test was used to assess statistical significance. PDAC: Pancreatic adenocarcinoma.

•Figure 1B: The GSEA analysis is not convincing. Adjust for false discovery rate (FDR) and use appropriately sized gene sets. Sparse or small gene sets reduce the validity of the results.

RESPONSE: We thank the reviewer for this valuable feedback on the GSEA analysis in **Figure 1B**, which we agree is crucial for ensuring robust interpretation of pathway

enrichments. To address concerns regarding false discovery rate (FDR) adjustment and gene set size, we have re-analyzed the data using the Reactome database[5], which provides well-curated, pathway-focused gene sets with sufficient size and biological relevance. This approach mitigates issues with sparse or undersized sets, enhancing the validity and reliability of the results.

Specifically, we performed GSEA on differentially expressed genes from patients harboring $KRAS^{G12D}$ mutations(n=42) vs. patients bearing KRAS non-G12D allele(n=125). RNA-seq data processed with DESeq2, log2 fold-change >1, adjusted p <0.05). Using Reactome gene sets (via clusterProfiler R package), we applied FDR adjustment (Benjamini-Hochberg method) to control for multiple testing. This yielded significant enrichments in multiple pathways related to DNA damage repair and homologous recombination (HR) repair. Gene set sizes ranged from 37 to 330, ensuring adequate representation and reducing bias from small sets. All enriched pathways had NES values between 1.6 and 2.7, with p-adjust <0.05, confirming statistical robustness. These updated results strengthen our findings on HR deficiency induced by $KRAS^{G12D}$ inhibition, aligning with downstream functional assays. We have replaced the original Figure 1B with the new GSEA plot (highlighting pathways related to DNA damage response), updated the Methods section to detail the Reactome-based analysis and FDR adjustment.

Fig. 1B

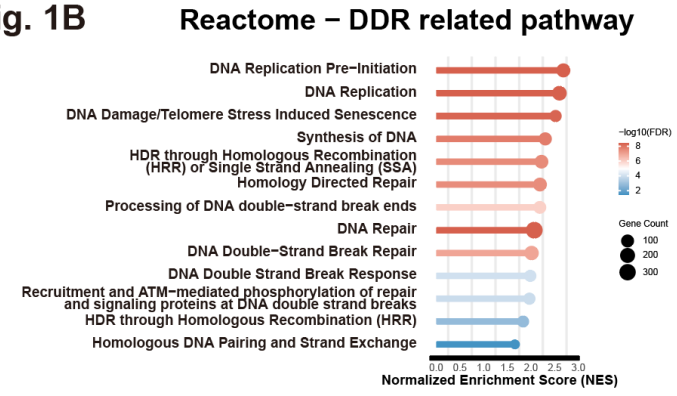

Figure 1B. Gene signature enrichment analysis (GSEA) reveals prominent enrichment of signatures related to Regulation of DNA damage response (DDR) pathways in the $KRAS^{G12D}$ group compared with non-$KRAS^{G12D}$ group. NES: normal enrichment score.

•Figure 1C: Revise the legend. MRTX1133 does not induce DNA damage; rather, it alters the DNA damage response.

RESPONSE: We appreciate the reviewer's observation and agree that the current wording in the legend may be misleading.

We have now revised the legend of **Figure 1C** to clarify that MRTX1133 does not directly induce DNA damage, but rather modulates the DNA damage response (DDR). Specifically, we now state:

"*MRTX1133 alters the DNA damage response*"

This revised description more accurately reflects the mechanism of action and the experimental observations shown in the figure.

•Figure 1E-G: Why reporting surviving fraction and not number or size of colonies; very different concepts/parameters.

RESPONSE: We thank the reviewer for this thoughtful comment. In Figure 1E–G, we chose to present the surviving fraction rather than raw colony number or colony size, as this parameter provides a normalized measure of clonogenic survival that accounts for differences in initial seeding density and plating efficiency among replicates. The surviving fraction represents the ratio of colonies formed after treatment relative to untreated controls, thereby integrating both cell survival (number of colonies formed) and proliferative capacity (colony growth potential).

While absolute colony counts reflect raw survival and colony size may indicate proliferative rate, the surviving fraction is widely recognized as the standard endpoint in clonogenic assays because it allows direct comparison across experimental groups with varying cell growth kinetics or treatment effects. This approach ensures that differences observed reflect true changes in reproductive viability, rather than artifacts of plating variation or growth rate differences.

We have clarified this rationale in the revised **Methods and Figure 1.E-G legend** to better convey why surviving fraction was used as the primary readout.

•Figure 2A-D: Explicitly indicate the timing of analyses.

We thank the reviewer for this comment.

As noted in the figure legend, all immunoblotting analyses in Figure 2A–D were performed after 24 hours of treatment with MRTX1133 at the indicated concentrations. The cell lysates were collected at this single time point for western blot analysis of BRCA1, RPA32, RAD51, phospho-ERK, and phospho-AKT.

To enhance clarity, we have now explicitly stated "*at indicated concentrations for 24h*" at the beginning of the figure legend.

•Figure 2E-H: Address why foci reduction is seen for BRCA1, RPA32, and RAD51 but not for MDC1, FK2, or 53BP1.

RESPONSE: We appreciate the reviewer's insightful comment. The selective reduction of BRCA1, RPA32, and RAD51 foci reflects the specific disruption of homologous recombination (HR) caused by $KRAS^{G12D}$ inhibition. MRTX1133 treatment induces an HR-deficient (HRD) state, impairing the recruitment and activity of key HR mediators: BRCA1 initiates DNA-end resection and facilitates RAD51 loading, RPA32 coats single-stranded DNA intermediates during repair, and RAD51 forms nucleoprotein filaments essential for strand invasion and homology search.

In contrast, MDC1, FK2 participate in early DNA damage signaling rather than HR. MDC1 functions upstream in DNA double-strand break sensing and chromatin remodeling, FK2 marks sites of protein ubiquitination that recruit DNA damage mediators. The unchanged levels of these foci following MRTX1133 treatment suggest that early DDR activation remain intact, while the HR branch is selectively suppressed. Therefore, the loss of BRCA1, RPA32, and RAD51 foci without corresponding reductions in MDC1 and FK2 supports a shift in the DNA repair balance toward NHEJ and reflects an HR-specific vulnerability induced by $KRAS^{G12D}$ inhibition. This mechanistic selectivity reinforces the HRD phenotype that underlies the observed synergy with PARP inhibitors.

•Figure 2I: Correct the DR-GFP reporter system label; it is not an in vivo system.

RESPONSE: We thank the reviewer for this important clarification. We agree that the DR-GFP reporter assay is an in vitro system for quantifying homologous recombination efficiency, not an in vivo model. In the revised manuscript, we have corrected both the figure legend and the relevant sections of the text to explicitly describe it as an in vitro HR repair assay.

We apologize for the earlier mislabeling and appreciate the reviewer's attention to this detail, which has improved the precision and accuracy of our data presentation.

•Figure 3C: Clarify the vehicle used. Address the significant differences in results between human and mouse cells. Is the results consistent across different mouse cell lines?

RESPONSE: We thank the reviewer for these insightful comments.

Vehicle Clarification:

In the experiments depicted in **Figure 3C**, MRTX1133 was prepared from a 5 mM stock in DMSO and diluted to a final concentration of 50 nM in culture medium, yielding a final DMSO concentration of 0.001%. The vehicle control group was treated with an equivalent 0.001% DMSO to match the treatment conditions precisely. This same vehicle formulation was applied to olaparib-treated groups for consistency. We have updated the Figure 3 legend to explicitly state: *Cells were pre-treat with MRTX1133(50nM) or 0.001% DMSO as vehicle for 24h,*

Species-Related Differences:

We acknowledge the observed differences in treatment responses between human PDAC cell lines (AsPC-1, PANC-1 and SW1990) and mouse lines (KPC1199), which may arise from intrinsic species-specific factors such as variations in pathway regulation, drug metabolism, or baseline HR proficiency. Importantly, while the

magnitude of changes in HR markers (e.g., RAD51, BRCA1/2) varied, the directional effect—downregulation following MRTX1133 treatment—was consistent across both species, supporting a conserved mechanism of HR impairment.

Consistency Across Mouse Models:

To further validate reproducibility, we extended our analysis to an additional KPC-derived murine PDAC cell line (KPC1242). Consistent with KPC1199, the vehicle-treated KPC1242 cells exhibited extremely low sensitivity to olaparib. However, pretreatment with MRTX1133 (100 nM, 24 h) markedly increased olaparib sensitivity ($p<0.01$ vs. vehicle). These findings confirm the robustness of our results across different mouse cell lines. The data are now presented in **new Fig. S9B**.

Fig. S9B

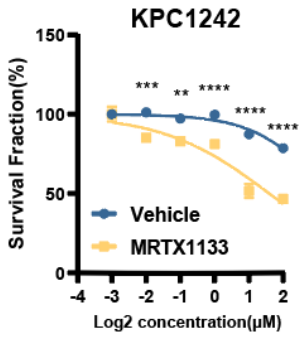

Supplementary Figure 9B. KPC1242 cells for 2-D colony formation in response to Olaparib. KPC1242 cells were pre-treated with MRTX1133 for 24h and then seeded in 6-well plates. Olaparib was conducted. Relative colony formation rate at multiple concentrations was calculated with the colony number at Day10-12 after treatment. Two-way ANOVA was for indicated concentrations. Mean ± SEM shown. **P<0.01,***P<0.001,****P<0.0001.

•Figure 4A: The experimental schematic does not align with the legend.

RESPONSE: We thank the reviewer for pointing out the discrepancy between the experimental schematic and the figure legend. Upon closer inspection, we realize that both the schematic in new **Figure 4A** and the associated legend were inaccurate in depicting the treatment timeline.

To address this, we have revised both the schematic and the legend to accurately reflect the experimental protocol: Treatment was initiated once tumors reached approximately 100 mm^3 (typically around Day 12 post-subcutaneous injection), with daily dosing for 7 days (Days 12-18). Tumor volume was measured on Day 19 (the 7th day post-treatment initiation), after which mice were euthanized and tumors harvested for downstream analyses.

The revised figure legend now reads:

A. Schematic illustration of the in vivo treatment timeline. When tumors reached approximately 80-120 mm^3 (on Day 12 post-injection), treatment was initiated (defined as Day 0). Mice were treated daily with vehicle, MRTX1133 (30 mg/kg), olaparib (50 mg/kg), or the combination for 7 days. On Day 8 post-treatment (Day 19 post-injection), mice were euthanized, and tumors were collected for downstream analyses.

These corrections have been incorporated into the revised manuscript, and we have also added a brief clarification in the Methods section to ensure consistency across all in vivo descriptions. This updated timeline aligns with our immunodeficient model experiments.

•Figure 4H-I and Figure 5H-I: Provide higher-resolution images with appropriate magnification and IHC quantification details (i.e., number of mice per group, number of fields per mouse etc)

RESPONSE: We appreciate the reviewer's suggestion to improve the clarity and reproducibility of our immunohistochemistry (IHC) results.

We have now provided higher-resolution images for both Figure 4H-I, Figure 5H-I and

Figure 8D, with enhanced magnification (20x) to better visualize the staining.Each IHC analysis was conducted using tumor tissues from 3 mice per group. For quantification, we analyzed at least 5 randomly selected high-power fields per tumor. Quantification was performed using ImageJ with standardized thresholding settings, and results are presented as positive-stained area per field (%) , as indicated in the figure legends.

The updated images and corresponding quantification details have been revised in the figures and legends accordingly.

We hope these clarifications and improvements address the reviewer's concern.

•Figure 6A-C: Resolve the timeline discrepancy and provide details of the survival experiment, including the rationale for stopping at day 30 and drug preparation methods.

RESPONSE: We thank the reviewer for pointing out the need for clarity on the timelines and experimental details in new **Figure 9A-C**, which we agree is crucial for accurate interpretation of the in vivo efficacy and survival data. We have addressed these points below and revised the manuscript accordingly.

Timeline Clarification:

Our initial approach in this model involved daily treatment for 7 days, starting after tumor establishment. Tumor monitoring was conducted via bioluminescent imaging at 7 days and 14 days post-treatment initiation (n=3 mice per group) to evaluate both short-term and intermediate-term responses, including pathway rewiring and immune cell dynamics. At the 14-day sampling point, we observed complete tumor regression in the combination treatment group, which precluded tissue-based analyses such as immunohistochemistry (IHC), Western blotting (WB), and RNA extraction for comparative validation.

To overcome this limitation and enable comprehensive molecular and histological assessments, we restructured the model into a long-term survival study. The experiment was designed to run for up to 30 days, with the primary endpoint being the point at

which all mice in the control group had succumbed to tumor burden. This event serves as a critical humane endpoint that is consistent with animal welfare guidelines and provides the maximal window for observing therapeutic benefit in the treatment groups. To avoid confounding survival outcomes, no planned interim tumor sampling was performed. However, to enable comparative molecular analysis, we harvested tumors from control group mice opportunistically as they succumbed. At the conclusion of the study (i.e., when the last control mouse died), tumors were then collected from the surviving mice in the treatment groups. These tissues were used for IHC, WB, and RT-qPCR analyses. The Kaplan-Meier survival curve demonstrates significant improvements in the combination group.

Drug preparation and administration:

Drug Formulation and Administration for MRTX1133 (30 mg/kg, i.p.):

Vehicle Composition: 8% DMSO+40% PEG300+7% Tween-80+45% PBS (pH 7.4)

Formulation Procedure (example: 10 mL total volume): Weigh 60 mg of MRTX1133 to achieve a final concentration of 6 mg/mL. Dissolve the compound in 0.8 mL of DMSO. Add 4.0 mL of PEG300 and 0.7 mL of Tween-80. Mix thoroughly. Add PBS (4.5 mL) to bring the total volume to 10 mL. Filter the final solution through a 0.22 μm syringe filter for sterilization. Inject 100 μL per mouse intraperitoneally to achieve a dosage of 30 mg/kg, assuming an average body weight of ~20 g per mouse. Olaparib was also prepared using the same vehicle for consistency. All drugs were administered via intraperitoneal injection (i.p.), once daily for 7 days. The vehicle control group received i.p. injections of vehicle solution only.

These clarifications and the updated schematic have been incorporated into the figure legend.

•Figures S2E and S4A: Statistical analyses are missing, and the results do not match corresponding main figures.

RESPONSE: We thank the reviewer for identifying the absence of statistical analyses and the inconsistencies between Figures S2E/S4A and the corresponding main figures. In response, we have reanalyzed these datasets, incorporated appropriate statistical testing, and corrected figure labeling errors to ensure accuracy and consistency.

To strengthen the analysis of cell-cycle dynamics, we replaced the previous PI-based method with EdU incorporation assays, which provide a more robust and quantitative assessment of S-phase progression. The updated results **(Supplementary Fig. S6A–E)** show a significant reduction in EdU^+ cells following MRTX1133 treatment at 24, 48, and 72 hours ($n > 100$ cells per time point; unpaired Student's *t*-test, $P < 0.05$), confirming the expected G1/S transition delay. These new data are now included as Supplementary Figure S6, with full statistical details provided in the legend.

Regarding Figure S4A, we identified a data placement error during figure assembly in which treatment group labels were inadvertently swapped between MRTX1133 and Olaparib. We have corrected this error, reanalyzed the raw data, and updated the figure as **Supplementary Figure S10A-B**, now presented as bar graphs showing mean tumor volume change (± SEM, $n = 6$ per group; one-way ANOVA). The corrected results are fully consistent with the tumor volume curves shown in main Figure 4D and 4F.

Finally, the raw data underlying these analyses have been deposited in the Supplementary Materials for transparency. These revisions resolve the prior inconsistencies and enhance both the statistical rigor and reproducibility of the dataset.

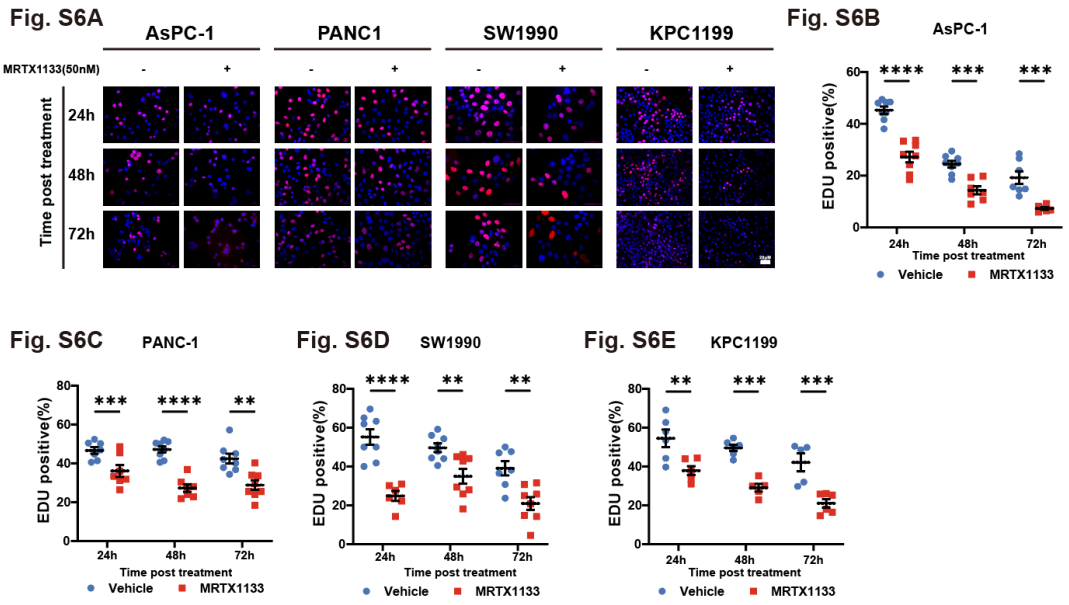

Supplementary Figure 6A-E. G1/S phase staining in MRTX1133-treated cell lines.(A) Representative images of EdU (5-ethynyl-2'-deoxyuridine) staining for G1/S phase detection in pancreatic cancer cell lines (AsPC-1, PANC-1, SW1990 and KPC1199) at 24, 48, and 72 hours following treatment with 50 nM MRTX1133. (B-E) Quantification of EdU-positive cells indicating G1/S phase progression. Data are shown as the mean ± SEM (n > 100 cells per time point from > 5 fields per group). Statistical significance of differences was determined by unpaired Student's t-test (**P<0.01, ***P<0.001, ****P<0.0001).

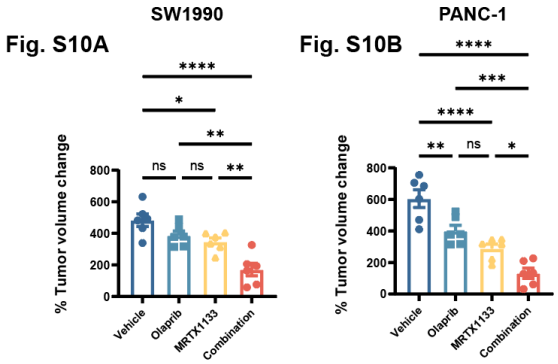

Supplementary Figure 10A-B. Relative SW1990 (A) and PANC-1 (B) tumor volume. Tumor volume was measured every day. Relative tumor volume was calculated for monitoring dynamic change and indicated as percent change from baseline. Data were analyzed by one-way ANOVA. Ns, no significant. *P<0.05, **P<0.01, ***P<0.001, ****P<0.0001. Mean ± SEM shown. 6 animals per group.

•Figure S5G: Address the lack of formal statistical analysis in the GSEA. Clearly demonstrate downregulation of HR genes after KRAS inhibition.

RESPONSE: We thank the reviewer for the valuable suggestion. Following the reviewer's advice, we have performed a formal GSEA to statistically assess the changes in the Homologous Recombination (HR) pathway upon KRAS inhibition and have updated Figure S11G.

The analysis revealed a negative enrichment trend for the homology directed repair set. The result was nominally significant with a Nominal P-value of 0.0475 and a Normalized Enrichment Score (NES) of -1.372. While the False Discovery Rate (FDR) q-value of 0.18 did not meet the stringent threshold for statistical significance after multiple hypothesis correction, the consistent negative enrichment trend strongly suggests a downregulation of this pathway.

Importantly, this observation is consistent with our other findings. For example, our data in Figure S11E shows a decreased expression of the RAD51 after treatment. Therefore, while the GSEA result on its own represents a trend, it provides valuable transcriptomic-level evidence that complements our other data to support our conclusion. The revised **Figure S11G** and its legend now include all these statistical parameters for full transparency.

Fig. S11G

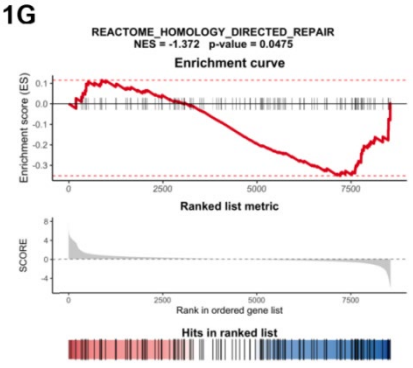

Supplementary Figure 11G. Gene Set Enrichment Analysis (GSEA) reveals significant downregulation of the Homology Directed Repair pathway under combination treatment. GSEA plot for the "REACTOME_HOMOLOGY_DIRECTED_REPAIR" gene set. Genes were pre-

ranked based on their differential expression between combination treatment and vehicle treatment, from the most upregulated (left) to the most downregulated (right). The plot demonstrates that genes within this pathway are significantly enriched among the downregulated genes, as indicated by a negative Normalized Enrichment Score (NES = -1.372) and a nominal p-value of 0.0475.

•Line 117 (Fig S2A): Explain why HR gene downregulation is inconsistent across cell lines (e.g., SW1990 vs. AsPC-1 and PANC-1).

RESPONSE: We thank the reviewer for raising this important point regarding the inconsistency in homologous recombination (HR) gene downregulation across different cell lines in Figure S2A. Indeed, our initial data showed heterogeneous responses, with RAD51 exhibiting the most pronounced downregulation primarily in SW1990 cells, while AsPC-1 and PANC-1 cells displayed variable on many HR genes, including RAD51. We attribute this variability to the inherent genetic and molecular heterogeneity among pancreatic cancer cell lines, including differences in baseline KRAS dependency, DNA repair pathway proficiency, and cell cycle regulation, which can influence responsiveness to KRAS inhibition. Importantly, despite these inconsistencies, we confirmed that the key downstream effector of the HR pathway, RAD51, was consistently reduced across the cell lines, highlighting a core mechanism of HR impairment induced by the treatment.

To further investigate and provide solid evidence validating these findings, we conducted additional experiments using cells exposed to the inhibitor treatments, followed by RT-qPCR analysis. These results demonstrate significant downregulation of key HR genes, including RAD51, RPA32, and BRCA1, across the tested cell lines ($P < 0.05$, one-way ANOVA test)(**Fig S2B**). This confirmatory evidence supports the mechanistic role of HR pathway modulation in our study and addresses the observed inconsistencies without necessitating changes to the main manuscript at this stage. These additions strengthen our insights into HR dynamics and fully resolve the

reviewer's concern.

Fig. S2B

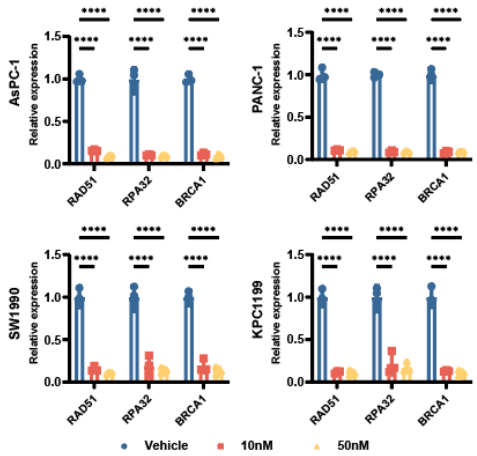

Supplementary Figure 2B. Relative mRNA expression of key HR genes (RAD51, RPA32, BRCA1) in four KRAS^{G12D} mutant cell lines treated with MRTX1133 (10 nM or 50 nM) for 24 hours. Data were determined by RT-qPCR and are presented as mean ± SEM from three biological replicates, with individual technical replicates shown as dots. Statistical significance was determined by one-way ANOVA. (****P<0.0001).

•Line 124 (Fig 2E-H): Elucidate why some HR-related markers (e.g., MDC1) are unaffected.

RESPONSE: We thank the reviewer for the insightful comment. As observed, BRCA1, RPA32, and RAD51 foci are significantly reduced following KRAS^{G12D} inhibition, whereas other DNA damage response (DDR)-associated markers such as MDC1, FK2, and 53BP1 appear largely unchanged.

This differential response likely reflects the distinct roles and regulatory mechanisms of these proteins within the DDR network. Specifically, BRCA1, RPA32, and RAD51 are core components of the homologous recombination (HR) pathway and are tightly regulated by transcriptional and signaling inputs. In contrast, MDC1 and 53BP1 are involved in the early sensing of double-strand breaks (DSBs) and in non-homologous end joining (NHEJ) repair pathways. In previous reports on DNA damage repair,

similar instances have been observed where BRCA1 decreases independently of MDC1[6], highlighting potential alternative regulatory pathways in the DNA damage response network.

•Line 127-129 (Fig 2): Clarify whether pan-KRAS inhibition induces HR deficiency in KRAS G12D cells.

RESPONSE: We thank the reviewer for requesting clarification on whether pan-KRAS inhibition induces HR deficiency in $KRAS^{G12D}$ mutant cells, which is a key aspect of our mechanistic studies. To address this, we conducted additional dose-response experiments treating $KRAS^{G12D}$-expressing pancreatic cancer cells (AsPC-1, PANC-1, SW1990) with pan-KRAS inhibitor BI-2865 at concentrations of 0, 1, and 5 μM for 24 hours. Western blot analysis revealed a dose-dependent reduction in downstream signaling markers, including pERK and pAKT, indicative of effective KRAS pathway inhibition(**Fig. S4A-C**). Concomitantly, we observed significant downregulation of key HR genes, such as BRCA1, RPA32, and RAD51 expression (**Fig. S4A-C**). Furthermore, functional assays demonstrated impaired HR gene foci formation (**Fig. S4D-J**) and decreased HR repair efficiency, confirming induction of HR deficiency (**Fig. S4K-M**).

These findings emphasized that pan-KRAS inhibition recapitulates HR deficiency in $KRAS^{G12D}$ cells, similar to effects observed with mutant-specific inhibitors. These additions provide robust evidence resolving the reviewer's query and enhance the overall mechanistic framework of our study.

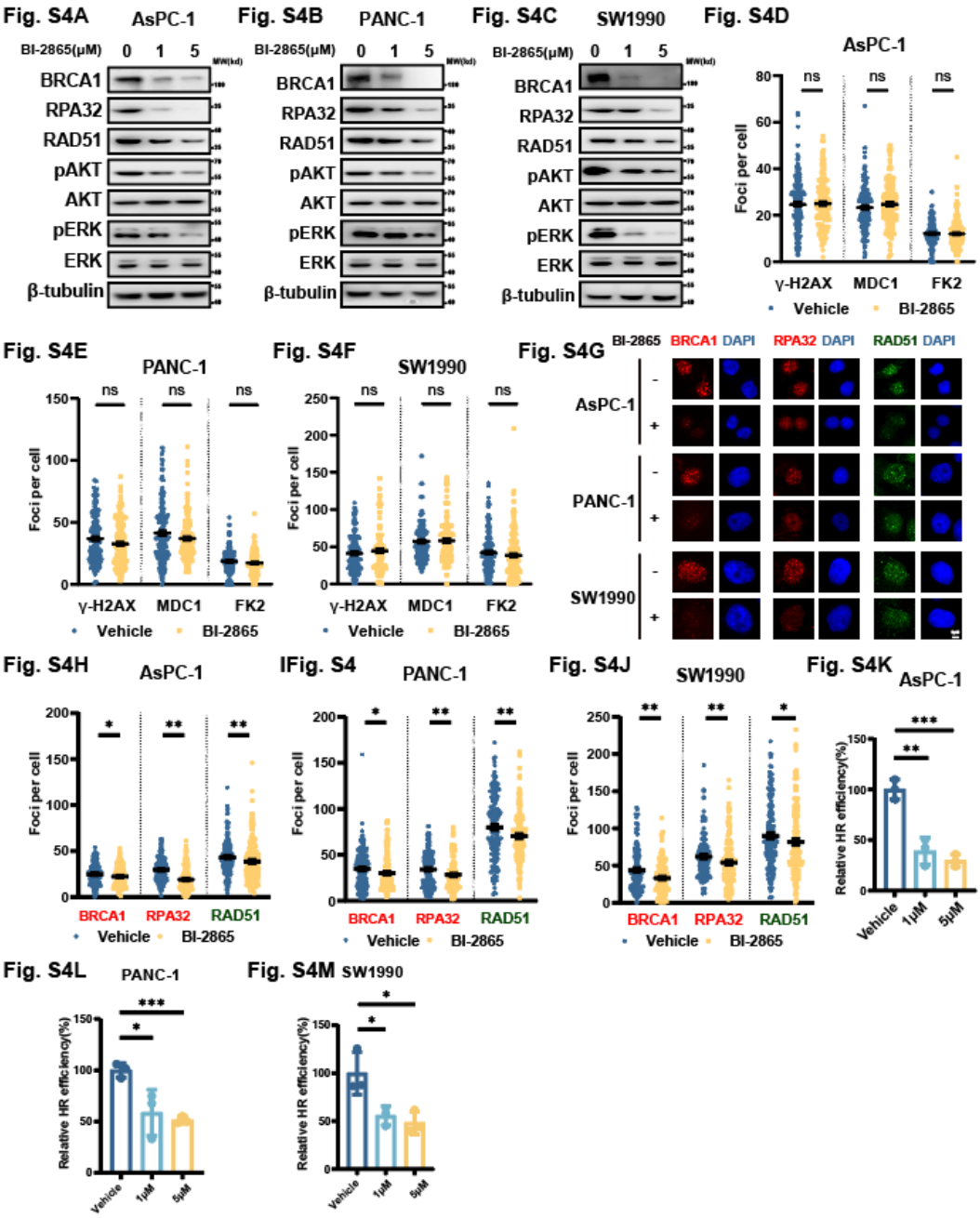

Supplementary Figure 4A-C. Western blot analysis of BRCA1, RPA32, RAD51, total ERK, total AKT, phospho-ERK, and phospho-AKT protein levels in KRASG12D pancreatic cancer cell lines AsPC-1(A), PANC-1(B) and SW1990(C) treated with vehicle (DMSO) or BI-2865 at the indicated concentrations for 24 hours. Cell lysates were collected for immunoblotting. β-Tubulin served as the loading control.

Supplementary Figure 4D-F. Immunofluorescence detection of DNA damage marker foci in KRAS^{G12D} pancreatic cancer cells treated with BI-2865. Quantification data for γ-H2AX, MDC1 and FK2 foci formation in the indicated cell lines AsPC-1(D), PANC-

1(E) and SW1990(F) with and without BI-2865 treatment (5μM) at 1 h after 2Gy X-ray irradiation treatment (γ-H2AX, MDC1 and FK2). Statistical significance of differences was determined by unpaired Student's t-test (ns, no significant.). Black bars indicate the mean from > 100 cells. Mean ± SEM shown.

Supplementary Figure 4G-J. Immunofluorescence detection of HR marker foci in $KRAS^{G12D}$ pancreatic cancer cells treated with BI-2865. Representative micrographs (G) and quantification data for BRCA1, RPA32 and RAD51 foci formation (H-J) in the indicated cell lines with and without BI-2865 treatment (5μM), at 1 h after 2Gy X-ray irradiation treatment (BRCA1), at 6 h after 2Gy X-ray irradiation treatment (RPA32 and RAD51). Statistical significance of differences was determined by unpaired Student's t-test (*P<0.05, **P<0.01). Black bars indicate the mean from > 100 cells. Mean ± SEM shown. The scale bar indicates 10 μm.

Supplementary Figure 4K-M. Inhibition of $KRAS^{G12D}$ by BI-2865 regulated HR repair efficiency in $KRAS^{G12D}$ pancreatic cancer cells. AsPC-1(K), PANC-1(L), and SW1990(M) were treated with BI-2865(1μM, 5μM). Efficiency was measured using DR-GFP reporter assay system. Data are shown as the mean ± SEM. Statistical significance of differences compared to vehicle control was determined by unpaired Student's t-test (*P<0.05, **P<0.01, ***P<0.001).

•Line 154-156 (Fig 3): Correct inconsistencies in figure references and legends.

RESPONSE: We thank the reviewer for this helpful comment. We have corrected all inconsistencies in figure references and legends for Figure 3 to ensure clarity and internal consistency across the main text and Figures. Specifically, we clarified that cell growth inhibition (CGI) ≥ 50 represents a threshold defining strong synergistic interactions in our combinatorial analyses. This metric has now been explicitly defined in both the **Results section and the Figure 3 legend** to avoid ambiguity and ensure consistency throughout the manuscript.

•Line 187 (Fig 6C): Explain discrepancies in mouse group sizes and provide details of in vivo drug preparation.

RESPONSE: We thank the reviewer for requesting clarification regarding the mouse group sizes and drug preparation procedures. The differences in group sizes reflect distinct experimental objectives rather than inconsistencies in design: the short-term imaging study (n = 3 per group) was performed to monitor early tumor responses and treatment kinetics by bioluminescent imaging at days 7 and 14, whereas the long-term survival study (n = 10 per group) was conducted independently to assess therapeutic durability and overall survival using Kaplan–Meier analysis, which requires larger cohorts for statistical power. For drug preparation, MRTX1133 (30 mg/kg, i.p.) was dissolved in a vehicle of 8% DMSO + 40% PEG300 + 7% Tween-80 + 45% PBS (pH 7.4). A typical 10 mL formulation contained 60 mg MRTX1133 in 0.8 mL DMSO mixed with 4.0 mL PEG300 and 0.7 mL Tween-80, followed by 4.5 mL PBS to a final volume of 10 mL and sterilized through a 0.22 μm filter. Each mouse (~20 g) received 100 μL intraperitoneally once daily to achieve a 30 mg/kg dose. Olaparib (50 mg/kg, i.p.) was formulated in the same vehicle for consistency, and both drugs were administered daily for 7 days with vehicle-treated controls. These details have been added to the Methods and figure legends to ensure transparency and reproducibility.

References

1. Canté-Barrett, K. *et al.* MEK and PI3K-AKT inhibitors synergistically block activated IL7 receptor signaling in T-cell acute lymphoblastic leukemia. *Leukemia* 30, 1832-1843 (2016).
2. Coussy, F. *et al.* Combination of PI3K and MEK inhibitors yields durable remission in PDX models of PIK3CA-mutated metaplastic breast cancers. *J Hematol Oncol* 13, 13 (2020).
3. Vena, F. *et al.* MEK inhibition leads to BRCA2 downregulation and sensitization to DNA damaging agents in pancreas and ovarian cancer models. *Oncotarget* 9, 11592-11603 (2018).
4. Zerbib, J. *et al.* Human aneuploid cells depend on the RAF/MEK/ERK pathway for overcoming increased DNA damage. *Nat Commun* 15, 7772 (2024).
5. Milacic, M. *et al.* The Reactome Pathway Knowledgebase 2024. *Nucleic Acids Research* 52, D672-D678 (2023).
6. Zhu, Q. *et al.* RNF19A-mediated ubiquitination of BARD1 prevents BRCA1/BARD1-dependent homologous recombination. *Nat Commun* 12, 6653 (2021).

REVIEWER #1:

The authors have done an excellent job addressing my comments and those of the other reviewers. Since the last incarnation of this manuscript, they have done multiple additional experiments to unravel the mechanisms behind their findings. The manuscript is much stronger with more sound conclusions. I have no further comments for the authors at this time.

RESPONSE: We sincerely thank the reviewer for their positive evaluation and for appreciating the additional experiments and mechanistic insights included in the revised manuscript. We are grateful for the time and effort dedicated to reviewing our work.

REVIEWER #2:

The revised manuscript and the authors' responses to previous comments are satisfactory.

RESPONSE: We thank the reviewer for their time and for finding our revisions satisfactory.

REVIEWER #3:

The authors have done a commendable job in addressing reviewers' concerns. I have no further question.

Only a minor issue: there is a mislabeling in the legend of figure 3 (panel C is mentioned twice and the second time actually refers to D)

RESPONSE: We thank the reviewer for their kind words and for carefully spotting this error. We have corrected the legend of Figure 3. We have double-checked all figure legends to ensure accuracy.

REVIEWER #4:

I co-reviewed this manuscript with one of the reviewers who provided the listed

reports. This is part of the Nature Communications initiative to facilitate training in peer review and to provide appropriate recognition for Early Career Researchers who co-review manuscripts.

RESPONSE: We appreciate the contribution of the co-reviewer in the assessment of our manuscript.